Spring 2017

Qualitative modeling of chaotic logical circuits and walking droplets: a dynamical systems approach

Aminur Rahman
New Jersey Institute of Technology

Copyright Warning & Restrictions

The copyright law of the United States (Title 17, United States Code) governs the making of photocopies or other reproductions of copyrighted material.

Under certain conditions specified in the law, libraries and archives are authorized to furnish a photocopy or other reproduction. One of these specified conditions is that the photocopy or reproduction is not to be "used for any purpose other than private study, scholarship, or research." If a, user makes a request for, or later uses, a photocopy or reproduction for purposes in excess of "fair use" that user may be liable for copyright infringement,

This institution reserves the right to refuse to accept a copying order if, in its judgment, fulfillment of the order would involve violation of copyright law.

Please Note: The author retains the copyright while the New Jersey Institute of Technology reserves the right to distribute this thesis or dissertation

Printing note: If you do not wish to print this page, then select "Pages from: first page # to: last page #" on the print dialog screen

ABSTRACT

QUALITATIVE MODELING OF CHAOTIC LOGICAL CIRCUITS AND WALKING DROPLETS: A DYNAMICAL SYSTEMS APPROACH

by
Aminur Rahman

Logical circuits and wave-particle duality have been studied for most of the 20^{th} century. During the current century scientists have been thinking differently about these well-studied systems. Specifically, there has been great interest in chaotic logical circuits and hydrodynamic quantum analogs.

Traditional logical circuits are designed with minimal uncertainty. While this is straightforward to achieve with electronic logic, other logic families such as fluidic, chemical, and biological, naturally exhibit uncertainties due to their inherent nonlinearity. In recent years, engineers have been designing electronic logical systems via chaotic circuits. While traditional boolean circuits have easily determined outputs, which renders dynamical models unnecessary, chaotic logical circuits employ components that behave erratically for certain inputs.

There has been an equally dramatic paradigm shift for studying wave-particle systems. In recent years, experiments with bouncing droplets (called *walkers*) on a vibrating fluid bath have shown that quantum analogs can be studied at the macro scale. These analogs help us ask questions about quantum mechanics that otherwise would have been inaccessible. They may eventually reveal some unforeseen properties of quantum mechanics that would close the gap between philosophical interpretations and scientific results.

Both chaotic logical circuits and walking droplets have been modeled as differential equations. While many of these models are very good in reproducing

the behavior observed in experiments, the equations are often too complex to analyze in detail and sometimes even too complex for tractable numerical solution. These problems can be simplified if the models are reduced to discrete dynamical systems. Fortunately, both systems are very naturally time-discrete. For the circuits, the states change very rapidly and therefore the information during the process of change is not of importance. And for the walkers, the position when a wave is produced is important, but the dynamics of the droplets in the air are not.

This dissertation is an amalgam of results on chaotic logical circuits and walking droplets in the form of experimental investigations, mathematical modeling, and dynamical systems analysis. Furthermore, this thesis makes connections between the two topics and the various scientific disciplines involved in their studies.

QUALITATIVE MODELING OF CHAOTIC LOGICAL CIRCUITS AND WALKING DROPLETS: A DYNAMICAL SYSTEMS APPROACH

by
Aminur Rahman

A Dissertation
Submitted to the Faculty of
New Jersey Institute of Technology
and Rutgers, The State University of New Jersey–Newark
in Partial Fulfillment of the Requirements for the Degree of
Doctor of Philosophy in Mathematical Sciences

Department of Mathematical Sciences, NJIT
Department of Mathematics and Computer Science, Rutgers–Newark

May 2017

APPROVAL PAGE

QUALITATIVE MODELING OF CHAOTIC LOGICAL CIRCUITS AND WALKING DROPLETS: A DYNAMICAL SYSTEMS APPROACH

Aminur Rahman

Dr. Denis L. Blackmore, Dissertation Advisor — Date
Professor of Mathematical Sciences, NJIT

Dr. Victor V. Matveev, Committee Member — Date
Associate Professor of Mathematical Sciences, NJIT

Dr. Roy H. Goodman, Committee Member — Date
Associate Professor of Mathematical Sciences, NJIT

Dr. Casey O. Diekman, Committee Member — Date
Assistant Professor of Mathematical Sciences, NJIT

Dr. Ivan C. Christov, Committee Member — Date
Assistant Professor of Mechanical Engineering, Purdue University

BIOGRAPHICAL SKETCH

Author: Aminur Rahman

Degree: Doctor of Philosophy

Date: May 2017

Undergraduate and Graduate Education:

- Doctor of Philosophy in Applied Mathematics,
  New Jersey Institute of Technology, Newark, NJ, 2017
- Bachelor of Science in Applied Mathematics,
  New Jersey Institute of Technology, Newark, NJ, 2010

Major: Applied Mathematics

Publications resulting from this thesis:

A. Rahman, I. Jordan, D. Blackmore. Qualitative models and experimental investigation of chaotic NOR gates and set/reset flip-flops (under review).

A. Rahman, D. Blackmore. Threshold voltage dynamics of chaotic RS flip-flop circuits (under review).

A. Rahman, D. Blackmore. Neimark–Sacker bifurcation and evidence of chaos in a discrete dynamical model of walkers. *Chaos, Solitons & Fractals* **91** 339-349 (2016)

D. Blackmore, A. Rahman, J. Shah. Discrete dynamical modeling and analysis of the R-S flip-flop circuit. *Chaos, Solitons & Fractals* **42** 951-963 (2009).

Presentations resulting from this thesis:

INVITED TALKS

Bifurcations in walking droplet dynamics. *Society for Industrial and Applied Mathematics Dynamical Systems Conference*, Snowbird Resort, Snowbird, UT, May 21, 2017

Dynamical modeling and analysis of walking droplets and chaotic logical circuits. *Numerical Methods for PDEs Seminar*, Massachusetts Institute of Technology, Cambridge, MA, February 22, 2017

Dynamical modeling and analysis of chaotic logical circuits and walking droplets. *Dynamical Systems Seminar*, University of Rhode Island, South Kingston, RI, February 8, 2017

Neimark-Sacker bifurcation and evidence of chaos in a discrete dynamical model of walkers. *American Mathematical Society Fall Northeast Sectional Conference 2015*, Rutgers University, New Brunswick, NJ, November 14, 2015

The chaotic ballet of walking droplets. *Mechanical and Industrial Engineering Colloquium*, New Jersey Institute of Technology, Newark, NJ, October 7, 2015

A scheme for modeling and analyzing the dynamics of logical circuits *Center for Nonlinear Studies Seminar*, Los Alamos National Laboratory, Los Alamos, NM, May 21, 2015

A scheme for modeling and analyzing the dynamics of logical circuits *Society for Industrial and Applied Mathematics Dynamical Systems Conference*, Snowbird Resort, Snowbird, UT, May 18, 2015

Further analysis of discrete dynamical models of the RS flip-flop circuit *American Mathematical Society Fall Southeast Sectional Conference*, University of North Carolina at Greensboro, Greensboro, NC, November 8, 2014

A scheme for modeling and analyzing the dynamics of logical circuits *American Mathematical Society Spring Sectional Northeast Conference*, University of Maryland Baltimore County, Baltimore, MD, March 29, 2014

CONTRIBUTED TALKS

The chaotic ballet of walking droplets. *Joint Mathematics Meetings*, Hyatt Regency Atlanta and Marriott Atlanta Marquis, Atlanta, GA, January 4, 2017

Neimark-Sacker bifurcations and evidence of chaos in a discrete dynamical model of walkers. *American Mathematical Society Fall Sectional Conference*, Bowdoin College, Brunswick, ME, September 24, 2016

A tempest in the mathematics of time: A brief history of chaos and its appearance in walking droplets and electronic circuits. *Math Graduate Student Seminar*, New Jersey Institute of Technology, Newark, NJ, June 21, 2016

Neimark-Sacker bifurcation and evidence of chaos in a discrete dynamical model of walkers. *American Physical Society 68th Annual Division of Fluid Dynamics Meeting*, Hynes Convention Center, Boston, MA, November 24, 2015

Neimark-Sacker bifurcation and evidence of chaos in a discrete dynamical model of walkers. *Math Graduate Student Seminar*, New Jersey Institute of Technology, Newark, NJ, June 11, 2015

A scheme for modeling and analyzing the dynamics of logical circuits *Joint Mathematics Meetings*, Baltimore, MD, January 15, 2014

Logical circuits: A scheme for discrete modeling and analysis. *Math Graduate Student Seminar*, New Jersey Institute of Technology, Newark, NJ, July 10, 2012

A scheme for modeling and analyzing the dynamics of logical circuits. *Hallenbeck Graduate Student Seminar*, University of Delaware, Newark, DE, October 20, 2010

POSTERS

A scheme for analyzing the dynamics of logical circuits. *Joint Mathematics Meetings*, Baltimore, MD, January 16, 2014

A scheme for analyzing the dynamics of logical circuits. *Graduate Student Association Research Day*, New Jersey Institute of Technology, Newark, NJ, October 31, 2013

A scheme for analyzing the dynamics of logical circuits. *Frontiers in Applied and Computational Mathematics*, New Jersey Institute of Technology, Newark, NJ, May 31 - June 2, 2013

A scheme for analyzing the dynamics of logical circuits. *Frontiers in Applied and Computational Mathematics*, New Jersey Institute of Technology, Newark, NJ, May 21 - 23, 2010

Discrete dynamical modeling and analysis of the R-S flip-flop circuit. *NJIT Experience Day*, New Jersey Institute of Technology, Newark, NJ, April 19, 2009

Discrete dynamical modeling and analysis of the R-S flip-flop circuit. *Dana Knox Student Research Showcase*, New Jersey Institute of Technology, Newark, NJ, April 8, 2009

Discrete dynamical modeling and analysis of the R-S flip-flop circuit. *Garden State Undergraduate Mathematics Conference*, Monmouth University, Monmouth, NJ, March 29, 2009

Chaos of the R-S flip-flop circuit. *Frontiers in Applied and Computational Mathematics*, New Jersey Institute of Technology, Newark, NJ, May 19 - 21, 2008

Chaos of the R-S flip-flop circuit. *NJIT Experience Day*, New Jersey Institute of Technology, Newark, NJ, April 5, 2008

بِسْمِ اللهِ الرَّحْمٰنِ الرَّحِيْمِ

To my sister, Maryom Rahman (Sona), who was a source of light when there was only darkness.

আমার ছোট বোনের জন্য, যে আমার অন্ধকার জীবন এক ঝলক আলো হয়ে এসেছে.

الله أكبر

ACKNOWLEDGMENT

First and foremost, a very special thank you to my advisor, Professor Denis Blackmore, who has guided me from the time I was an undergraduate student. He encouraged me to think independently and spent countless hours helping me refine my ideas. He has praised me when I have succeeded and consoled me when I have failed. Denis is not only a great mentor, but also a great friend.

In addition, I would like to thank my dissertation committee members, Professors Ivan Christov, Victor Matveev, Roy Goodman, and Casey Diekman, for fruitful discussions and helpful advice. Victor for being one of the best teachers I have had, Roy for always challenging me to become a better applied mathematician, and Casey for being emblematic of a successful early career academic and providing me with informal advice for the next stage of my career.

In particular, I would like to thank Ivan Christov (Purdue University) for being a great friend. He has introduced me to numerous potential employers, provided opportunities for collaboration, and invited me to present my research at various seminars. Furthermore, Ivan gives me frank and informal advice, which has aided me in making good academic decisions.

A special thank you to Professor David Horntrop, my first university math professor, my undergraduate advisor, and later my supervisor for teaching, for spending countless hours advising and helping me with not only teaching, but also with job applications and interviews.

I would also like to thank Professor Blackmore's and my undergraduate research assistant, Ian Jordan, who spent many months on the electronics experiments presented in this work. In addition to research, he was a wonderful student in several courses and is a great friend.

Finally, I would like to thank my family for their constant love and support. My extended family for their encouragement. My grandmothers, Kalpana Rahman (née Grace Mary Christian) and Kanija Khatun, and my late grandfathers, Khalilur Rahman and Sakhwat Hossein, for always wishing the best for me. My parents, Sahidur Rahman and Sofia Rahman (née Sofia Khatun), who were instrumental in creating a stress free environment for my research. My wonderful sister, Maryom Rahman, for her unconditional love and adoration.

I would also like to thank my friends for our many adventures and occasional misadventures, which have made my life truly exciting. In particular, I would like to thank Moira Jeanne Mahady for her emotional support, constant motivation, and for hiking the tallest mountains (east of the Mississippi) with me, which has had a direct impact on this dissertation. In fact, one such adventure allowed me to clear my mind, and while camping solve a proof I had been stuck on and subsequently finish writing the article within the following week. And I can't forget Rory the mountain climbing Aussie.

TABLE OF CONTENTS

Chapter **Page**

TABLE OF CONTENTS
(Continued)

Chapter **Page**

TABLE OF CONTENTS
(Continued)

Chapter **Page**

TABLE OF CONTENTS
(Continued)

Chapter **Page**

LIST OF TABLES

Table **Page**

LIST OF FIGURES

LIST OF FIGURES
(Continued)

Figure **Page**

LIST OF FIGURES
(Continued)

Figure **Page**

LIST OF FIGURES
(Continued)

Figure **Page**

CHAPTER 1

INTRODUCTION

If Poincaré is the father of Dynamical Systems, Newton, Leibniz, and the Bernoullis, are its great grandfathers. The foundations were laid in the late 1600s and early 1700s, through intimate connections to real world problems with works like "Nova Methodus" [85], "Principia" [115], "Methodus Fluxionum" [116], "Explicationes" [5], and many others. Two centuries later, Poincaré applied new mathematical techniques to the study of celestial mechanics [130, 131], which came to be known as *Dynamical Systems*. He showed that information about a system can be extracted through its qualitative properties (*phase space*); i.e., without having to solve the system of equations. Meanwhile, Lyapunov developed ideas on the stability of dynamical systems [93], many of which are used in the linear stability analysis conducted in this thesis. In fact, the general theme of this thesis is nonlinear dynamics and chaos; i.e., unstable systems, which incidentally also interested Poincaré.

A story that comes to mind is of Poincaré and the King of Sweden. In 1887, Oscar II of Sweden posed a question with a prize. Roughly, he asked, if there are three masses in space what will the motion of this system be? This has been dubbed "the three-body problem". Poincaré used asymptotic techniques to solve a restricted - perturbed three-body problem; that is let two of the bodies have much greater mass than the third. While he won the prize, there was a mistake in his analysis. He later realized that the method he had used would not accurately describe the motion due to the system depending on initial conditions with great sensitivity [129]. This, along with Hadamard's billiards [54], essentially initiated the study of chaotic systems.

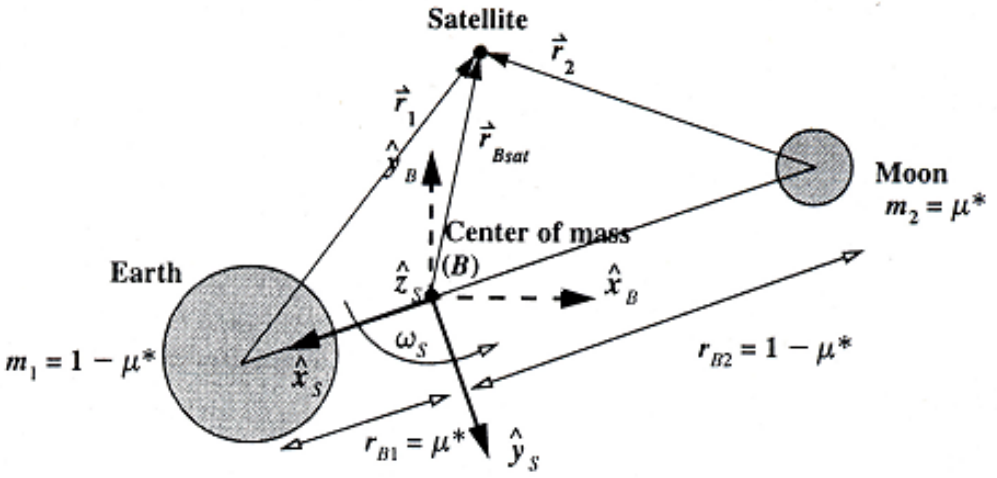

Figure 1.1 An illustration of the three-body problem. (Reproduced with permission Springer Publishing Company).

Source: D. Vallado. *Fundamentals of astrodynamics and applications.* Springer-Verlag, New York, NY, 2007

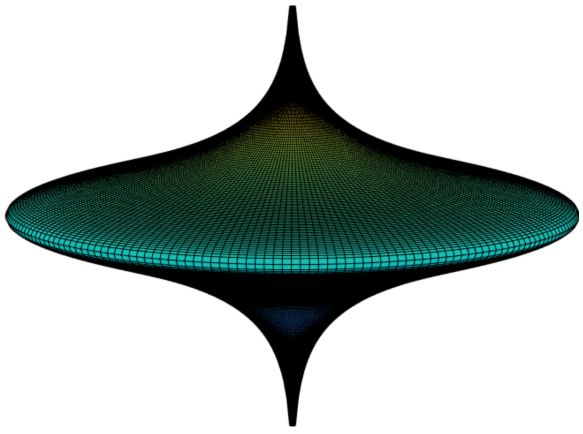

Figure 1.2 An illustration of a *pseudosphere* used to create the surface for Hadamard's billiards.

For many years, these types of systems were generally avoided. In the 1950s and 1960s, Lorenz studied nonlinear weather forecasting models through numerical simulations. He discovered that inputting two close initial conditions created very different simulation results [89] (Figure 1.3). Lorenz continued his work [90, 91] and others followed in his footsteps, which led to the properties (sensitive dependence, aperiodicity, and transitivity [102]) of "Chaos" finally being investigated *en masse* and delineated.

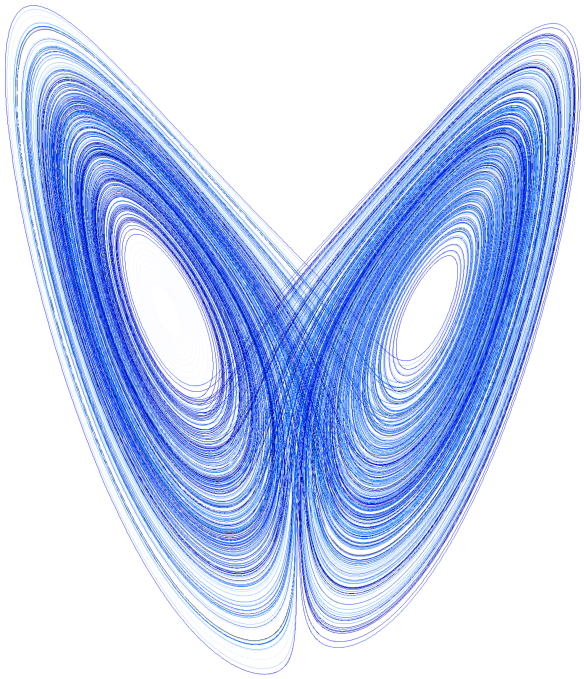

Figure 1.3 Simulation of the Lorenz equations resulting in the Lorenz strange. (Reproduced and modified under *CC0 License*).

Source: Wikimol. https://en.wikipedia.org/wiki/File:Lorenz_system_r28_s10_b2-6666.png. Date accessed: April 13, 2017. Date added: May 2005.

While all of the dynamical systems studied in its early days were continuous (differential equations), later mathematicians started studying a close cousin of differential equations – difference equations or iterations of *maps*. These difference equations are dubbed *Discrete Dynamical Systems* and have strong connections with

their continuous counterparts. An important feature of discrete dynamical systems is the relative ease, compared to continuous dynamical systems, in their analysis and simulations. One major drawback is in the approximate nature of discrete dynamical models – most things in nature are perceived as evolving continuously. However, as we have learned from Poincaré, we may not always need to be completely precise when making qualitative conclusions.

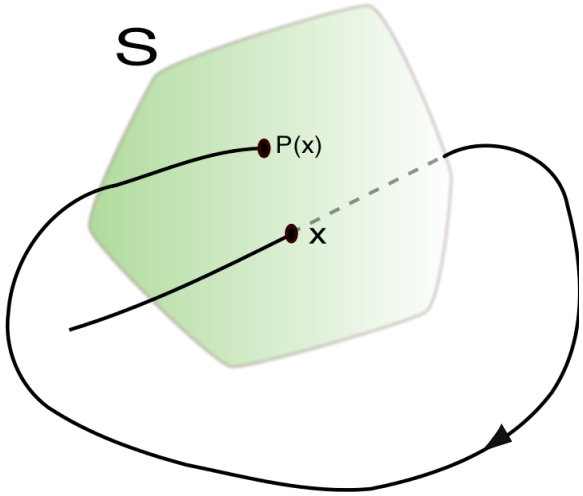

Figure 1.4 An example of a Poincaré map. (Reproduced under *Creative Commons Attribution-Share Alike 3.0*)

Source: Gato ocioso. https://en.wikipedia.org/wiki/File:Poincare_map.svg. Date accessed: April 25, 2017. Date added: February 2008.

It is often difficult to develop a discrete analog of a continuous system, however one way to derive, or in most cases approximate, this analog is through a first return map. If we have a continuous dynamical system that intersects a manifold of the phase space at recurring time intervals, we can define a first return map; also called a *Poincaré map* (Figure 1.4). One of the most studied first return map is the Hénon map (Figure 1.5), which is a simplified Poincaré map of Lorenz's equations [63]. While this is a popular technique, it should be noted that not all maps are derived/approximated

Figure 1.5 The Hénon attractor. (Reproduced under *Free Art License*).

Source: XaosBits. https://nl.wikipedia.org/wiki/File:HenonMapImage.png. Date accessed: April 13, 2017. Date added: February 2005.

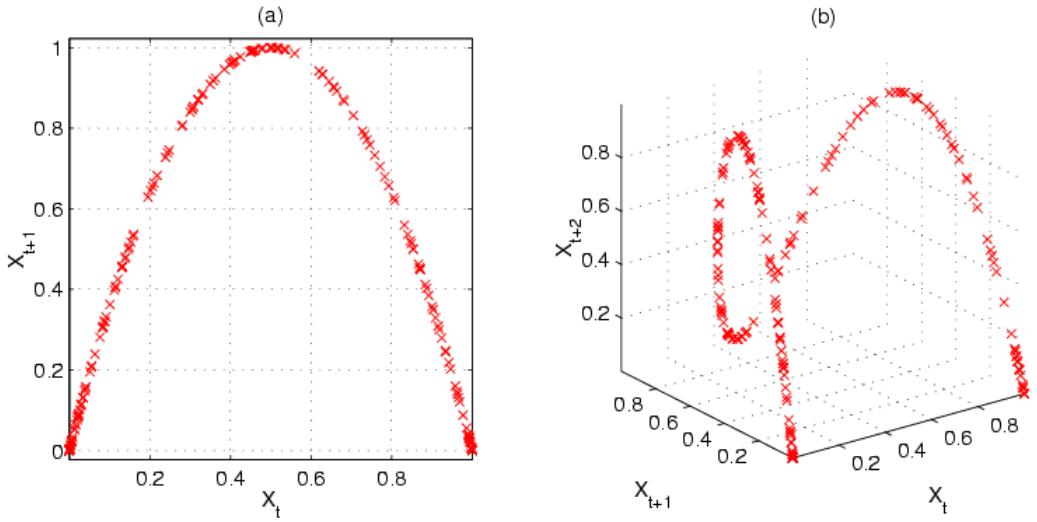

Figure 1.6 Two and three dimensional scatter plots of iterates of the logistic map. (Reproduced under *Creative Commons Attribution-Share Alike 3.0*).

Source: Maksim. https://en.wikipedia.org/wiki/File:Logistic_map_scatterplots_large.png. Date accessed: April 13, 2017. Date added: March 2006.

in this manner. Some of the most important maps such as the logistic map [100] (Figure 1.6), a model of population dynamics, and Duffing map, which is a discrete version of the Duffing equation [39], are not first return maps.

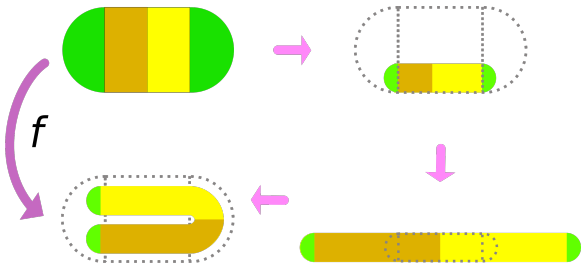

Figure 1.7 Illustration of one iteration of the Smale Horseshoe. (Creative Commons Attribution-Share Alike 3.0)

Source: SyntaxError55. https://en.wikipedia.org/wiki/File:Smale_Horseshoe_Map.svg. Date accessed: April 13, 2017. Date added: December 2007

The map that has had perhaps the most influence on the study of chaotic systems is the horseshoe map [150, 151, 152], developed by Smale in 1967, and appropriately called the *Smale horseshoe*. He developed the concepts of the horseshoe by studying a continuous system, the van der Pol oscillator [158, 159]. The idea was to search for stretching and folding of iterate space, like a horseshoe, which Smale showed would be sufficient to satisfy the properties of a chaotic system. A nice illustration of a similarly chaotic map is the Baker's map [153]. The idea is to consider a piece of square dough and cut it in half vertically. Then stack the halves on top of each other while compressing/stretching it back into the square. This continues *ad infinitum*. One can imagine placing two dots on the dough, and then once the process has started the two dots separate from each other at an exponential rate. An example of the Baker's map using a picture of my advisor and me is shown in Figure 1.8. We shall directly use concepts from Smale's horseshoe map to analyze some of the dynamics investigated in this thesis.

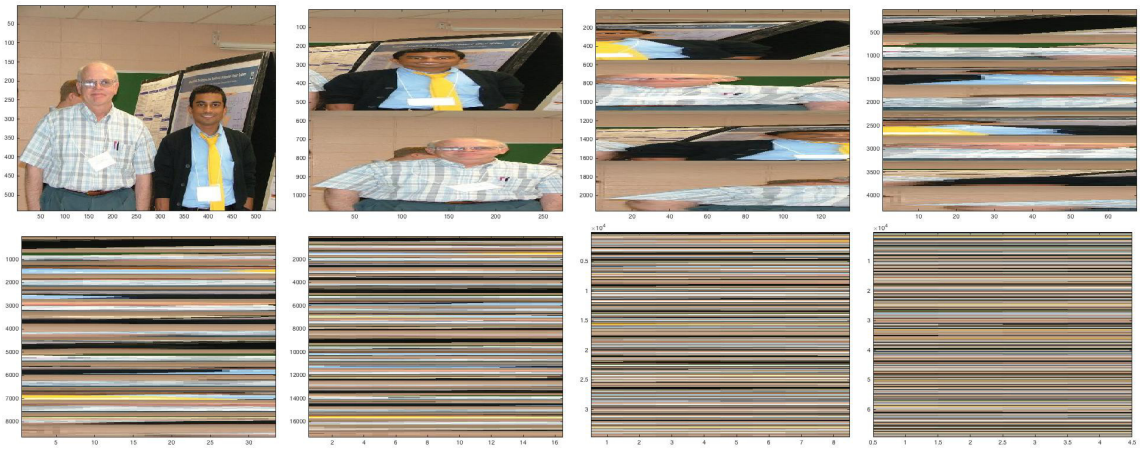

Figure 1.8 An example of a Baker's map applied to a photograph of my advisor and me. The top row shows iterates zero to three from left to right, and the bottom row shows iterates four to seven from left to right.

From its infancy, Dynamical Systems Theory has had an intimate connection to real world phenomena. It was first developed to study celestial mechanics, and eventually grew to become its own major field with an abundance of both theoretical and physical problems. In this thesis I present my contributions to both the theoretical and physical aspects of Dynamical Systems – the theory motivated by the physics. The motivations come from two rich physical phenomena: chaotic logical circuits and walking droplets.

1.1 Dynamical Systems Theory

Before we begin the more technical discussions, let us introduce some necessary definitions and notations. For simplicity we often denote the discrete dynamical system (difference equation) $x_{n+1} = f(x_n)$ as $x = f(x)$. We also denote a complex conjugate with a bar over the variable (e.g., $z \to \bar{z}$). First we define some terms related to topology,

Definition 1.1.1. A map $h : M \to M$, where M is a manifold, is said to be a *homeomorphism* if it is a bijective bicontinuous map.

Definition 1.1.2. Two dynamical systems $x = f(x)$ and $y = g(y)$ on M are *topologically equivalent* if there is a homeomorphism h of M such that h maps oriented (by increasing time) orbits of the first system onto oriented orbits of the second system. Such an h is called a *topological equivalence* between the systems (or sometimes a *conjugacy* - especially for the case of discrete dynamical systems).

Definition 1.1.3. The dynamical system $x = f(x)$ is said to be *structurally stable* if for every $\varepsilon > 0$ sufficiently small, all $g \in B_\varepsilon(f)$ are topologically equivalent to f.

Definition 1.1.4. Suppose a dynamical system $x = f_\mu(x)$ has one (or many) parameter(s) denoted by μ, and assume that in a small neighborhood of some critical value μ_*, $\mu_1 < \mu_* < \mu_2$ and $x = f_{\mu_2}(x)$ is not topologically equivalent to $x = f_{\mu_1}(x)$, the dynamical system is said to undergo a *bifurcation* at $\mu = \mu_*$.

Next we define chaos. Though there are a few different formal definitions of chaos, the one used in this dissertation is from Robinson [140] due to the book's explicit use of discrete dynamical systems. The definition is given (with minor modifications) in three parts,

Definition 1.1.5. A map $f : X \to X$ is *topologically transitive* on an invariant set Y provided the forward orbit of some point p is dense in Y.

Definition 1.1.6. A map $f : X \to X$ is said to have *sensitive dependence* on initial conditions if there is an $r > 0$ such that for each point $x \in X$ and $\varepsilon > 0$ there is a point $y \in X$ with $d(x, y) < \varepsilon$ and a $k \geq 0$ such that $d(f^k(x), f^k(y)) \geq r$.

Definition 1.1.7. A map $f : X \to X$ is said to be *chaotic* on an invariant set Y if

(i) f is transitive on Y,

(ii) f has sensitive dependence on initial conditions on Y.

Finally, we define a term that has already been used, but now we have the machinery to formally define it.

Definition 1.1.8. If the invariant set Y is an attracting set, we call it a *chaotic attractor*, and if it has fractal structure we say it is a *strange attractor*.

While there have been many great leaps in Dynamical Systems Theory, in this section we discuss the works that have been directly applied to the phenomena of interest. The focus of this dissertation is nonlinear dynamics, and more precisely chaos. The main property we are interested in for these models are the paths to chaos, which arise through a succession of bifurcations. Two bifurcations that appear often in this dissertation are the *Neimark–Sacker* [114, 144, 81] and *period doubling* (also known as a *flip* [81]) bifurcation. Furthermore, we can prove the existence of chaotic orbits without or in addition to analyzing the bifurcation. Some of the ways in which we prove chaos in this dissertation are through *3-cycles* [87] and *horseshoes* [148, 150, 151, 152, 72]. Finally, we also consider the idea of invariant measures in order to connect the dynamics of a map to the statistics of the orbits. In this section we briefly discuss these results and present the original theorems, with some modifications, without proof, which the reader may refer to in the cited literature.

The bifurcation that appears the most in this thesis is the Neimark–Sacker (N–S) bifurcation, which is essentially a discrete analog of the Hopf bifurcation. This can also be thought of as a Poincaré-like map of Hopf bifurcations on a torus ($S^1 \times S^1$; i.e., if we let S^1 be the circle the torus is the cartesian product of two circles). In a continuous two-dimensional dynamical system, a Hopf bifurcation occurs when a

spiral source/sink changes stability and produces a limit cycle as a parameter is varied. The bifurcation is supercritical if a stable limit cycle arises as the parameter increases. Conversely, the bifurcation is subcritical if an unstable limit cycle is created as the parameter decreases. For a discrete two-dimensional map a N–S bifurcation occurs in the same manner. Due to the discrete nature of the dynamical system, an invariant closed Jordan curve (a topological circle) is born instead of a limit cycle.

The existence of a N–S bifurcation at a specific fixed point for a single parameter can be shown by verifying the relevant genericity conditions and showing that the eigenvalues are complex conjugates of modulus one as the parameter passes through the critical value. A genericity condition is usually pivotal in proving a bifurcation (a topological change in the set of iterates) exists. Furthermore, the complex conjugate eigenvalues prove that the fixed point is a focus before and after the bifurcation, thereby allowing the creation of an invariant circle. This is shown formally in Theorem 1.1.1, modified from [81] to match the language in this thesis. We first define the normal form of the N–S bifurcation and the first Lyapunov coefficient, then we present the theorem. It should be noted that these two definitions are actually derived quantities, however for the sake of brevity we shall simply define them here.

Definition 1.1.9. For the dynamical system (difference equation)

$$\mathbf{x} = \begin{pmatrix} w \\ x \end{pmatrix} = \mathbf{f}_\mu(\mathbf{x}) \tag{1.1}$$

through the change of variables $x \mapsto z$ the *normal form* is given by

$$H(z, \bar{z}) := \lambda z + \sum_{2 \le j+k \le 3} \frac{1}{j!k!} g_{jk} z^j \bar{z}^k + O(|z|^4) \tag{1.2}$$

where λ is the multiplier of the system and z is a complex variable.

Definition 1.1.10. From the normal form above we define the *first Lyapunov coefficient* as

$$d(0) := \mathrm{Re}\left(\frac{\bar{\lambda} g_{21}}{2}\right) - \mathrm{Re}\left(\frac{(1-2\lambda)\bar{\lambda}^2}{2(1-\lambda)} g_{20} g_{11}\right) - \frac{1}{2}|g_{11}|^2 - \frac{1}{4}|g_{02}|^2.$$

Theorem 1.1.1 (Sacker 1964)**.** *Given a two-dimensional one-parameter dynamical system, $\boldsymbol{x} = \boldsymbol{f}_\mu(\boldsymbol{x})$, having at $\mu = \mu_*$ the fixed point $\boldsymbol{x}_*$ with complex multipliers $\lambda_{1,2} = \exp(\pm i\theta_*)$ there is a neighborhood of $\boldsymbol{x}_*$ in which a unique closed invariant curve bifurcates from $\boldsymbol{x}_*$ as μ passes through μ_* if the following genericity conditions are satisfied,*

(C.1) $r'(\mu_*) \neq 0$, *where* $r = |\lambda|$,

(C.2) $\exp(\pm ik\theta_*)$ *for* $k = 1, 2, 3, 4.$,

(C.3) The first Lyapunov coefficient $d(0) \neq 0$.

Furthermore, $d(0) < 0$ *is known as the supercritical case and* $d(0) > 0$ *is known as the subcritical case.*

Another bifurcation that appears in abundance in the study of walking droplets is the period doubling bifurcation. This bifurcation does precisely as the name suggests. As the relevant parameter is varied a fixed point bifurcates into a 2-cycle. This can also have a cascading effect where the 2-cycle then bifurcates into a 4-cycle with the process continuing *ad inordinatum*. The conditions for a flip bifurcation is stated in Theorem 1.1.2 [81], again with modifications.

Theorem 1.1.2 (Flip Bifurcation)**.** *Suppose that a one-dimensional one-parameter dynamical system*

$$x = f_\mu(x) \in C^\infty(\mathbb{R});\ x, \mu \in \mathbb{R}, \tag{1.3}$$

has the fixed point $x_* = 0$ *at* $\mu_* = 0$*, and let* $\lambda = f_0'(0) = -1$*. If the nondegeneracy conditions*

$$(C.1)\ \frac{1}{2}f_0''(0)^2 + \frac{1}{3}f_0'''(0) \neq 0; \qquad (C.2)\ \partial_\mu f_0'(0) \neq 0,$$

hold, then there exists a C^∞*-diffeomorphism transforming the system into*

$$\xi \mapsto -(1 + |g(\lambda)|\lambda)\xi \pm \xi^3 + O(\xi^4);\ g \in C^\infty(\mathbb{R}). \tag{1.4}$$

One consequence of a cascading period doubling bifurcation is the existence of 3-cycles, and as shown in [87] a 3-cycle implies chaos. The full theorem of Li and Yorke, with modifications, is given below.

Theorem 1.1.3 (Li-Yorke 1975)**.** *Let* I *be an interval and* $(F : I \to I) \in C(I)$*. Consider points* $a, b, c, d \in I$ *such that* $b = F(a)$*,* $c = F^2(a)$*,* $d = F^3(a)$*, and* $d \leq a < b < c$ *(or* $d \geq a > b > c$*). Then* $\forall k \in \mathbb{N}$*, there exists a periodic point in* I *with period* k*. Furthermore, there is an uncountable set* $S \subset I$ *containing no periodic points, which satisfies the conditions:*

$$(A)\ \forall p, q \in S \text{ such that } p \neq q, \limsup_{n\to\infty} |F^n(p) - F^n(q)| > 0$$
$$\text{and } \liminf_{n\to\infty} |F^n(p) - F^n(q)| = 0$$
$$(B)\ \forall p \in S \text{ and periodic point } q \in I, \limsup_{n\to\infty} |F^n(p) - F^n(q)| > 0$$

Perhaps the most influential development in modern dynamical systems theory is Smale's horseshoe [150]. Applying the horseshoe map to a pill shaped region (as shown in Figure 1.7) and its inverse *ad infinitum*, then intersecting these two sets give us a *Cantor dust* (the product of two interval Cantor sets). Smale first presented Theorem 1.1.4 in a 1963 symposium honoring Marston Morse at the Institute for Advance Study in Princeton, NJ [148]. For the sake of preserving a piece of history

we state Smale's theorem in its original form so the reader may see it in its full glory. Notice that not only do we have seemingly random behavior through the arbitrarily long periods, but we also have structural stability; i.e., horseshoe chaos is structurally stable.

Theorem 1.1.4 (Smale 1963)**.** *The horseshoe map f has a closed invariant set Λ that contains a countable set of periodic orbits of arbitrarily long period, and an uncountable set of nonperiodic orbits, among which there are orbits passing arbitrarily close to any point of Λ.*

1.2 Logical Circuits

Inventions and innovations of the latter part of the 20^{th} century have been dominated by electronics and computation. While computing devices have been around since before the 1900s, perhaps the first major paradigm shift in computation was Alan Turing and his team cracking the *Enigma* code via their computer, *Bombe*. Since then, many Nobel prizes have been awarded for advances in computing technology, such as with the transistor, quantum electronics, Josephson junctions, integrated circuits, opto-electronics, the charge-coupled device sensor, and optical communication. In addition, computers have even beaten humans at games that humans seemed to have an advantage in, such as chess, jeopardy, and go.

When we think of computation, we generally think of silicon based devices, and these devices are designed to be as stable as possible. We owe much of our modern comforts due to this endeavor, which has been a triumph for electrical engineering and physics. However, not all logical systems are electronic nor man-made, and as we observe, nature is seldom stable.

For example, the New Caledonian crow can solve complex problems involving tools and some nontrivial arithmetic [145, 156]. How can an animal with such a small brain perform tasks that dogs and human toddlers would find impossible? What type of computation could it be unconsciously doing? One thing we know for certain is that it is very different from the type of computation that computers do.

Since it is often easier to physically study electrical systems than logic families arising in nature, studying chaotic logical circuits can help us better understand naturally occurring logical systems. Before we can study chaotic logical circuits, we must first understand nonlinear circuits. Perhaps the first nonlinear circuit was the van der Pol oscillator [158] (Figure 1.9), first studied by van der Pol in the late 1920s. In this circuit he observed complex periodic curves, called *limit cycles*. He then studied the circuit with forcing [159] from an alternating current source E_s, which produced seemingly random trajectories. This was the first time chaos had been observed in an electronic circuit.

In 1983, Chua developed a simple chaotic circuit using an inductor, two capacitors, a resistor, and a nonlinear resistor [21, 22, 30, 23, 77] (Figure 1.10). When he measured the voltages across the two capacitors and the current through the inductor, he noticed projections of what appeared to be a strange attractor, similar to the Lorenz strange attractor, dubbed the *double scroll attractor* due to the scroll-like shape (Figure 1.11). The chaos in the system is produced by perturbations from the nonlinear resistor. In a standard resistor, the ratio between the current through it and the voltage drop across it is proportional with the constant of proportionality being the conductance (the reciprocal of resistance). In a nonlinear resistor, this relationship is as the name suggests: nonlinear. Specifically, in Chua's nonlinear resistor (called *Chua's diode*), the relationship is piecewise linear.

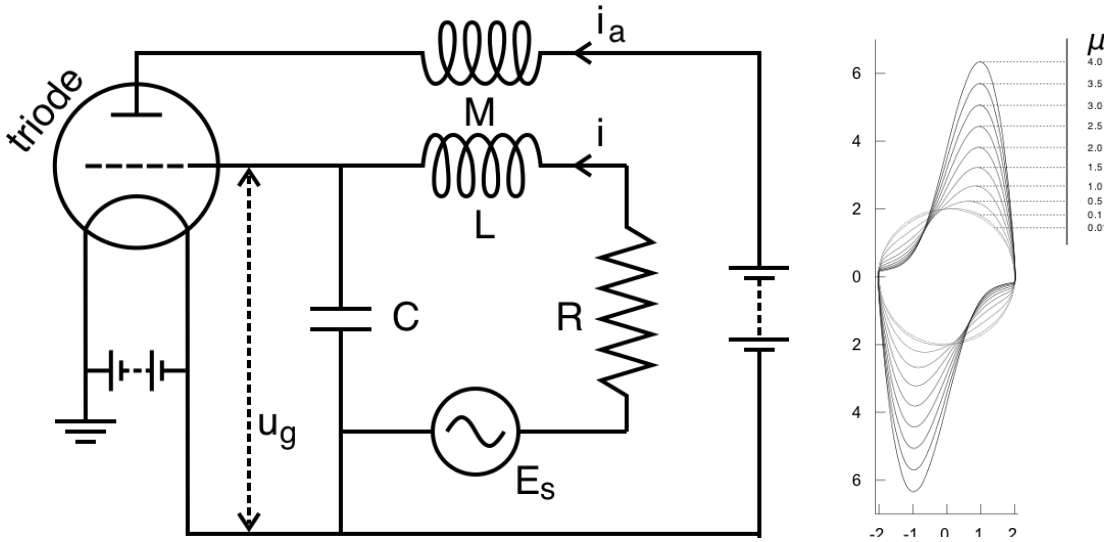

Figure 1.9 A physical realization of the van der Pol oscillator and limit cycles arising from the unforced van der Pol oscillator. (Reproduced under *Creative Commons Attribution-Share Alike 3.0*).

Source(Left): Kraaiennest. https://en.wikipedia.org/wiki/File:Van_der_pol_triode.svg. Date accessed: April 13, 2017. Date added: June 2009
Source(Right): Widdma. https://en.wikipedia.org/wiki/File:VanderPol-lc.svg. Date accessed: April 13, 2017. Date added: September 2009

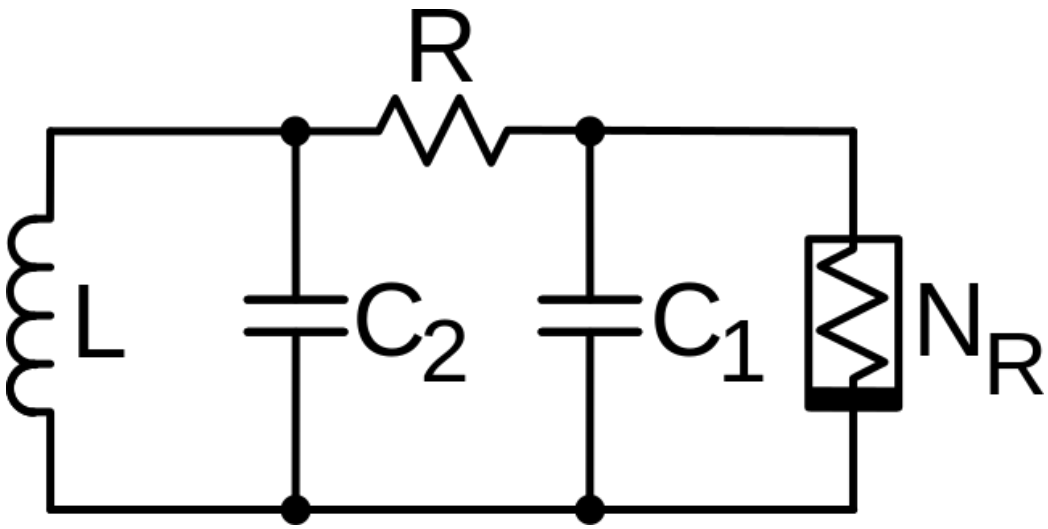

Figure 1.10 Schematic of Chua's circuit realized using an inductor, two capacitors, a resistor, and a nonlinear resistor. (Reproduced under *CC0 License*).

Source: Chetvorno. https://en.wikipedia.org/wiki/File:Chua27s_circuit_with_Chua_diode.svg. Date accessed: April 13, 2017. Date added: February 2014.

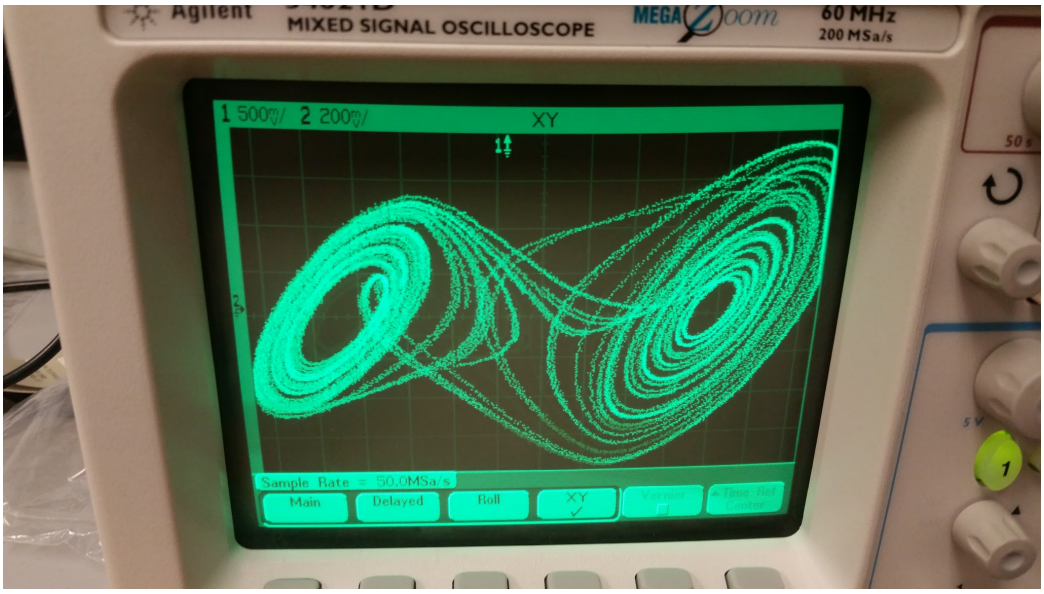

Figure 1.11 "Double scroll" attractor produced from our experiments on the oscilloscope by plotting the two capacitors in Chua circuit on each axis.

A year later Matsumoto modeled Chua's circuit as a system of three ordinary differential equations [99, 24, 23]. He derived them via Kirchoff's laws using the voltage law for the first loop and current law for the nodes on both sides of the standard resistor (1.5). This gives a system of equations that governs the voltages V_{C_1}, V_{C_2} across the capacitors C_1, C_2 and the current χ_L through the inductor L. He uses a function $g(V_{C_1})$ for current coming into the right node of the standard resistor from the nonlinear resistor and conductance G of the standard resistor.

$$\begin{aligned} C_1\frac{dV_{C_1}}{dt} &= G(V_{C_2} - V_{C_1}) - g(V_{C_1}) \\ C_2\frac{dV_{C_2}}{dt} &= G(V_{C_1} - V_{C_2}) + \chi_L \\ L\frac{d\chi_L}{dt} &= -V_{C_2} \end{aligned} \tag{1.5}$$

Since the 1990s there has been growing interest in controlling chaotic circuits starting from synchronization [123, 31], and leading to logical operations [118]. Early constructions of chaotic logical circuits used Chua's diode to manipulate the voltage to achieve logical outputs. For more complex logical circuits, components called *threshold control units* (TCUs) [109] have been employed [111, 110, 16].

The two logical circuits that we refer to most are the NOR gate and set/reset flip-flop (RSFF). The "black-box" schematics and truth tables of the classical NOR gate and RSFF are shown in Figures 1.12 and 1.13.

While there has been an abundance of *Simulation Program with Integrated Circuit Emphasis* (*SPICE*) simulations and some experimental investigations in the literature, such as [118, 111, 110], there is a dearth of models for the more complex chaotic logical circuits. This is understandable since the usual modeling techniques become ever more difficult to implement as the number of components increase. Traditionally, logical circuits have been modeled as systems of ordinary differential

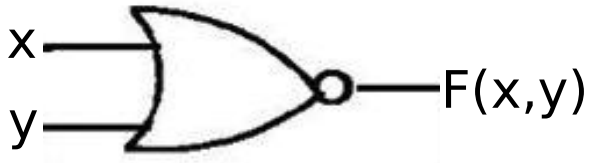

x	y	$F(x,y) = \overline{x \vee y}$
0	0	1
0	1	0
1	0	0
1	1	0

Figure 1.12 A "black-box" schematic and truth table for the classical NOR gate, where $\vee$ denotes conjunction and bar denotes negation.

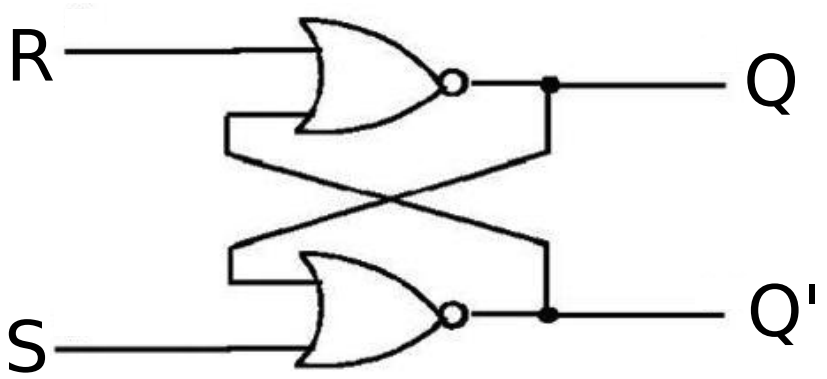

Inputs		Outputs	
R	S	Q	Q'
0	1	1	0
1	0	0	1
0	0	keep	keep
1	1	undefined	undefined

Figure 1.13 A "black-box" schematic and truth table for the classical RSFF.

equations (see [73, 118]) because resistors, capacitors, and inductors are related via different rates of change. Furthermore, *SPICE* simulations are often employed as a means of studying circuit designs, but the computational costs become unreasonable as circuits become more complex. However, more recently, there has been some effort in modeling logical circuits as simple discrete dynamical systems [56, 142, 9] and developing a mathematical framework for studying chaos in boolean networks [143, 136, 137].

1.3 Hydrodynamic Quantum Analogs

It has been known for decades that a fluid drop can be made to bounce on a vibrating fluid bath for long time scales. In recent years, bouncing droplets have been observed to bifurcate from the bouncing state (no horizontal motion) to the walking state (horizontal motion). Experiments with walking droplets (called *walkers*) exhibit analogs of wave-particle duality and more specifically quantum-like phenomena. Studying walkers can enhance our understanding of quantum mechanics and suggest viable alternatives to the Copenhagen interpretation, the idea that quantum particle dynamics depend on their probability wave, in the form of pilot wave theory.

Pilot wave theory is based upon the idea that particle trajectories drive the statistics seen in quantum mechanics. In the early days of quantum mechanics it was seen as a promising explanation of the statistics arising in experiments. Specifically the works of de Broglie [35] and later Bohm [10], while very different, showed potential as alternate formulations to that of the Copenhagen interpretation. As J.S. Bell said in [4],

> *De Broglie showed in detail how the motion of a particle, passing through just one of two holes in screen, could be influenced by waves propagating*

through both holes. And so influenced that the particle does not go where the waves cancel out, but is attracted to where they cooperate. This idea seems to me so natural and simple, to resolve the wave-particle dilemma in such a clear and ordinary way, that it is a great mystery to me that it was so generally ignored.

In recent years, fluid dynamic experiments with droplets bouncing on a vibrating bath were observed to exhibit quantum-like behavior. This effectively revived the theory in the form of hydrodynamic quantum analogs and catalyzed the current very active state of walking droplet research. In 2005 Couder and collaborators observed droplets moving across a vibrating fluid bath [28]. The droplets accomplish this by exciting an eigenmode at each bounce, which generates a wave field, and in turn are propelled by interacting with this field [28, 133]. Later, Couder *et al.* [27] and Eddi *et al.* [40, 41] observed quantum-like behavior such as single particle diffraction, tunneling, and the Zeeman effect. Furthermore, there were extensive experiments conducted on the quantization of orbits by Fort *et al.* [48], Harris *et al.* [59, 58], and Perrard *et al.* [128, 127].

The experimental work led to many mathematical models. Discrete path memory models (accompanied by experimental results) for quantized circular orbits and walking in free space were developed by Fort *et al.* [48] and Eddi *et al.* [42], respectively. A detailed hydrodynamic model derived from free space experiments was developed by Molacek *et al.* [106]. Oza *et al.* took this further and developed integro-differential equation models for walkers in free space [120] and a circular rotating frame [119, 121]. Then more accurate models for the waves were developed by Milewski *et al.* [103] and coupled with the equations of motion of the droplet.

While many of these models agree very well with experiments, the equations are quite difficult to study analytically. The complexity of the equations naturally created interest in developing realistic simplified mathematical models exhibiting important

dynamical features of the original ones, while being easier to analyze. The first models to exploit the discrete nature of the bouncing/walking were developed by Fort *et al.* [48] and later Eddi *et al.* [42]. Several other such reduced models were developed and two of them, devised by Shirokoff [146] and Gilet [49], are planar discrete dynamical system models. Shirokoff [146] developed a model in which he derived a map for the motion of a particle in a square cavity. In this model, using numerics, he discovered the cascading period doubling bifurcations indicative of chaos. Gilet [49] included the amplitude of subsequent modes in his model for the straight line motion of a particle. He observed what appeared to be a Neimark– Sacker (N-S) bifurcation in numerous simulations, and so conjectured its existence and type. We prove these conjectures and other results in [135].

A summary of quantum-like behavior in experiments of walking droplets and recent theoretical developments for hydrodynamic pilot wave theory can be found in [12, 14, 13].

1.4 Summary and Overview

This dissertation discusses the role of dynamical systems theory in studying chaotic logical circuits and walking droplets. It encompasses the entire spectrum of applied mathematics from experimentation, to modeling, to detailed theoretical analysis, and even some computation and coding. This effectively separates the thesis into two main parts, logical circuits and walking droplets, and three subparts, experiments, modeling, and analysis, which are intended to give the reader a complete scientific account of recent developments in the fields of chaotic logical circuits and walking droplets.

We begin with circuit experiments in Chapter 2 where we first give brief overviews of previous chaotic logical circuit experiments and their *SPICE* simulations, and then discuss our experiments [137] on the dual NOR gate and RS flip-flop in detail. Chapter 3 outlines a differential equation model developed for the autonomous flip-flop [118]. We derive the model in a slightly different manner from the original study. Then using standard dynamical systems techniques, different from those used by Okazaki *et al.* in [118], we arrive at the same results as that study.

Discussion of our modeling framework begins in earnest from Chapter 4. We delineate both our naïve (Section 4.1) [136] and mechanistic (Section 4.2) [137] modeling techniques and also provide analysis of the basic properties. The detailed dynamical systems analysis of the relevant models are in Chapters 5 and 6. In Chapter 5 we prove the existence of a variety of paths to chaos by embedding topological objects designed to replicate the effects of different combinations of op-amps. This chapter is a mathematical exploration of the possibilities through a naïve unphysical model rather than creating a predictive modeling framework. Predictive circuit models are discussed in Chapter 6. Here the analysis is simpler, but the models behave according to physical properties observed in experiments, which rectifies the gap between the mathematics and the physics from the previous chapter.

Then the story transitions to walking droplets; first with experiments in Chapter 7. Here we discuss four hydrodynamic quantum analog experiments: single particle diffraction [27], circular corral [59], rotating frame [58], and annular region [44]. Then in Chapter 8, Oza's integro-differential models for the trajectory of walkers are described and the linear stability analysis is reproduced from [120, 119, 121].

Our discussion of discrete dynamical walker models begin in Chapter 9. We present Shirokoff's model briefly (Section 9.1) [146] and Gilet's model (Section 9.2) [49], providing our analysis of their basic dynamical properties [135]. We then show

our detailed analysis of Gilet's model for walkers in Chapter 10. This includes a new global bifurcation that we are currently investigating.

Finally, we conclude with a summary and outline of future work in chapter 11. For logical circuits we are currently investigating the possibility of constructing a circuit analog of neuronal networks and we have a method for chaotic encryption via the chaotic RS flip-flop. We show a "proof of concept" example of chaotic encryption implemented in a MATLAB code (relegated to Appendix A) using our mechanistic model for the RS flip-flop. For walking droplets the role of dynamical systems is to connect the analysis with physical experiments. By studying dynamical properties, especially the paths to chaos, of effective models one can tune the experiments to give the desired statistics, namely the statistics observed in quantum mechanics. In essence we would reverse engineer the experiments, which may then reveal unforeseen consequences of the pilot wave interpretation of quantum mechanics.

CHAPTER 2

CHAOTIC LOGICAL CIRCUITS EXPERIMENTS

In this Chapter, experiments and *SPICE* simulations of the autonomous flip-flop (Section 2.1), a chaotic NOR gate (Section 2.2), and a chaotic set/reset (RS) flip-flop (Section 2.3) are summarized. In addition we give a detailed description of our dual NOR gate/RS flip-flop experiment (Section 2.3.2) [137] are discussed. We choose these logical circuits due to their sophisticated logical behavior and inherent chaos.

2.1 Autonomous Flip-flop

A particularly interesting autonomous flip-flop was designed and studied by Okazaki *et al.* [118]. They use six main components: a linear resistor, an inductor, two capacitors, and two nonlinear resistors. The construction is similar to Chua's circuit with an additional nonlinear resistor, and both nonlinear resistors are looped with both capacitors. The schematic is shown in Figure 2.1.

The voltage difference for the main circuit is produced by a battery. Then the voltages of the two capacitors are measured and plotted (shown in Figure 2.2 (left)). This is effectively a two dimensional projection of the associated ODE phase-space. From this phase-plane diagram, Okazaki *et al.* approximate the iterates of a Poincaré map as shown in Figure 2.2 (right). Since this is the only chaotic logical circuit in the literature for which a Poincaré map is provided, we shall refer back to it to compare the qualitative behavior of threshold control units in later sections.

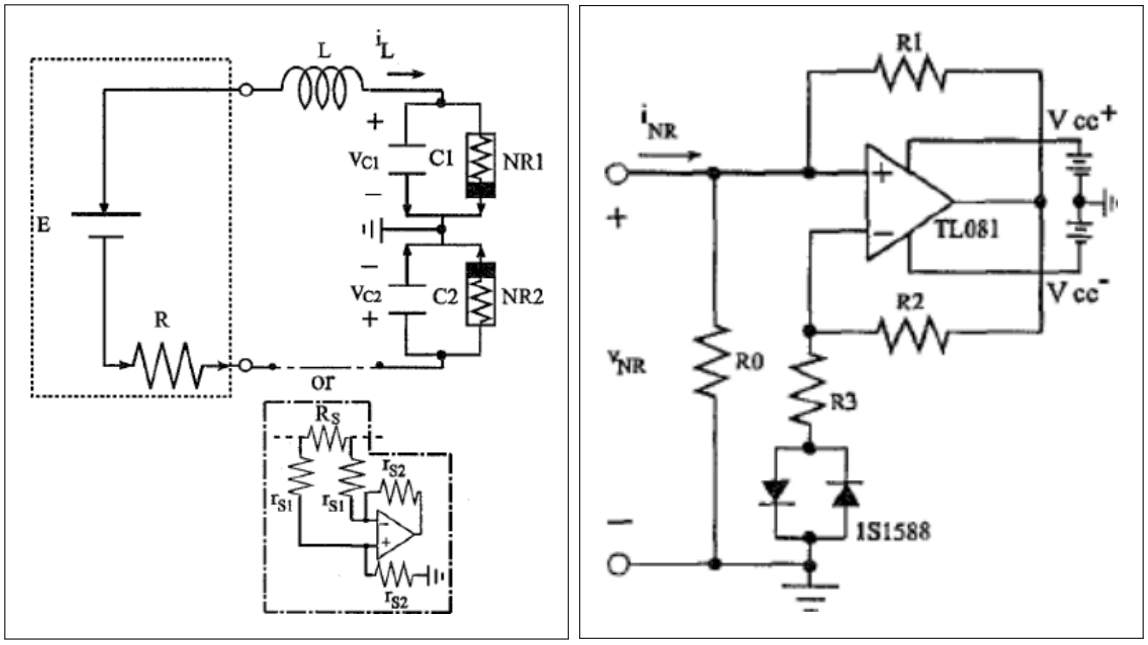

Figure 2.1 Left: Schematic of autonomous flip-flop with nonlinear resistor implicitly shown. Right: Explicit schematic of nonlinear resistor. (Reproduced under *IEEE* thesis permissions).

Source: H. Okazaki, H. Nakano, and T. Kawase. Chaotic and bifurcation behavior in an autonomous flip-flop circuit using piecewise linear tunnel diodes. *Circ. Syst.*, 3: 291-297, 1998.

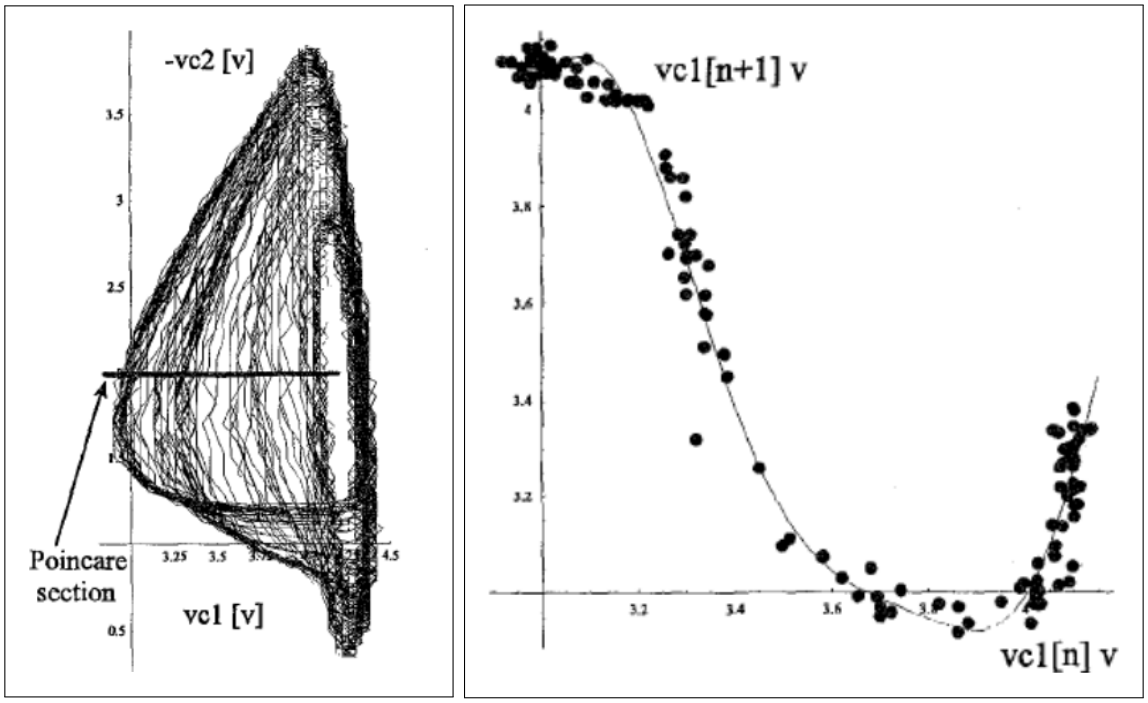

Figure 2.2 Plots of experimental data for the autonomous flip-flop circuit. Left: Projection of chaotic attractor onto the plane. Right: Approximate Poincareé Map resulting from the Poincareé section on the attractor. (Reproduced under *IEEE* thesis permissions).

Source: H. Okazaki, H. Nakano, and T. Kawase. Chaotic and bifurcation behavior in an autonomous flip-flop circuit using piecewise linear tunnel diodes. *Circ. Syst.*, 3: 291-297, 1998.

2.2 NOR Gate

As the methods for controlling chaotic circuits became more sophisticated [123, 31], electrical engineers started designing more complex logical circuits. One such circuit is the *NOR gate*, which can be combined with other NOR gates to make all other gates. The first implementation of the NOR gate was developed by Murali *et al.* in [111, 110]. They use Chua's circuit as the foundation and construct a threshold control unit (TCU) in order to produce the NOR outputs. A "black-box" and full schematics are shown in Figure 2.3.

From the schematic, this circuit and its inputs are far more complex than the autonomous flip-flop of Okazaki *et al.* . In order to cycle through all of the acceptable inputs to test the NOR gate, the authors choose to use two clocked signals, produced using alternating current, for which one has twice the frequency of the other. Both of these inputs are connected to the TCU. Depending on the inputs and output voltage, the TCU produces a voltage difference in the Chua circuit and simultaneously attempts to synchronize the threshold voltage with the first capacitor. The output is then measured at the node, V_0. This is shown in Figure 2.4.

We observe that the threshold voltage is seemingly random, when both inputs are set to unity, in addition to the low incident noise. This indicates that the system may be chaotic. We also observe that the threshold voltage tries to synchronize with the capacitor voltage, which leads to competition, the result of which produces damped oscillations in the output voltage during transitions in the clock cycle.

This NOR gate construction motivates the set/reset flip-flop construction in the next section.

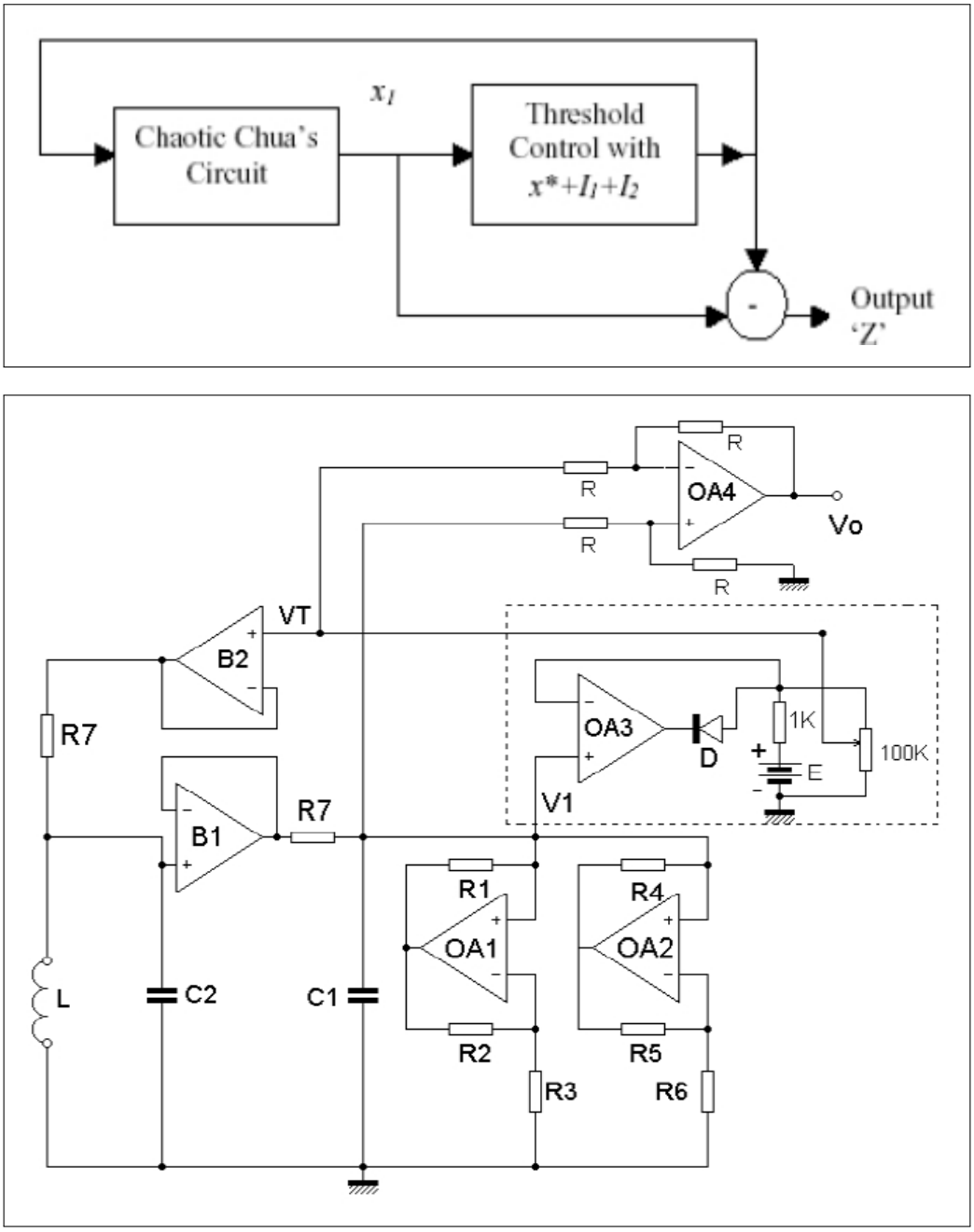

Figure 2.3 Schematics of a chaotic NOR gate. Top: "Black-box" schematic. Bottom: Full schematic. (Reproduced with permission from *World Scientific Publishing Co., Inc.*).

Source: K. Murali, S. Sinha, and W. Ditto. Implementation of a NOR gate by a chaotic Chua circuit. *Int. J. Bifurcat. Chaos*, 13: 2669-2672, 2003.

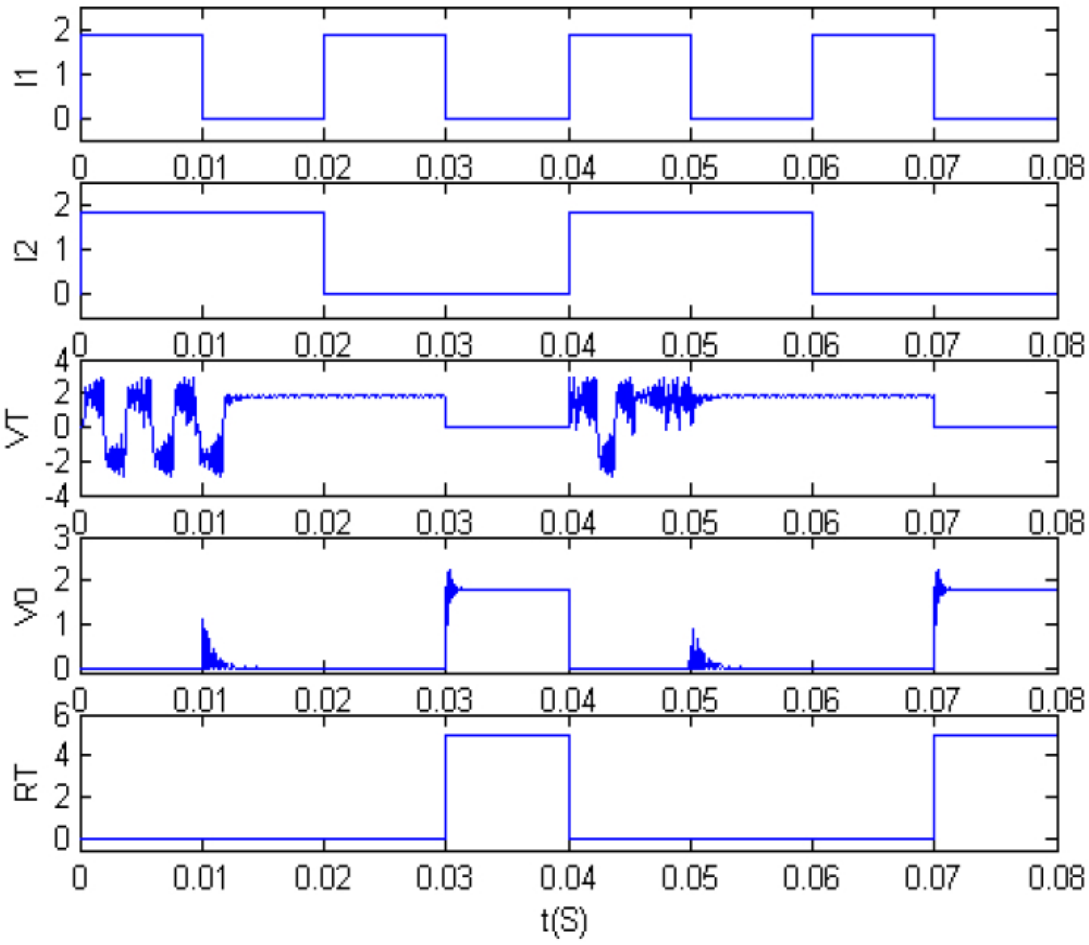

Figure 2.4 SPICE simulation plots of the two input voltages, threshold voltage, output voltage, and expected output voltage. (Reproduced with permission from *World Scientific Publishing Co., Inc.*).

Source: K. Murali, S. Sinha, and W. Ditto. Implementation of a NOR gate by a chaotic Chua circuit. *Int. J. Bifurcat. Chaos*, 13: 2669-2672, 2003.

2.3 Set/Reset Flip-flop

In this section, we discuss previous *PSPICE* (a *SPICE* based software) simulations for a chaotic set/reset flip-flop (RSFF) construction and present our own experimental results to demonstrate the robustness of the circuit design even in the midst of chaos.

2.3.1 Cafagna-Grassi Simulations

Murali *et al.* developed and tested a chaotic NOR gate construction in [111] and with more detail in [110]. Then Cafagna and Grassi designed an RSFF [16] using similar principles to the NOR gate of Murali *et al.*, which is the inspiration for our own RSFF.

The RSFF is designed with Chua's circuit at its core and two TCUs to realize each NOR gate. Two switches are used to convert the circuit from operating as two separate NOR gates to operating as an RSFF and vice versa. Cafagna and Grassi plot the *PSPICE* simulations of the inputs, outputs, and threshold voltages for both NOR gates, the inputs and outputs of the RSFF, and finally the voltages across the two capacitors [16]. In the next section we present our design and experiments of the RSFF showing similar plots and making comparisons with the previous investigation.

2.3.2 Rahman – Jordan – Blackmore

Since the circuit of Cafagna and Grassi [16] uses components that have become unavailable, we needed to design a modern chaotic RSFF/dual NOR gate. The schematic of our circuit design is shown in Figure 2.5. For the *MultiSIM* simulations we use the components shown in Table 2.1. The chaotic backbone of the circuit comes from Chua's circuit, and we employ threshold control units to produce the logical outputs. The *MultiSIM* plots for the dual NOR gate are shown in Figure 2.6. We then made a physical realization of the circuit with mostly the same components

(Table 2.1) as the *MultiSIM* (a *SPICE* based software) simulations. The experimental setup is shown in Figure 2.7. In order to power the circuit and get readings we used a DC power supply, wave form generator, *Arduino Due*®, and an oscilloscope. From the physical realization we reproduced the *MultiSIM* plots. To activate the dual NOR gate we keep switches 1 and 2 in Figure 2.5 closed and switches 3 and 4 open. The experimental results for the dual NOR gate setup are shown in Figure 2.8. In Figures 2.8c and 2.8d we notice windows of what looks like chaotic dynamics. This is also observed in the *MultiSIM* simulations. It should be noted that the threshold behavior of the *MultiSIM* circuit and the physical realization are slightly different due to a change in the operational amplifiers (op-amps). We take a detailed look at the dynamics in Section 6.2.

To deactivate the dual NOR gate we open switches 1 and 2 in Figure 2.5. To properly activate the RSFF we need to close switches 3 and 4, however we get the RSFF outputs even with the switches open. When we close the switches we notice the *race conditions* (the tendency of the two signals to have slightly different frequencies) for the "1-1" input causing wild oscillations, which is completely missed in the simulations. This shows that the design has implicit feedbacks, through the op-amps, which result in RSFF operations. However, when the two NOR gates are explicitly connected with one another (i.e., the output of one NOR gate feeds back to the input of the other NOR gate) the race condition exacerbates the oscillations. The experimental results for the RSFF setup are shown in Figure 2.9. While the experiments of the RSFF mainly work as expected, the *MultiSIM* simulations are not able to properly capture this behavior.

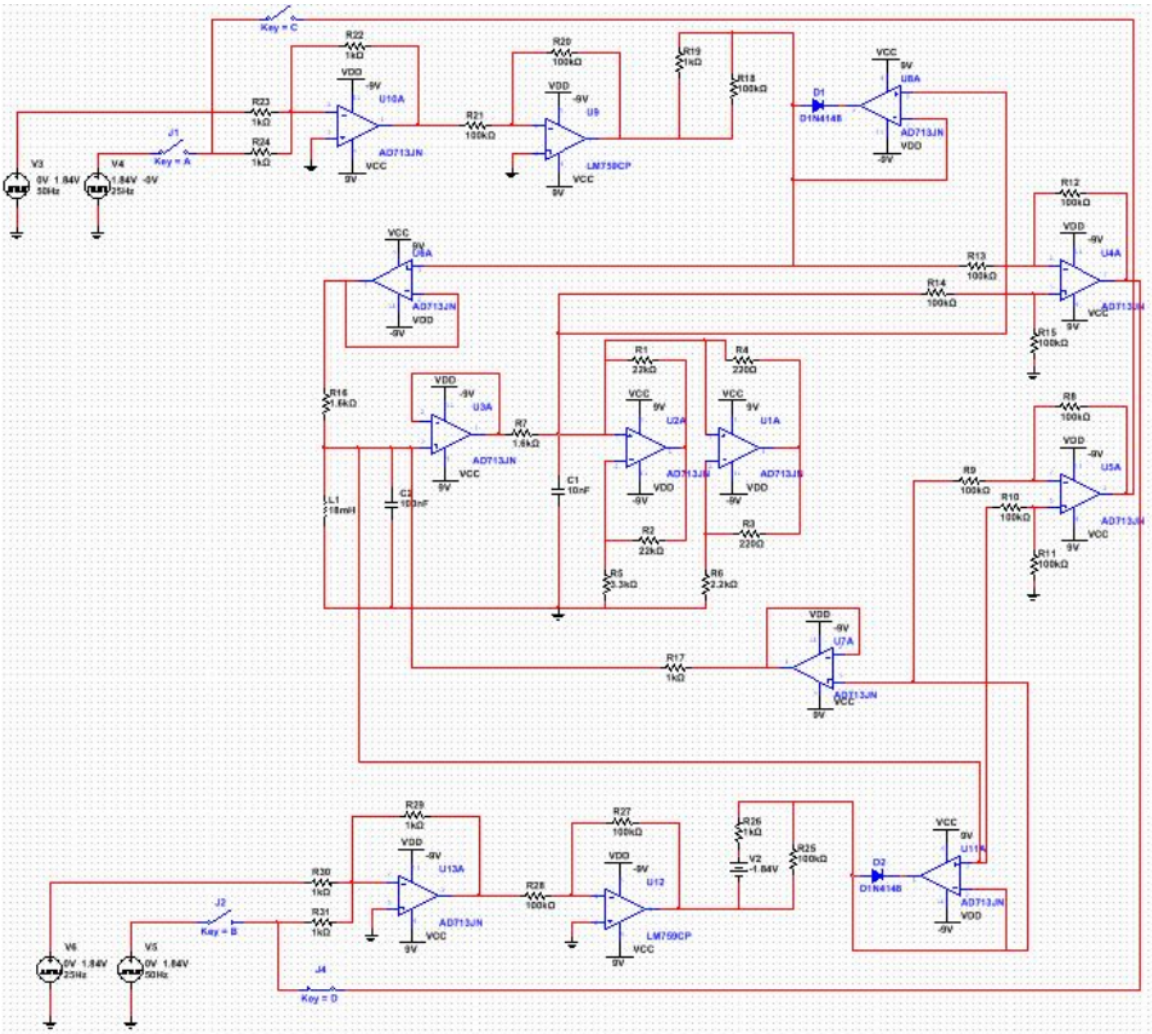

Figure 2.5 Full schematic of the RSFF/dual NOR design.

Source: A. Rahman, I. Jordan, and D. Blackmore. Qualitative models and experimental investigation of chaotic NOR gates and set/reset flip-flops. arXiv: 1702:04838, 2017.

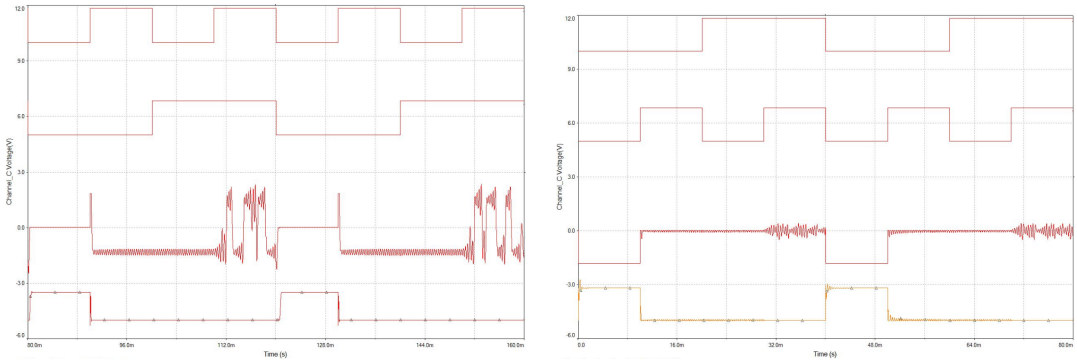

Figure 2.6 *MultiSIM* plots of the two input voltages, threshold voltage, and output voltages for the two separate NOR gates.

Source: A. Rahman, I. Jordan, and D. Blackmore. Qualitative models and experimental investigation of chaotic NOR gates and set/reset flip-flops. arXiv: 1702:04838, 2017.

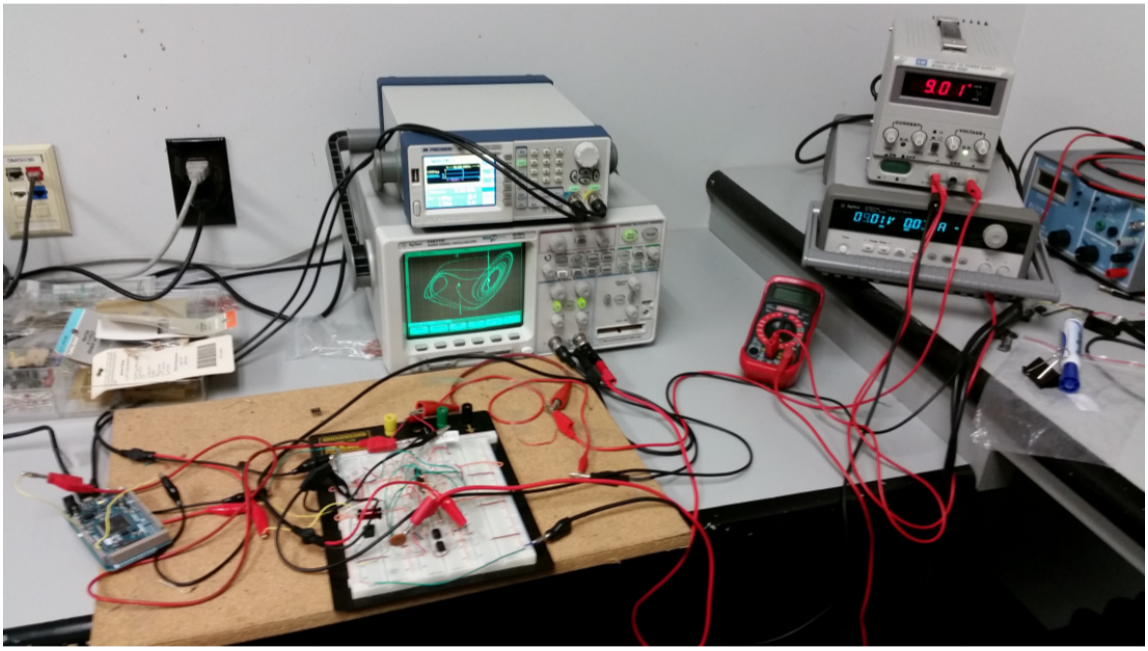

Figure 2.7 Experimental setup of dual NOR gate and RS flip-flop.

Source: A. Rahman, I. Jordan, and D. Blackmore. Qualitative models and experimental investigation of chaotic NOR gates and set/reset flip-flops. arXiv: 1702:04838, 2017.

Table 2.1 List of Components for Dual NOR Gate and RS Flip-flop

Type	Quantity	Code	Comments
$1k\Omega$ Resistor	9		
$100k\Omega$ Resistor	14		
$1.6k\Omega$ Resistor	2		
$22k\Omega$ Resistor	2		
$220k\Omega$ Resistor	2		
$2.2k\Omega$ Resistor	1		
$3.3k\Omega$ Resistor	1		
$100nF$ Capacitor	1		
$10nF$ Capacitor	1		
$18mH$ Inductor	1		
Op-Amp	6	AD713JN	Used in *MultiSIM*
Op-Amp	1	LM759CP	Used in *MultiSIM*
Op-Amp	7	NTE858m	Used in physical realization

Source: A. Rahman, I. Jordan, and D. Blackmore. Qualitative models and experimental investigation of chaotic NOR gates and set/reset flip-flops. arXiv: 1702:04838, 2017.

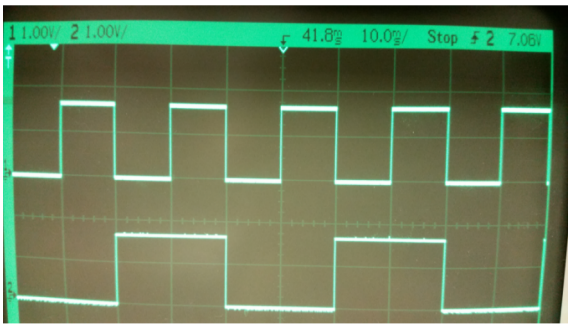

(a) Inputs

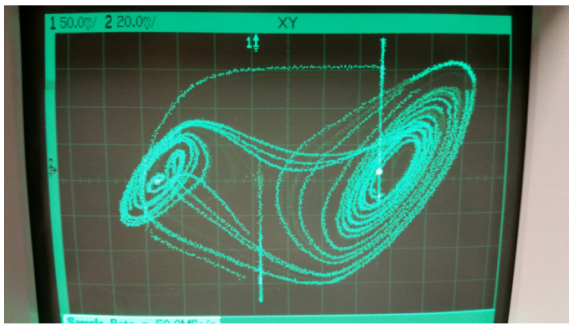

(b) Capacitor voltages

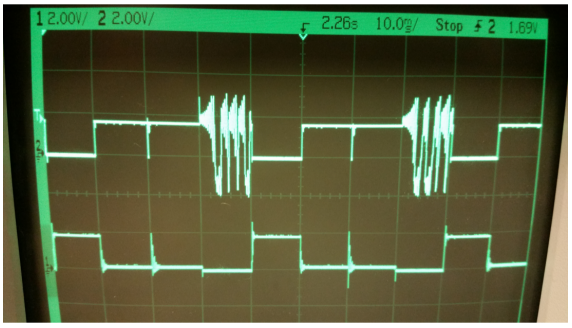

(c) Threshold 1 and NOR output 1

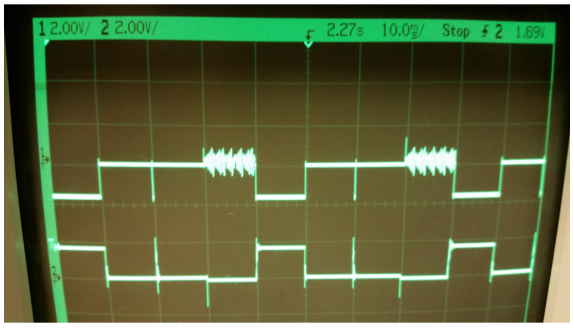

(d) Threshold 2 and NOR output 2

Figure 2.8 Experimental results for the dual NOR gate setup. For (a), (c), and (d) the abscissa represents time and the ordinate represents voltage. In (b) the plot shows the phase space produced by the two capacitors. In (a) the plot shows the two input voltages. In (c) and (d) the plot shows the respective threshold voltage and NOR outputs.

Source: A. Rahman, I. Jordan, and D. Blackmore. Qualitative models and experimental investigation of chaotic NOR gates and set/reset flip-flops. arXiv: 1702:04838, 2017.

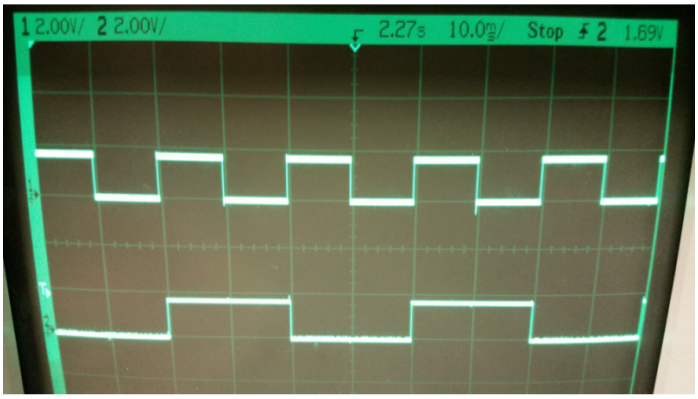

(a) Inputs

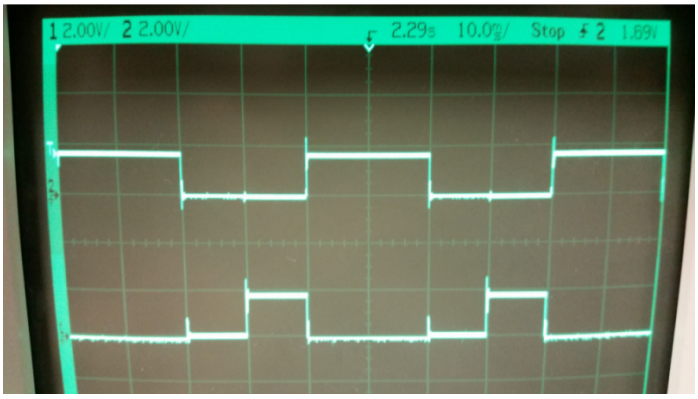

(b) Output without explicit feedback

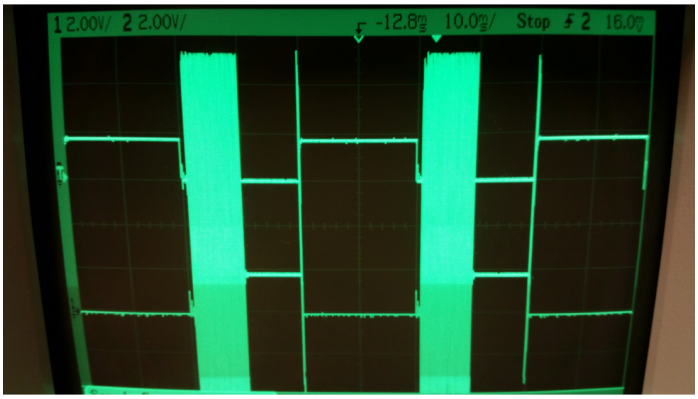

(c) Output with explicit feedback

Figure 2.9 Experimental results for the RSFF setup. For (a), (b), and (c) the abscissa represents time and the ordinate represents voltage. In (a) the plot shows the two input voltages. In (b) the voltage was measured when switches 3 and 4 in Figure 2.5 are open. In (c) the voltage was measured when switches 3 and 4 in Figure 2.5 are closed.

Source: A. Rahman, I. Jordan, and D. Blackmore. Qualitative models and experimental investigation of chaotic NOR gates and set/reset flip-flops. arXiv: 1702:04838, 2017.

CHAPTER 3

TRADITIONAL MODELING TECHNIQUES: AUTONOMOUS FLIP-FLOP

The autonomous flip-flop in [118] was designed to reproduce behavior of a specific family of ODEs in an electrical system. Essentially, they had the model before designing the circuit, however the concepts one would use to go from the physical circuit to the model are commonly used for other circuits and are easy to delineate. In this section, we perform the useful exercise of deriving the model from the circuit elements. We also analyze the model through predominantly algebraic techniques, whereas Okazaki *et al.* used mainly qualitative geometric arguments.

3.1 Description

In order to model most electronic circuits, we must apply Kirchhoff's laws. Kirchhoff's current law states that the sum of all currents entering (exiting is entering with a minus sign) a node is zero. Furthermore, Kirchhoff's voltage law states that the voltages in a closed loop sum to zero. Now, we refer to Figure 2.1. First we study the large loop, which consists of the voltage source, an inductor, two capacitors, and a resistor. Let the voltage across the capacitors be denoted as v_1 and v_2, the resistance of the resistor as R, the voltage generated by the voltage source as E, the inductance as L, and the current through the inductor as Z. This gives us the equation,

$$L\frac{dZ}{dt} = E - RZ - v_1 + v_2.$$

Next, we derive the equations for the top and bottom nodes (notice that the middle node is grounded, i.e., zero voltage), which is done simultaneously. The only difference between the two nodes is the direction of the current, Z. First, let the current of the nonlinear resistors, represented by f, be a function of voltage, namely the voltages across the capacitors. Then, let the capacitances of the capacitors be C_1 and C_2. This gives us the equations,

$$C\frac{dv_1}{dt} = Z - f(v_1)$$
$$C\frac{dv_2}{dt} = -Z - f(v_2)$$

Then the full system is

$$\begin{aligned} C\frac{dv_1}{dt} &= Z - f(v_1), \\ C\frac{dv_2}{dt} &= -Z - f(v_2), \\ L\frac{dZ}{dt} &= E - RZ - v_1 + v_2; \end{aligned} \tag{3.1}$$

which is precisely the equations that were studied by Okazaki *et al.* [118]. As in [118] this can be nondimensionalized using $x = v_1/V_{\max}$, $y = -v_2/V_{\max}$, $z = Z/Z_{\max}$, $\rho = R/R_{\max}$ ($R_{\max} = V_{\max}/Z_{\max}$), and $\eta = E/V_{\max}$. Some of the less intuitive nondimensional quantities are the natural frequency, $\omega = \sqrt{1/C_1L + 1/C_2L}$, the time constant, $T = \omega t$, the nondimensionalized function for the nonlinear resistors, $F(\{\cdot\}) = f(\{\cdot\}V_{\max})/Z_{\max}$, and the derived nondimensional parameters, $B_1 = 1/(R_{\max}\omega C_1)$ and $B_2 = 1/(R_{\max}\omega C_2)$. Finally, (3.1) takes the nondimensional matrix form,

$$\begin{pmatrix} \dot{x} \\ \dot{y} \\ \dot{z} \end{pmatrix} = \Phi(x, y, z) = \begin{pmatrix} B_1(z - F(x)), \\ B_2(z - F(y)), \\ \frac{\eta - \rho z - x - y}{B_1 + B_2}. \end{pmatrix} \tag{3.2}$$

This is the model we analyze below.

3.2 Basic Properties

While Okazaki *et al.* gave a graphical representation of the fixed points [118], it is not difficult to explicitly derive the equations, the roots of which are the fixed points,

$$z_* - F(x_*) = 0, \quad z_* - F(y_*) = 0; \qquad \eta - \rho z_* - x_* - y_* = 0.$$

The first two equations give us, $x_* = F^{-1}(z_*)$ and $y_* = F^{-1}(z_*)$, which implies $x_* = y_*$. Using these three conditions we get

$$\eta - \rho F(x_*) - 2x_* = 0, \tag{3.3}$$

$$\eta - \rho F(y_*) - 2y_* = 0, \tag{3.4}$$

$$\eta - \rho z_* - 2F^{-1}(z_*) = 0. \tag{3.5}$$

Using these equations we can solve for F and F^{-1} in terms of their arguments,

$$F(x_*) = -2x_*/\rho + \eta/\rho \tag{3.6}$$

$$F(y_*) = -2y_*/\rho + \eta/\rho \tag{3.7}$$

$$F^{-1}(z_*) = -\rho z_*/2 + \eta/2 \tag{3.8}$$

From [118] we know that F is increasing and piece-wise-linear, hence so is f^{-1}. Furthermore, since $F(0) = 0$, F and F^{-1} will have the same signs as their respective arguments. Also recall, η and ρ are positive parameters. From (3.8), since the the lines intersect the ordinate in the positive half and the slopes are negative, all the fixed points must lie in the first octant, and by symmetry, the seventh octant.

Next, we find the Jacobian of Φ,

$$D\Phi(x,y,z) = \begin{pmatrix} -B_1F'(x) & 0 & B_1 \\ 0 & -B_2F'(y) & B_2 \\ -1/(B_1+B_2) & -1/(B_1+B_2) & -\rho/(B_1+B_2) \end{pmatrix} \tag{3.9}$$

Evaluating at the fixed points and taking the determinant gives,

$$\begin{aligned} |D\Phi(x_*,x_*,z_*) - \lambda I| &= \begin{pmatrix} -B_1F'(x_*) - \lambda & 0 & B_1 \\ 0 & -B_2F'(x_*) - \lambda & B_2 \\ -1/(B_1+B_2) & -1/(B_1+B_2) & -\rho/(B_1+B_2) - \lambda \end{pmatrix} \\ &= -\lambda^3 - [(B_1+B_2)F'(x_*) + \rho/(B_1+B_2)]\lambda^2 \\ &\quad - [B_1B_2F'(x_*)^2 + \rho F'(x_*) + 1]\lambda - \frac{B_1B_2F'(x_*)(\rho F'(x_*)+2)}{B_1+B_2} \end{aligned}$$

Finding the roots of the cubic polynomial through numerical means yields a convoluted result. One may attempt to compute the determinant to extract more information about the fixed points, and can employ the RouthHurwitz stability criterion [141, 70] to aid the stability analysis. However, doing this would require lengthy calculations for very little information, which is why Okazaki *et al.* chose to use mainly numerical simulations to compare their model to the experiments.

3.3 Simulations

Okazaki *et al.* integrated (3.2) and projected the phase space onto the voltage-voltage plane just as in Section 2.1. Furthermore, they also approximated the Poincaré map using the same ordinate value as in Section 2.1. While these techniques are useful, they only work with simple circuits. As the circuits become more complex so do the

usual dynamical systems techniques. The difficulty in analyzing certain 3-dimensional systems motivates a search for simpler models in Chapter 4.

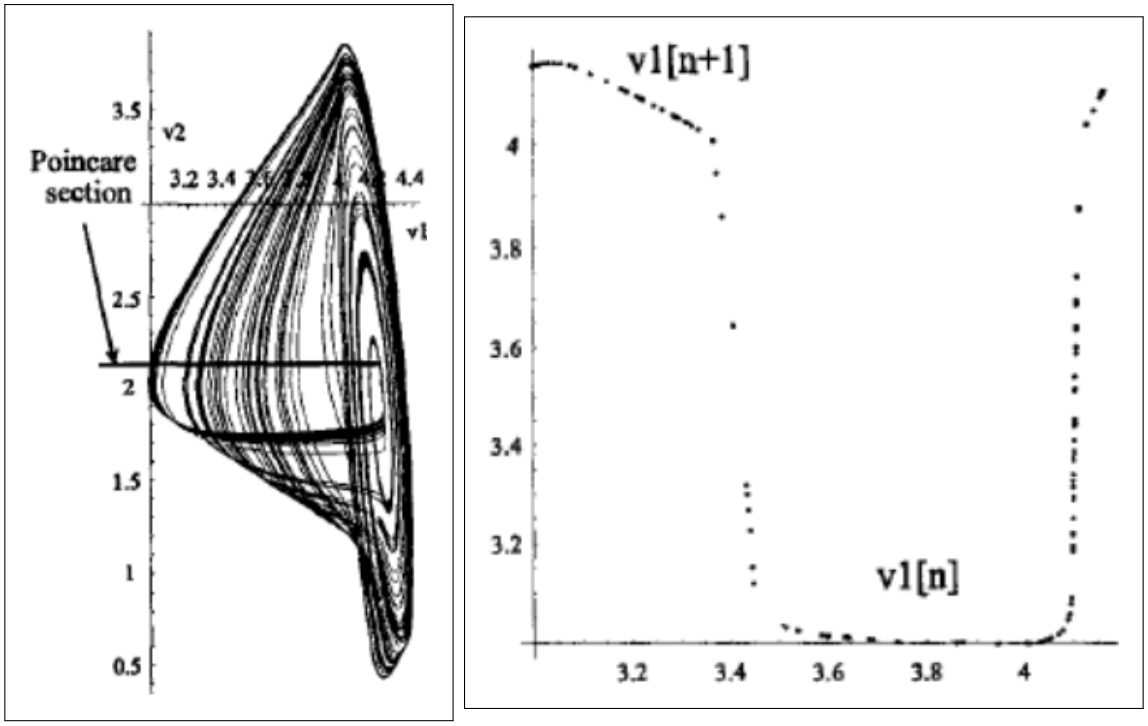

Figure 3.1 Plots of simulation data for the autonomous flip-flop circuit. Left: Projection of the chaotic attractor onto the plane. Right: Approximate Poincareé map resulting from the Poincareé section on the attractor. (Reproduced under *IEEE* thesis permissions).

Source: H. Okazaki, H. Nakano, and T. Kawase. Chaotic and bifurcation behavior in an autonomous flip-flop circuit using piecewise linear tunnel diodes. *Circ. Syst.*, 3: 291-297, 1998.

CHAPTER 4

DISCRETE DYNAMICAL MODELS: CHAOTIC LOGICAL CIRCUITS

There are several connections between the solutions of the model ODEs and iterates of maps that can be used for dynamical comparisons, among which are the following: As observed by Hamill *et al.* [56], the autonomous nature of the logical circuit equations allows dynamical analysis via the iterates (snapshots) of a fixed time map, which can be reduced to a planar map in special cases as shown in Kacprzak and Albicki [74] and Kacprzak [73]. In addition, the application of a standard explicit one-step integration method is tantamount to the iteration of the map describing the scheme, thus enabling the (approximate) reduction from a continuous to a discrete dynamical system as shown, *e.g.* by Danca [34]. Of course, there is the well-known method of employing Poincaré sections to analyze three-dimensional continuous dynamical systems using two-dimensional discrete dynamical systems, which has been employed in numerous investigations of chaotic logical circuit realizations such as Murali *et al.* [111, 110], Okazaki *et al.* [118] and Ruzbehani *et al.* [142]. As it turns out, chaotic logical circuits can be realized using the circuit of Chua and its generalizations [23, 25].

There is also another interesting connection between realization of chaotic logical circuits and nonlinear maps that might afford an opportunity for comparisons with the results obtained from our two-dimensional discrete dynamical system models. This nonlinear map approach has been established in the work of Ditto *et al.* [38], which features the notion of reconfigurable logic gates comprising connected NOR and NAND gates constructed using one-dimensional discrete dynamical systems and associated thresholds.

In this chapter, we derive discrete dynamical models of logical circuits, such as the NOR gate and RSFF. First we derive models using naïve simplifying assumptions (Section 4.1) [136], then we derive a mechanistic model (Section 4.2) [137]. The simplicity in our models is due to the use of continuous extensions of logical operations. In electronics nothing is quite discrete and logical operations are carried out in some continuous manner that is different for each device. Consider the NOR gate (the negation of conjunction), $F(x,y) = \overline{x \vee y}$, x, $y \in \{0,1\}$, for which $F(0,0) = 1$ and all other combinations are zero (Figure 1.12). We can continuously extend it, in the most natural manner, as $f(x,y) = (1-x)(1-y)$, x, $y \in [0,1]$. Then for x, $y \in \{0,1\}$ we achieve the same outcome. We then ask what happens if a signal traverses through the same devices as for the logical circuit inputs and outputs, but in a different order? Perhaps carefully inserted perturbations of the continuous extensions is sufficient to reproduce certain observed dynamical behavior.

4.1 Naïve Threshold Control Unit Models

To obtain the minimal discrete dynamical system model for the classical RSFF circuit (Figure 1.13), we start with the simplest continuous extension of the input/output map of the NOR gate to the unit square in the plane, which is clearly given by the function $\mathcal{N} : I^2 \ (\subset \mathbb{R}^2) \to I \ (\subset \mathbb{R})$ defined as

$$\mathcal{N}(x,y) := (1-x)\,(1-y)\,, \tag{4.1}$$

where $I^2 := I \times I := [0,1] \times [0,1] \subset \mathbb{R}^2$ is the unit square and x and y are the inputs. Observe that this quadratic function is bilinear in the variables $(1-x)$ and $(1-y)$, and behaves precisely like the pure logical NOR gate when $x, y \in \{0,1\}$. Using the functional representation (4.1) for each of the (NOR gate) components of the RSFF

circuit, we let $Q = (1-R)(1-Q')$ and $Q' = (1-S)(1-Q)$ and solve the two equations for Q and Q' obtaining the continuous extension for the RSFF (away from the origin),

$$Q := \frac{S(1-R)}{R+S-RS}, \qquad Q' := \frac{R(1-S)}{R+S-RS}. \tag{4.2}$$

Recall in Figure 1.13 we show the classical "black-box" schematic of the RSFF and the above equation matches the truth table exactly except at $R = S = 0$.

4.1.1 Derivation

Since the threshold outputs are fed back in a similar manner to the RSFF outputs, and because they both have the same edge trigger (cock cycle transition) effects neglecting the chaotic regions, we make the naïve assumption that the underlying logical behavior is preserved and we readily obtain its minimal extension to the unit square in the form of a map $F : I^2 \to I^2$ defined as

$$F = (\xi, \eta) : I^2 \left(\subset \mathbb{R}^2\right) \to I^2 \left(\subset \mathbb{R}^2\right), \tag{4.3}$$

where the coordinate functions are

$$\xi(x,y) := \frac{y(1-x)}{x+y-xy}, \qquad \eta(x,y) := \frac{x(1-y)}{x+y-xy}, \tag{4.4}$$

with the x-y-coordinates playing the roles of the previous threshold output, and ξ-η coordinates playing the roles of the current threshold output.

One might well ask what the map (4.3), which is the natural continuous extension of the exact logical circuit map defined on $\{0,1\}$, has to do with the mathematical models of physical realizations of flip-flop circuits. Typical models are in terms of systems of three nonlinear, piecewise smooth ordinary differential equations and should

have the minimal (exact logical circuit) maps approximately embedded within them – most likely as part of certain Poincaré sections. Hence, it is reasonable to assume that small C^0 perturbations of (4.3) should reflect the dynamics of possible physical realizations of flip-flop circuits to a rather significant extent.

This map generates a discrete (semi-) dynamical system in terms of its forward iterates determined by n-fold compositions of the map with itself, denoted as F^n, where $n \in \mathbb{N}$, the set of natural numbers. We shall employ the usual notation and definitions for this system; for example, the *positive semiorbit* of a point $p \in \mathbb{R}^2$, which we denote as $O_+(p)$, is simply defined as $O_+(p) := \{F^n(p) : n \in \mathbb{Z},\, n \geq 0\}$, and all other relevant definitions are standard (*cf.* [52, 75, 122, 164]). The minimal map (4.3) is real-analytic (C^ω) on I^2 except at the origin, where it is not even well-defined. Consequently, we should really consider F to be defined on $I^2 \setminus \{(0,0)\}$ and actually on $X := I^2 \setminus \{(0,0),(1,1)\}$ if we wish to avoid the origin for all forward iterates of F.

4.1.2 Basic Properties

First we take note of some of the analytical properties of the map (4.3), which are listed in what follows. The proofs of all these results are straightforward and hence left out.

(A1) The map $F \in C^\omega(X)$.

(A2) F is $\mathbb{Z}_2$-symmetric, *i.e.*, $R \circ F = F \circ R$ for the reflection R in the line $y = x$.

(A3) $F(X) = Y := \{(\xi,\eta) \in \mathbb{R}^2 : 0 \leq \xi, \eta$
and $\xi + \eta < 1\} \cup \{(1,0),(0,1)\}$.

(A4) $F((0,1] \times \{0\}) = (0,1)$, $F(\{0\} \times (0,1]) = (1,0)$, and if $\rho(a) := \{(x,ax) : 0 < x, a\} \cap X$ is the ray through the origin sans the origin in X, then $F(\rho(a)) \subset$

$\{(\xi, (a-1)+a\xi) : 0 < \xi\} \cap Y$. Moreover, as $(x, y) \to (0, 0)$ along the ray $\rho(a)$, $F(x, y)$ converges to the point of intersection of the line defined by $x + y = 1$ with the ray $\rho(1/a)$. This shows just how singular the formulas (4.3) are at the origin.

(A5) The derivative (matrix) for F on X is

$$F' = (x + y - xy)^{-2} \begin{pmatrix} -y & x(1-x) \\ y(1-x) & -x \end{pmatrix}, \tag{4.5}$$

with determinant

$$\det F'(x, y) = xy(x + y - xy)^{-3}, \tag{4.6}$$

which shows that the implicit function theorem cannot guarantee the existence of a local smooth inverse along the x- and y-axes.

(A6) In fact, the inverse of F, where it exists, is given as

$$F^{-1}(\xi, \eta) = \left(\frac{1-\xi-\eta}{1-\eta}, \frac{1-\xi-\eta}{1-\xi} \right), \tag{4.7}$$

which is clearly in $C^\omega(Y \setminus \{(1, 0), (0, 1)\})$.

These properties will be used to prove the results in Chapter 5.

4.2 Mechanistic Models

We first model NOR gates, then we use those models to model the RSFF. This is accomplished by constructing continuous extensions and approximating the behavior of the Threshold Control Units (TCUs) and Chua's circuit. We have also provided simplified schematics in Figure 4.1 to help illustrate the modeling process. It should

be noted, that while in the experiments we use a high voltage of 1.84 volts, in our models this is normalized to 1.

One may suggest solving Matsumoto's equation [99] for Chua's circuit as part of the model, and use that to model the behavior of the TCUs. While this would be a legitimate approach, the goal of the Chapter is to formulate the simplest model in terms of derivation and simulation. Having to solve the ordinary differential equation at each time step would be reasonable for a two gate circuit, but would not be scalable to large chaotic logical circuits with many gates. For these reasons, we forgo explicitly modeling the capacitor voltages, and instead develop models for the threshold voltages and the outputs, then show that the derived capacitor voltages agree reasonably well with experiments and *MultiSIM* simulations in addition to showing the threshold and outputs agree surprisingly well with the experiments and simulations.

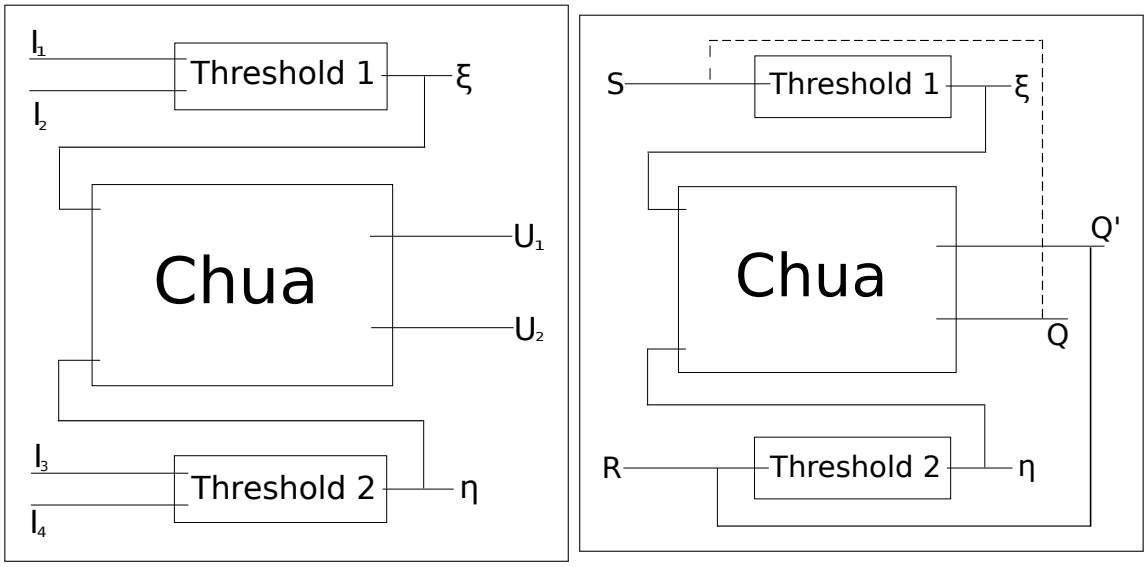

Figure 4.1 Simplified schematics of dual NOR gates (left) and RS flip-flop (right) used to illustrate the building blocks of the models.

Source: A. Rahman, I. Jordan, and D. Blackmore. Qualitative models and experimental investigation of chaotic NOR gates and set/reset flip-flops. arXiv: 1702:04838, 2017.

4.2.1 Derivation of the NOR Gate Model

Here we derive and analyze the NOR gate models. The schematic for the gates given in Figure 2.5 may be simplified to Figure 4.1 in order to get a general picture of the circuit. It should be noted that the blocks are not absolutely accurate as the block labeled "Chua" has additional op-amps compared to that of the traditional Chua circuit and feedback from the "Chua" block to the threshold blocks are not explicitly shown.

We begin by formulating the simplest continuous extension of the NOR operator: $\overline{x \vee y} = (1-x)(1-y);\ x, y \in \{0, 1\}$. This gives us the equation,

$$\begin{aligned} U_1 &= (1 - I_1)(1 - I_2), \\ U_2 &= (1 - I_3)(1 - I_4); \end{aligned} \tag{4.8}$$

where U are the respective outputs and I are the respective inputs as shown in Figure 4.1. This naïve extension is enough to approximate the behavior of the NOR gate outputs, and we shall also modify them later to simulate certain subtle aspects of the circuit. However, the more interesting dynamics are observed in the TCUs.

First, let us define the maps, $f : [0, 1]^2 \times [-2, 2] \to [-2, 2]$ and $g : [0, 1]^2 \times [-1, 1] \to [-1, 1]$, where the chosen intervals are the operating domains of the TCUs by design. We apply these maps to the inputs and current time threshold voltages to get the next time threshold voltages,

$$\begin{aligned} \xi_{n+1} &= f(I_1, I_2, \xi_n), \\ \eta_{n+1} &= g(I_3, I_4, \eta_n); \end{aligned} \tag{4.9}$$

where ξ and η are the respective threshold voltages as shown in Figure 4.1.

Next, we tabulate our observations from Figure 2.8 and 2.6 in (4.10), and formulate functions f and g that qualitatively reproduce the observed behavior. It

should be noted that, henceforth, we shall denote a seemingly random voltage (in the chaotic regime) by a star ($\star$), where $\star$ is not a number to be measured, but rather denotes chaotic behavior.

$$\begin{aligned} f(0,0,0) &= 0, & f(1,0,1) = f(0,1,1) &= 1, & f(1,1,\star) &= \star; \\ g(0,0,-1) &= -1, & g(1,0,0) = g(0,1,0) &= 0, & g(1,1,\star) &= \star. \end{aligned} \tag{4.10}$$

In order to satisfy these criteria, we first define the maps, $y_f : [-2,2] \to [-2,2]$ and $y_g : [-1,1] \to [-1,1]$, then

$$\begin{aligned} f(I_1, I_2, x_1) &:= |I_1 - I_2| + I_1 I_2 y_f(x_1), \\ g(I_3, I_4, x_2) &:= |I_3 - I_4| - 1 + I_3 I_4 y_g(x_2); \end{aligned} \tag{4.11}$$

satisfies each property except chaotic behavior.

Now, we must formulate y_f and y_g such that (4.11) reproduces the qualitative behavior of the threshold voltages for $(I_1, I_2) = (1,1)$ and $(I_3, I_4) = (1,1)$ as shown in Figure 2.8. We postulate y_f and y_g will be tent map-like, which is reasonable in the physical sense since these op-amps influence the signal in an approximately piecewise linear manner. Furthermore, the NOR gate developed by Murali *et al.* employed a TCU originally designed to produce the first few iterates of a logistic map [111], and a tent map is topologically conjugate to a logistic map. For y_f, we write

$$y_f(x) := \begin{cases} \frac{1+\mu_f}{1-\mu_f}(x + \nu_f) - \mu_f \nu_f, & x \in [-\mu_f \nu_f, -\nu_f], \\ \mu_f x, & x \in [-\nu_f, \nu_f], \\ \frac{1+\mu_f}{1-\mu_f}(x - \nu_f) + \mu_f \nu_f, & x \in [\nu_f, \mu_f \nu_f]; \end{cases} \tag{4.12}$$

and we write y_g as,

$$y_g(x) := \nu_g + \mu_g \begin{cases} 1 + x - \nu_g & \nu_g - 1 \leq x \leq \nu_g - 1/2, \\ \nu_g - x & \nu_g - 1/2 \leq x \leq \nu_g. \end{cases} \tag{4.13}$$

We illustrate (4.12) and (4.13) in Figure 4.2. In Figure 4.2a and (4.12), μ_f is the slope of the middle line segment and it also determines the slope of the other two line segments, whereas ν_f mainly affects the domain of the map. In Figure 4.2b and (4.13), μ_g is twice the height of the map, and $1 - \nu_g$ is the amount the new interval is translated from the interval $[0, 1]$. Moreover, all parameters are positive.

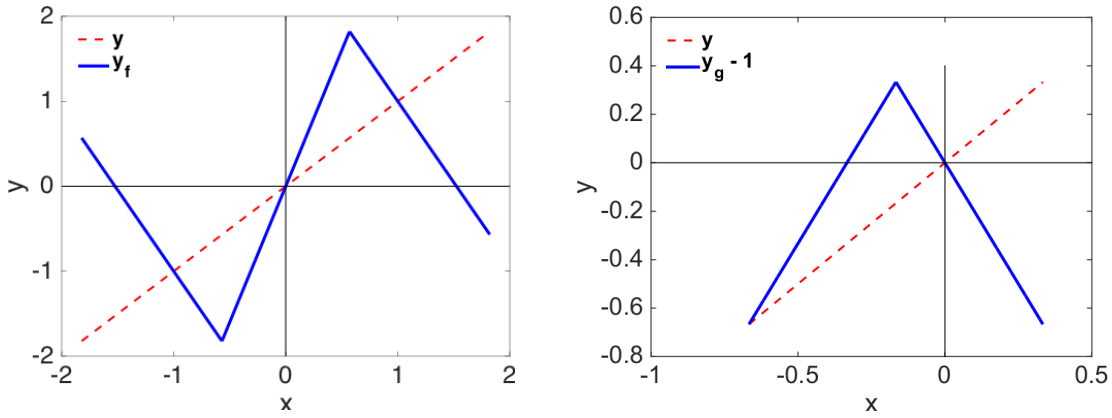

(a) Illustration of y_f.

(b) Illustration of $y_g - 1$.

Figure 4.2 Plots of y_f and y_g for fixed values of μ_f, ν_f, μ_g, ν_g.

Source: A. Rahman, I. Jordan, and D. Blackmore. Qualitative models and experimental investigation of chaotic NOR gates and set/reset flip-flops. arXiv: 1702:04838, 2017.

This gives us a model of the thresholding in the two NOR gate operation of the circuit.

Basic Properties. Since the interesting behavior arises for $(I_1, I_2) = (1, 1)$ and $(I_3, I_4) = (1, 1)$, it suffices to analyze $f(1, 1, x)$ and $g(1, 1, x)$. First we search for the

fixed points. From empirical observations we require $g(1,1,x)$ and $f(1,1,x)$ to have a fixed point at the origin and $f(1,1,x)$ to have two other nonzero fixed points. By definition, the latter has a fixed point at the origin and two nonzero fixed points. However, for the former, we require the right branch to intersect the origin. In order to achieve this, we set $g(1,1,x) = x = 0$ for $x \in [\nu_g - 1/2, \nu_g]$ (the right branch),

$$0 = -1 + \nu_g + \mu_g\nu_g \Rightarrow \nu_g = \frac{1}{1+\mu_g}.$$

Furthermore, in order to ensure the inequality, $\nu_g - \frac{1}{2} \leq x \leq \nu_g$, we require $\nu_g \leq \frac{1}{2}$, i.e., $\mu_g \geq 1$.

Now let us identify any additional fixed points of $g(1,1,x)$, which necessarily lie on the left branch, i.e., $x \in [\nu_g - 1, \nu_g - 1/2]$,

$$\begin{aligned} x_* &= -1 + \nu_g + \mu_g - \nu_g\mu_g + \mu_g x_* \\ \Rightarrow (1-\mu_g)x_* &= -1 + \frac{1}{1+\mu_g} + \mu_g - \frac{\mu_g}{1+\mu_g} = -(1-\mu_g) + \frac{1-\mu_g}{1+\mu_g} \\ \Rightarrow x_* &= -1 + \frac{1}{1+\mu_g} = -\frac{\mu_g}{1+\mu_g} = \nu_g - 1. \end{aligned}$$

Next, we identify the two nonzero fixed points of $f(1,1,x)$. For $x \in [\pm\nu_f, \pm\nu_f\mu_f]$,

$$\begin{aligned} x_* = \frac{1+\mu_f}{1-\mu_f}x_* \pm \left(\mu_f\nu_f - \nu_f\frac{1+\mu_f}{1-\mu_f}\right) \Rightarrow \left(\frac{-2\mu_f}{1-\mu_f}\right)x_* &= \mp\nu_f\frac{1+\mu_f^2}{1-\mu_f} \\ \Rightarrow x_* &= \pm\nu_f\frac{1+\mu_f^2}{2\mu_f}. \end{aligned}$$

We summarize the fixed point analysis in Table 4.1.

To analyze the stability of the fixed points of $g(1,1,x)$, let us take the derivative,

$$\frac{dg(1,1,x)}{dx} = \begin{cases} \mu_g & \nu_g - 1 \leq x \leq \nu_g - 1/2, \\ -\mu_g & \nu_g - 1/2 \leq x \leq \nu_g; \end{cases} \tag{4.14}$$

Both fixed points are sources when $\mu_g > 1$. For $\mu_g = 1$, there is a line of fixed points on the left branch such that constitutes a global attracting set. Clearly, this case is unphysical, and hence we require $\mu_g > 1$.

Taking the derivative for $f(1, 1, x)$ gives,

$$\frac{df(1,1,x)}{dx} = \begin{cases} \frac{1+\mu_f}{1-\mu_f} & x \in [-\mu_f\nu_f, -\nu_f], \\ \mu_f & x \in [-\nu_f, \nu_f], \\ \frac{1+\mu_f}{1-\mu_f} & x \in [\nu_f, \mu_f\nu_f]; \end{cases} \tag{4.15}$$

By definition, $\mu_f \geq 1$, since otherwise the two outer branches would be undefined. If $\mu_f = 1$, there is a line of fixed points on the middle branch, and hence this too is unphysical. Therefore, we require $\mu_f > 1$, which shows the origin is a source. The other two fixed points are sinks if $(1 + \mu_f)/(1 - \mu_f) < -1$, and sources if $(1+\mu_f)/(1-\mu_f) > -1$. Notice that $(1+\mu_f)/(1-\mu_f) = -1$ only when $\mu_f = 0$, which we showed was not permissible. Now, if $(1 + \mu_f)/(1 - \mu_f) < -1$, $1 < -1$, which is false. If $(1 + \mu_f)/(1 - \mu_f) > -1$, $1 > -1$, which is true. Therefore, each of the fixed points is always a source.

The fixed points along with the conditions on the parameters required to yield physical results are summarized in the table below,

These properties will be used to analyze the TCU models in greater depth in Chapter 6.

4.2.2 Derivation of a Deterministic Set/Reset Flip-flop Model

Now that we have a model for the NOR gates we can derive the model of the RSFF. Just as with the NOR gate, we sketch a simplified schematic of the RSFF in Figure 4.1. For the traditional RSFF, the output from each NOR gate is fed back into the other. Therefore, we replace I_1 and I_3 with R and S and I_2 and I_4 with Q and Q' in

Table 4.1 Summary of Fixed Points and Conditions on Parameters to Cause All Fixed Points to be Sources

Equation	Fixed points	Conditions
$g(1,1,x)$	$x_* = 0,\ -\dfrac{\mu_g}{1+\mu_g}$	$\mu_g > 1$
$f(1,1,x)$	$x_* = 0,\ \pm\nu_f \dfrac{1+\mu_f^2}{2\mu_f}$	$\mu_f > 1$ and $\nu_f > 0$

Source: A. Rahman, I. Jordan, and D. Blackmore. Qualitative models and experimental investigation of chaotic NOR gates and set/reset flip-flops. arXiv: 1702:04838, 2017.

(4.11) and (4.8),

$$\begin{aligned} f(R,Q',x_1) &:= |R-Q'| + RQ'y_f(x_1), \\ g(S,Q,x_2) &:= |S-Q| - 1 + SQy_g(x_2); \end{aligned} \tag{4.16}$$

hence,

$$\begin{aligned} Q_{n+1} &= (1-R)(1-Q'_n), \\ Q'_{n+1} &= (1-S)(1-Q_n). \end{aligned} \tag{4.17}$$

It should be noted that (4.16) must be used in conjunction with (4.9).

As we shall show in Chapter 6 the deterministic models don't capture the decaying oscillatory behavior at the clock edges. This necessitates a model that incorporates the nontrivial behavior observed at clock edges in the experiments.

4.2.3 Derivation of a Stochastic Set/Reset Flip-flop Model

As we shall observe in Chapter 6 the deterministic models don't capture the decaying oscillatory behavior at the clock edges. Physically, the oscillations observed at certain clock edges are caused by a non-binary difference in the capacitor voltage and threshold voltage (recall that the outputs are calculated by subtracting the threshold voltage from the capacitor voltage). However, we take a different approach, developing a model for the threshold voltages and output voltages rather than determining the output voltages via the other two as explained in the preceding section. In order to accomplish this, we must still rely on the physical intuition of the thresholding mechanism.

Whenever the inputs are such that they cause a threshold to change its state drastically (not including the gradual transition to chaos), the TCU attempts to synchronize the capacitor voltage with the threshold voltage for the proper output. This causes a competition between the capacitor voltage (under the influence of the previous input) and the TCU (stimulated by the current input), which the TCU finally wins. During this process, due to the chaotic nature of both the capacitor voltages and threshold voltages, each path to synchronization is different. Since we do not have the explicit model for the capacitor voltages, we will treat this competition as a stochastic process.

During the transitions that lead to the edge effect, we assume there is a probability at each time step that the output will either accept the new inputs or be induced by the weighted average of inputs from previous time steps, where the weights are also determined randomly (or rather, pseudo-randomly). Here we define the time step as the reciprocal of the circuit frequency.

Consider the sequences $\{m\}_1^M$, $\{n\}_0^N$, and $\{t\}_0^T$, such that $T = N+1$ and $M = T$. Let N be the number of time steps in the past that affect future outcomes and T be

the number of time steps after the edge at which the output is affected (usually about 1 millisecond). Further, let $\left\{w_j^{(t)}, \ldots, w_j^{(t-n+1)}, w_j^{(t-n)}, w_j^{(t-n-1)}, \ldots, w_j^{(t-N)}\right\} \subseteq \{m\}_1^M$ be the weights applied, with the same probability, out of $\{m\}_1^M$, to the respective inputs, $I_j^{(t-n)}$ for $j = \{1, 2, 3, 4\}$. Let $p(t) \in \{0, 1\}$ be some random variable for each time t, with not necessarily identical distributions. In addition, let

$$A_j^{(t)} = \begin{cases} I_j^{(t)} & \text{if } p(t) = 0, \\ \left(\sum_{n=0}^{N} w_j^{(t-n)} I_j^{(t-n)}\right) \Big/ \sum_{n=0}^{N} w_j^{(t-n)} & \text{if } p(t) = 1; \end{cases} \tag{4.18}$$

be the perceived input. Then we substitute $A_j^{(t)}$ into (4.8) for the respective inputs,

$$\begin{aligned} U_1(t) &= \left(1 - A_1^{(t)}\right)\left(1 - A_2^{(t)}\right), \\ U_2(t) &= \left(1 - A_3^{(t)}\right)\left(1 - A_4^{(t)}\right); \end{aligned} \tag{4.19}$$

to model the effects at the transition points. It should be noted that besides the transition points, which last about a millisecond, the outputs behave as described by the continuous extensions. Finally, in order to simulate noise produced by the waveform generator, we add/subtract a small random term, $\varepsilon \in \mathbb{R}$, to/from the inputs (i.e., $I_j \to I_j \pm \varepsilon$).

For the RSFF, we use the same technique, except this time we substitute (4.18) in only for R and S. Hence, for the transitions, (4.17) becomes,

$$\begin{aligned} Q_{n+1}(t) &= \left(1 - A_1^{(t)}\right)\left(1 - Q'_n\right), \\ Q'_{n+1}(t) &= \left(1 - A_3^{(t)}\right)\left(1 - Q_n\right). \end{aligned} \tag{4.20}$$

The models developed in this section will be analyzed and compared against experiments in Chapter 6.

CHAPTER 5

ANALYSIS AND SIMULATIONS: NAÏVE THRESHOLD CONTROL UNIT MODELS

In this chapter, we analyze the naïve RSFF model in detail. First, some of the more basic properties and fixed/periodic points of the minimal model are delineated (Section 5.1). Then we explore the effects of various perturbations of the minimal model (Section 5.2). Theorems on various paths to chaos are proved in order to demonstrate the richness of the problem and possible electrical design options (Section 5.3). While the types of perturbations mentioned are not necessarily physical, they are consistent perturbations occurring naturally in mathematical models and serves as a good mathematical exercise that may lead to more physically relevant ideas. Much of this work is presented in [136].

5.1 Dynamics of the Minimal Model

We shall analyze the deeper dynamical aspects of the model map (4.3) and (4.4) for various parameter ranges in the sequel, but first we dispose of some of the more elementary properties that follow directly from the definition and (A1)-(A6) shown in Section 4.1.2.

(D1) If we restrict F to $\hat{X} := \{(x, y) : 0 < x, y \text{ and } x + y < 1\}$, and denote this restriction by $\hat{F}$, it determines a full dynamical system defined as

$$\left\{\hat{F}^n : n \in \mathbb{Z}\right\},$$

which, for example, allows the definition of the full *orbit* of a point $p \in \mathring{Y}$ as

$$O(p) := \left\{ \hat{F}^n(p) : n \in \mathbb{Z} \right\}.$$

(D2) The line $y = x$ is F-invariant, while the x- and y-axes are F^2-invariant.

(D3) Both of the points $(1, 0)$ and $(0, 1)$ are fixed points of F^2.

5.1.1 Analysis of the Fixed and Periodic Points

The properties of the fixed and periodic points of the model map [136] shall be delineated in a series of lemmas, which follow directly from the results in the preceding sections and fundamental dynamical systems theory (as in [52, 75, 122, 164]). Our first result is the following,

Lemma 5.1.1. *The only fixed point of F in X is*

$$p_* = (x_*, y_*) = \left(\frac{3 - \sqrt{5}}{2} \right) (1, 1) \cong 0.38197\,(1, 1)\,,$$

which is a saddle point with eigenvalues

$$\lambda_s = -\left(\frac{3 - \sqrt{5}}{2} \right),\ \lambda_u = -\left(\frac{1 + \sqrt{5}}{2} \right).$$

This fixed point has linear stable and stable manifolds given as

$$W^s_{lin}\,(p_*) = \{(x, x) : x \in \mathbb{R}\} \text{ and } W^s\,(p_*) = \{(x, x) : 0 < x < 1\},$$

and the linear unstable manifold

$$W^u_{lin}\,(p_*) = \{(x, -x + 2x_*) : x \in \mathbb{R}\}.$$

Next, we analyze the unstable manifold of p_* in some detail. For this purpose, it is convenient to introduce a change of variables linked to the symmetry of F expressed in (A2); namely,

$$T(x,y) = (u,v) := \left(\frac{x+y-2x_*}{\sqrt{2}}, \frac{-x+y}{\sqrt{2}} \right),$$

with inverse

$$T^{-1}(u,v) = (x,y) := \left(x_* + \frac{u-v}{\sqrt{2}}, x_* + \frac{u+v}{\sqrt{2}} \right).$$

Clearly, T is a translation of the origin to the fixed point p_* followed by a counterclockwise rotation of $\pi/4$. The defining map for the dynamics in the new coordinates can be readily computed to be

$$\tilde{F}(u,v) := T \circ F \circ T^{-1}(u,v) = \left(\sqrt{2}/R(u,v) \right) \left(\sqrt{2}(1+2x_*^2)u + (1-x_*^2)(v^2-u^2), -\sqrt{2}v \right), \tag{5.1}$$

where

$$R(u,v) := 2x_*(2-x_*) + 2\sqrt{2}(1-x_*)u + v^2 - u^2.$$

The properties of the unstable manifold of the fixed point may now be described as in the following result, which can be proved directly from Lemma 5.1.1 and (5.1).

Lemma 5.1.2. *The unstable manifold of the fixed point p_*, which corresponds to $0 = (0,0)$ in the new $u-v$-coordinates, has the form*

$$W^u(p_*) = W^u(0) = \{(\varphi(v), v) : |v| < 1/\sqrt{2}\},$$

where φ is a smooth (C^∞) function satisfying the following properties:

(i) $\varphi(0) = \varphi'(0) = 0$ *and* $\varphi(v) \uparrow \frac{-2+\sqrt{5}}{\sqrt{2}}$ *as* $v \uparrow 1/\sqrt{2}$.

(ii) φ *is an even function.*

(iii) φ *satisfies the functional equation*

$$\varphi(v) = \kappa \left\{ (1 - x_*^2) \left(\varphi(v)^2 - v^2 \right) + \frac{S(\varphi(v), v)}{\sqrt{2}} \varphi \left(\frac{-2v}{S(\varphi(v), v)} \right) \right\}, \tag{5.2}$$

where $\kappa := 1/\left[\sqrt{2}\,(1 + 2x_*^2)\right]$ *and*

$$S(\varphi(v), v) := 2x_*(2 - x_*) + 2\sqrt{2}(1 - x_*)\varphi(v) + v^2 - \varphi(v)^2.$$

We note here that (5.2) can be used to obtain Picard iterate (local) approximations of the unique solution via the recursive formula (*cf.* [62])

$$\varphi_{n+1}(v) = \kappa \left\{ (1 - x_*^2) \left(\varphi_n(v)^2 - v^2 \right) + \frac{S(\varphi_n(v), v)}{\sqrt{2}} \varphi_n \left(\frac{-2v}{S(\varphi_n(v), v)} \right) \right\}. \tag{5.3}$$

A good starting point for these iterates is

$$\varphi_1(v) := \sqrt{2} \left(\sqrt{5} - 2 \right) v^2,$$

which satisfies the first two properties of Lemma 5.1.2, and turns out to be a fairly good approximation for the unstable manifold. Using (5.3), we obtain an improved approximation in the form

$$\varphi_2(u) = \kappa \left\{ (1 - x_*^2) \left(2(\sqrt{5} - 2)v^2 - 1 \right) v^2 + \left(\sqrt{5} - 2 \right) S(\varphi_1(v), v) \left(\frac{-2v}{S(\varphi_1(v), v)} \right)^2 \right\}, \tag{5.4}$$

where

$$S\left(\varphi_1(v), v\right) = 2 \left\{ x_* \left(1 - x_*\right) + v^2 \left[\left(2(1 - x_*)(\sqrt{5} - 2) + 1 \right) - (\sqrt{5} - 2)^2 v^2 \right] \right\}.$$

which is illustrated in Figure 5.1. As a matter of fact, it can be proved that these iterates actually converge locally to the smooth solution of (5.2), but the details,

which follow the argument in [62], although straightforward, are a bit too involved to include here. We remark here that it is not difficult to prove that a global solution of the unstable manifold equation can be obtained as follows:

$$W^u(p_*) = \lim_{n\to\infty} F^n(\Delta'),$$

where $\Delta' := \{(x, 1-x) : 0 \leq x \leq 1$.

Let us now investigate periodic orbits of the discrete dynamical system (4.3). It is easy to see from the definition that $\zeta := \{(1,0),(0,1)\}$ is a 2-cycle in which each point has (least) period two. As for any other cyclic behavior, we have the following comprehensive result that follows directly from the definition of the dynamical system and properties (A1)-(A6) (Section 4.1.2) and (D1)-(D3).

Lemma 5.1.3. *The 2-cycle $\zeta := \{(1,0),(0,1)\}$ is the only cycle of F; it is superstable and has basin of attraction*

$$\mathfrak{B}(\zeta) := I^2 \setminus \{(x,x) : x \in \mathbb{R}\}.$$

5.1.2 Summary of the Dynamics

We see from our analysis that the dynamical system (generated by) F defined by (4.3)-(4.4) has highly oscillatory, but quite regular behavior. There is one fixed point (on the line $y = x$), which attracts everything on the diagonal in X. In addition, there are only two other special points; namely, $(1,0)$ and $(0,1)$, both of which are superstable periodic points of period two that comprise the 2-cycle $\zeta := \{(1,0),(0,1)\}$. Moreover, ζ attracts everything in X except the points along the diagonal. Thus we see that our minimal model replicates the highly oscillatory "race" behavior found in physical realizations of RSFF circuits, but none of the chaotic dynamics. In fact, the

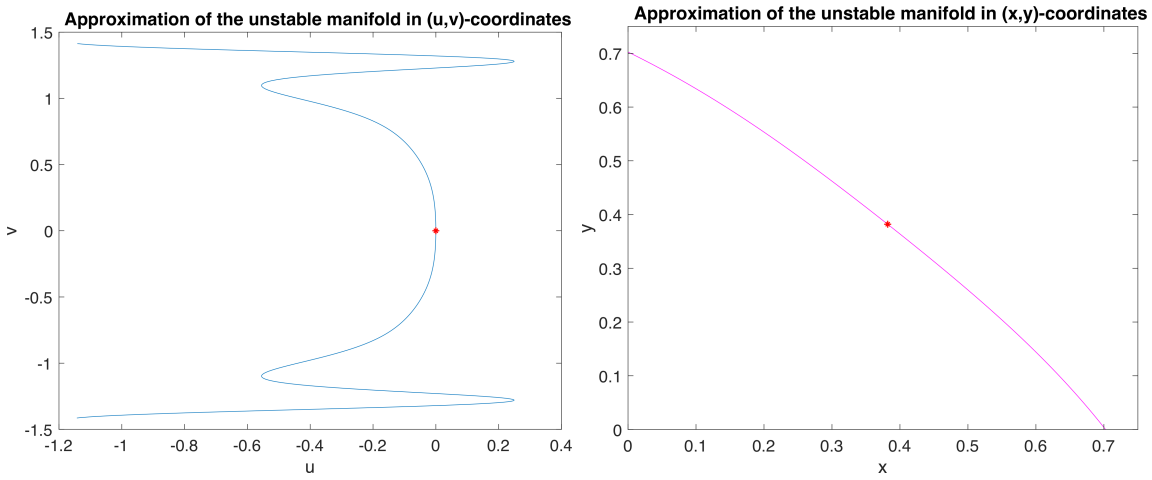

Figure 5.1 Picard iteration approximation (φ_6) in u, v-coordinates (left) and x, y-coordinates (right).

Source: A. Rahman and D. Blackmore. Threshold voltage dynamics of chaotic RS flip-flop circuits. arXiv:1507.03065, 2017.

nonwandering set of the minimal dynamical system, which actually coincides with the periodic set, has the simple form

$$\Omega(F) = \mathrm{Per}(F) = \{p_*\} \cup \zeta, \tag{5.5}$$

and F is C^1-structurally stable so that the dynamics maintains its regularity for all perturbations that, along with their derivatives, are sufficiently small. A proof of the structural stability for our map, which does not quite satisfy the usual hypotheses, can be fashioned from a straightforward modification of the methods employed in [36, 122, 125, 139]. Thus, it would seem that perturbations capable of generating chaos can be very small, but their derivatives need to be quite large or even fail to exist. We shall verify this in the sequel.

5.2 Perturbed Minimal Model with One-dimensional Chaos

In this section, we shall show how small perturbations that do not break the reflectional symmetry of the minimal model can produce chaos along the diagonal. More precisely, we shall give a constructive proof of the following result.

Theorem 5.2.1. *There exist continuous arbitrarily small C^0 perturbations of the minimal model map F for the RSFF circuit that are symmetric with respect to reflections in the invariant line $y = x$ and exhibit one-dimensional chaos in their restrictions to the diagonal.*

Proof. The idea of our argument is to embed an arbitrarily small C^0 perturbation into F that implants known chaotic dynamics along the dynamics without breaking the symmetry. This chaotic insert is defined along the diagonal for any $\sigma > 0$ using the continuous piecewise-linear function

$$\psi_\sigma(x) := \begin{cases} -x, & -2\sigma \le x \le 0 \\ -2\left(\sigma - |x - \sigma|\right), & 0 \le x \le 2\sigma \end{cases}, \tag{5.6}$$

which is illustrated in Figure 5.2. Observe that the composition $\tau_\sigma := \psi_\sigma^2 : [0, 2\sigma] \to [0, 2\sigma]$ is just the 2σ-scaled tent map given by

$$\tau_\sigma(x) = 2\left(\sigma - |x - \sigma|\right),$$

which is known to have chaotic dynamics, including periodic orbits of all periods, a dense orbit and a Lyapunov exponent of $\log 2$ for almost all initial points (see, e.g., [75]). Now we note from the definitions, (4.3) and (4.4), (A2), and Lemma 5.1.1 that the restriction f of F to the diagonal is

$$f(x) = \frac{1 - x}{2 - x}, \tag{5.7}$$

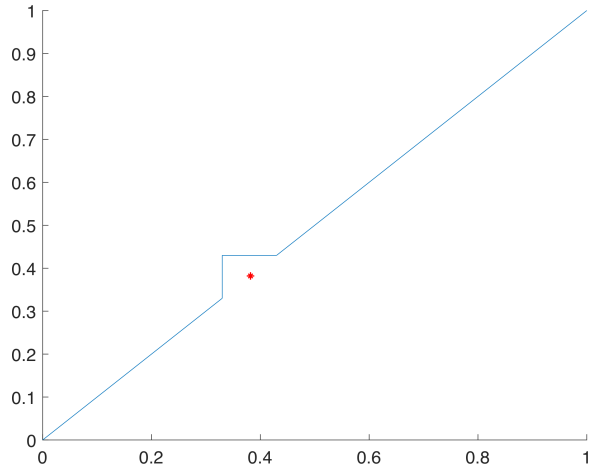

Figure 5.2 Illustration of a kink perturbation.

Source: A. Rahman and D. Blackmore. Threshold voltage dynamics of chaotic RS flip-flop circuits. arXiv:1507.03065, 2017.

which has the unique (stable) fixed point $x_* = (1/2)(3 - \sqrt{5})$, and this is a global attractor on the unit interval $[0, 1]$. It is easy to see that for every $\varepsilon > 0$, we can choose $0 < 8\sigma < \min\{1/6, \varepsilon\}$ such that there is a continuous map $f_\sigma : [0, 1] \to [0, 1/2]$ with the following properties: (i) $f_\sigma(x) = \psi_\sigma(x - x_*)$ for all $x \in J_\sigma := [x_* - 2\sigma, x_* + 2\sigma]$; (ii) $f_\sigma(x) = f(x)$ for all $x \in [0, 1] \setminus [x_* - 8\sigma, x_* + 4\sigma]$; (iii) f_σ is strictly decreasing on $[0, x_* + \sigma] \cup [x_* + 2\sigma, 1]$; and (iv) $|f_\sigma(x) - f(x)| < 4\sigma$ for all $0 \leq x \leq 1$. We observe that J_σ is a global attractor for f_σ, but not strange since it has dimension equal one. The one-dimensional chaotic implant can be extended to the whole two-dimensional domain of F. More precisely, it is easy to see (by simply linearly joining the perturbed diagonal map to F) that there exists for any $0 < 8\sigma < \min\{1/6, \varepsilon\}$ a continuous map $F_\sigma : X \to X$ satisfying the following properties: (a) the diagonal is F_σ- invariant (b) F_σ restricted to the diagonal is f_σ; (c) F_σ is symmetric with respect to the diagonal; (d) the dynamics of F_σ of the diagonal are qualitatively the same as that of F; and

(e) $|F_\sigma(x,y) - F(x,y)| < 8\sigma$ for all $(x,y) \in X$. As σ can be made arbitrarily small, the proof is complete. □

Observe that the perturbation F_σ constructed in the above proof is merely continuous and piecewise smooth inside a small ball centered at the fixed point x_* and smooth (i.e., C^∞) outside of the ball. The perturbation and its chaotic dynamics are illustrated in Figure 5.8. By smoothing the corners of the construction, the perturbation can be made smooth, which leads directly to the following result.

Corollary 5.2.1. *The perturbation in Theorem 5.2.1 can be chosen so that it is a C^∞ function having the same qualitative dynamics as the function constructed above.*

It is useful to note that the perturbation F_σ producing one-dimensional chaos along the invariant diagonal is arbitrarily C^0 close to the original map F. However, it cannot be made arbitrarily C^1 close to F by virtue of the readily verified fact that the restriction to the diagonal is C^1-structurally stable, so we cannot find arbitrarily small perturbations in the C^1 sense that posses chaotic dynamics. As we shall see in the next section, there exist arbitrarily small C^0 perturbations that are arbitrarily small C^1 perturbations except in regions of small diameter of F that are C^∞ and exhibit (two-dimensional) chaotic dynamical regimes.

5.3 Two-dimensional Chaos Induced by Perturbation

In this section, we shall show how arbitrarily small perturbations of the minimal model can induce chaotic dynamics of various types that are more substantial and complex than that described in Theorem 5.2.1. Our first perturbation involves the (geometric) local embedding of a Smale horseshoe in the minimal model in a neighborhood of the saddle point p_*.

5.3.1 Direct Horseshoe Chaos

We begin by defining a map in a neighborhood of p_* that yields the desired horseshoe. First, let $0 < \delta_0 \leq 0.04$ so that

$$\begin{aligned}\bar{B}_{6\sqrt{2}\delta_0}(p_*) :=& \{(x,y) \in \mathbb{R}^2 : (x-x_*)^2 + (y-y_*)^2 \leq 72\delta_0^2\} \\ &\subset [x_* - 6\sqrt{2}\delta_0, x_* + 6\sqrt{2}\delta_0]^2 \subset (0,1)^2 = \text{int}\left(I^2\right),\end{aligned}$$

where $\text{int}(E)$ denotes the interior of the subset E of the plane. Now, for each $0 < \delta \leq \delta_0$,we introduce a (s,t)-coordinate system with origin at p_*, the s-axis pointing to the right along the linear unstable manifold of p_* and the t-axis pointing upward along the stable manifold of p_*. Let $P_\delta : \{(s,t) : |s|, |t| \leq 6\delta\} \to \mathbb{R}^2$ be defined in terms of s,t-coordinates as

$$P_\delta(s,t) := (\varphi_\delta(s), \psi_\delta(s,t)), \tag{5.8}$$

where φ_δ is an odd function such that

$$\varphi_\delta(s) := \begin{cases} -(3/2)s, & 0 \leq s \leq 2\delta \\ 3(s-3\delta), & 2\delta \leq s \leq 4\delta \\ (1/3)(s+5\delta), & 4\delta \leq s \leq 6\delta \end{cases},$$

and ψ_δ is an odd function of t for each s given by

$$\psi_\delta(s,t) := -\delta t - \mu(s),$$

where

$$\mu(s) := \begin{cases} 0, & |s| \leq 2\delta \\ \text{sgn}(s)(|s| - \delta), & \delta \leq s \leq 2\delta \\ \text{sgn}(s)\delta, & |s| \geq 2\delta \end{cases}.$$

As p_* is a fixed point of both P_δ and the minimal model F, for and given $\varepsilon > 0$ we can choose $0 < \delta = \delta(\varepsilon) \leq \delta_0$ such that in terms of the euclidean norm, we have

$$\|F(p) - P_\delta(p)\| < \varepsilon$$

for all $p \in \bar{B}_{6\sqrt{2}\delta_0}(p_*)$. Moreover, it is easy to see – as shown in Figure 5.3 – that the image of the square

$$Q_\delta := \{(s,t) : -2\delta \leq s,t \leq 2\delta\}$$

under the map (5.6), namely $P_\delta(Q_\delta)$, is a (double) horseshoe. Note that all of the above functions are continuous and piecewise linear, which means they have smooth approximations (obtained by smoothly rounding out the corners) that are arbitrarily C^0-close to them. Consequently, we can and will assume that the perturbations chosen here to prove our next result and in the sequel are smooth.

Theorem 5.3.1. *For every $\varepsilon > 0$ there exists a $0 < \delta = \delta(\varepsilon) \leq 0.04$ such that the (smooth) perturbation of the minimal model map F defined as*

$$F_\delta(p) := (1 - \rho(r))\, P_\delta(p) + \rho(r) F(p), \tag{5.9}$$

where P_δ is as in (5.8), $r := \|p - p_*\|$ and

$$\rho(r) := \begin{cases} 0, & 0 \leq r \leq 4\delta\sqrt{2} \\ \left(1/\delta\sqrt{2}\right)\left(r - 4\delta\sqrt{2}\right), & 4\delta\sqrt{2} \leq r \leq 5\delta\sqrt{2} \\ 1, & r \geq 5\delta\sqrt{2} \end{cases},$$

satisfies $\|F_\delta(p) - F(p)\| < \varepsilon$ for all $p \in I^2$ and $F_\delta(Q_\delta)$ is a double horseshoe as shown in Figure 5.3.

Proof. As noted above, the restriction $0 < \delta \leq 0.04$ guarantees that $\bar{B}_{6\sqrt{2}\delta}(p_*)$ is contained in the interior of I^2 and that by taking δ sufficiently small, we can further

ensure that $\|F(p) - P_\delta(p)\| < \varepsilon$ on $\bar{B}_{6\sqrt{2}\delta}(p_*)$. Hence, it follows from the definition of ρ and (5.9) that $\|F_\delta(p) - F(p)\| < \varepsilon$ on I^2. Finally, (5.9) implies that $F_\delta(Q_\delta) = P_\delta(Q_\delta)$, which is the double horseshoe illustrated in Figure 5.3, and this completes the proof. □

In light of Theorem 5.3.1, the next result on the existence of horseshoe type chaos follows directly from the results of Birkhoff, Moser, and Smale (*cf.* [52, 75, 108, 122, 139, 151, 164]).

Corollary 5.3.1. *The perturbation F_δ in Theorem 5.3.1 is chaotic on an invariant subset contained in the double horseshoe image described therein. In particular, F_δ restricted to this invariant set is conjugate to the shift map on three symbols.*

5.3.2 Snap-back Repeller Chaos

There also are arbitrarily small C^0 perturbations of F exhibiting snap-back repeller chaos of the type described, for example, by Marotto [96, 97]. We start by showing how a small C^0 perturbation of F can turn p_* into a source with at least four snap-back points and then show that it is possible to create infinitely many snap-back points circling the fixed point. Once again we employ the s,t-coordinate system and δ_0 used in the preceding subsection to define the perturbation in a neighborhood of p_*. In particular, we define $R_\delta : \{(s,t) : |s|, |t| \leq 6\delta\} \to \mathbb{R}^2$ as

$$R_\delta(s,t) := (\varphi_\delta(s), \psi_\delta(t)), \tag{5.10}$$

where φ_δ is an odd function of s defined for $s \geq 0$ as

$$\varphi_\delta(s) := -2s,$$

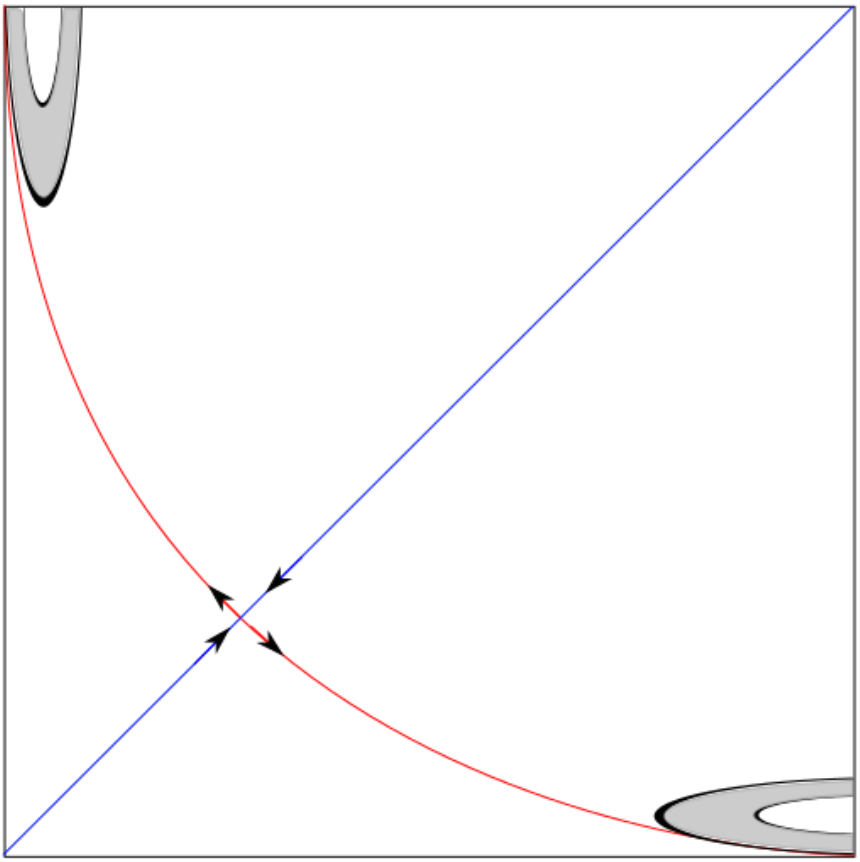

Figure 5.3 Embedded double horseshoe in the neighborhood of $(x, y) = (0, 1), (1, 0)$.

Source: A. Rahman and D. Blackmore. Threshold voltage dynamics of chaotic RS flip-flop circuits. arXiv:1507.03065, 2017.

and ψ_δ is an odd function of t defined for $t \geq 0$ by

$$\psi_\delta(t) := \begin{cases} -2t, & 0 \leq t \leq \delta \\ 2(t-2\delta), & \delta \leq t \leq 3\delta \\ 5\delta - t, & 3\delta \leq t \leq 6\delta \end{cases},$$

and graphed in Figure 5.4.

As p_* is a fixed point of both R_δ and the minimal model F, for and given $\varepsilon > 0$ we can choose $0 < \delta = \delta(\varepsilon) \leq \delta_0$ such that in terms of the euclidean norm, we have

$$\|F(p) - R_\delta(p)\| < \varepsilon$$

for all $p \in \bar{B}_{6\sqrt{2}\delta_0}(p_*)$. As above, we are going to assume with no loss of generality, that our perturbations are actually smooth, and this leads to our next result, which is an analog of Theorem 5.3.1.

Theorem 5.3.2. *For every $\varepsilon > 0$ there exists a $0 < \delta = \delta(\varepsilon) \leq 0.04$ such that the (smooth) perturbation of the minimal model map F defined as*

$$F_\delta(p) := (1 - \sigma(r))\, R_\delta(p) + \sigma(r) F(p), \tag{5.11}$$

where R_δ is as in (5.10), $r := \|p - p_*\|$ and

$$\sigma(r) := \begin{cases} 0, & 0 \leq r \leq 5\delta\sqrt{2} \\ \left(1/\delta\sqrt{2}\right)\left(r - 5\delta\sqrt{2}\right), & 5\delta\sqrt{2} \leq r \leq 6\delta\sqrt{2} \\ 1, & r \geq 6\delta\sqrt{2} \end{cases},$$

satisfies $\|F_\delta(p) - F(p)\| < \varepsilon$ for all $p \in I^2$ and p_* is a snap-back repeller for F_δ having the chaotic dynamics described in [96, 97].

Proof. The restriction $0 < \delta \leq 0.04$ ensures that $\bar{B}_{6\sqrt{2}\delta}(p_*)$ is contained in the interior of I^2 and that by taking δ sufficiently small, we can further ensure that

$\|F(p) - R_\delta(p)\| < \varepsilon$ on $\bar{B}_{6\sqrt{2}\delta}(p_*)$. Consequently, (5.11) and the definition of the function σ implies that $\|F_\delta(p) - F(p)\| < \varepsilon$ on I^2. It also follows from (5.11) that $F_\delta(p) = R_\delta(p)$ for all $p \in \bar{B}_{5\sqrt{2}\delta_0}(p_*)$, so p_* is a hyperbolic repeller for F_δ having - as is clear from Figure 5.4 – four snap-back points at $(s,t) = (0, \pm 2\delta)$ and $(s,t) = (0, \pm 5\delta)$. The chaotic dynamics then follows from [96, 97] and the proof is complete. □

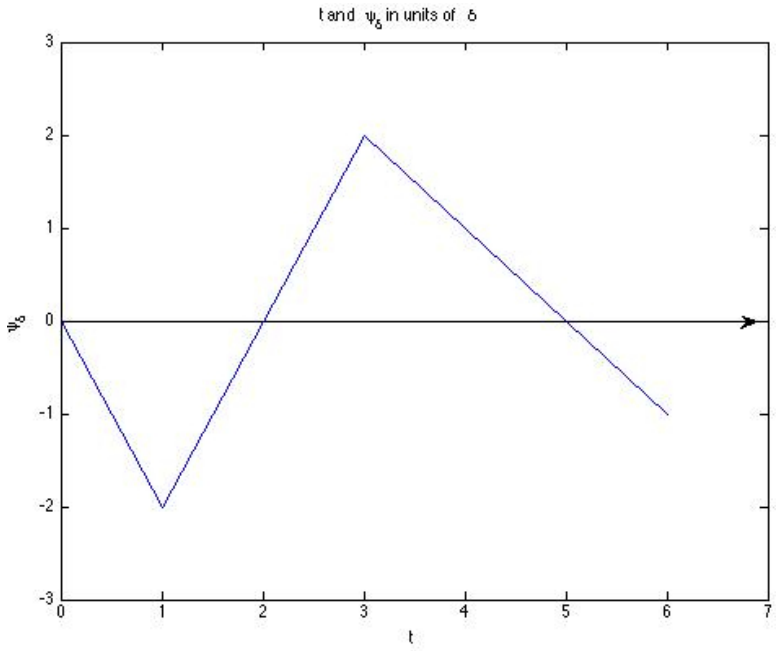

Figure 5.4 Coordinate function for snap-back repeller perturbation.

Source: A. Rahman and D. Blackmore. Threshold voltage dynamics of chaotic RS flip-flop circuits. arXiv:1507.03065, 2017.

It should be noted that the chaos described in Theorem 5.3.2 is essentially one-dimensional inasmuch as it is confined to the unstable manifold of p_* with respect to the minimal model F. However, it is not difficult to see how the construction in the above proof can be modified to obtain higher dimensional snap-back repeller chaos.

One need only consider a perturbation $\tilde{R}_\delta$ given in polar form (with p_* as the origin in the s,t- coordinate plane) as

$$\tilde{R}_\delta := \psi_\delta(r)\,(\cos\theta, \sin\theta)\,,$$

which has two full circles of snap-back points around p_*. If in addition, we modify ψ_δ in the annulus $2\delta \leq r \leq 6\delta$ so that it is negative for certain θ-sectors, the location of the snap-back points near p_* can be easily controlled.

5.3.3 Chaos Generated by Embedding Transverse Homoclinic Orbits and Heteroclinic 2-cycles

Chaos can also be generated by perturbing F so that it has transverse homoclinic points or transverse heteroclinic 2-cycle points, for then it exhibits chaotic subshift dynamics (*cf.*[6, 37, 52, 75, 122, 164]).

To begin, we prove a simple result showing how to create transverse intersections in a homoclinic or heteroclinic curve on a surface with an arbitrarily small C^0 perturbation. It should be noted that it is well known that such transverse intersections can be produced by arbitrarily small C^1 perturbations on general C^1 surfaces (*cf.* [75, 122, 164]), but we shall find it useful for our simulations in the sequel to present a specialized C^0 result for the plane that is much easier to prove. In fact, the idea of the proof is quite transparent, involving just a carefully localized small sinusoidal perturbation normal to the homoclinic or heteroclinic curve (see Figure 5.5), but the details are a bit involved. By a *homoclinic curve* or *heteroclinic curve* joining a single, respectively, pair of distinct saddle points of a differentiable map of a differentiable surface, we mean an (open) curve contained in the stable (unstable) and (stable) manifolds of the single, respectively, pair of points that contains the saddle points in

its closure. A *heteroclinic 2-cycle* is just pair of heteroclinic curves joining a pair of distinct saddle points.

Lemma 5.3.1. *Let $f : S \to S$ be a C^1 self-map of a connected surface S in $\mathbb{R}^2$. Suppose that p and q are identical or distinct saddle points of f joined, respectively, by a homoclinic or heteroclinic curve γ that is contained both in $W^u(p) \cap W^s(q)$ and a subset of S that is compact in $\mathbb{R}^2$. If there is a point $u_{-1} \in \gamma$ such that $u_0 := f(u_{-1})$, $u_1 := f^2(u_{-1})$, $u_2 := f^3(u_{-1})$ and $u_3 := f^4(u_{-1})$ are contained in a connected open neighborhood U of the closed subarc κ of γ from u_{-1} to u_3 and f is invertible on U, then there is an arbitrarily small C^0 perturbation g of f, equal to f except in an open subset V of U that contains a nontrivial closed subarc σ of κ from u_0 to a point $v_0 \in \gamma$ not containing u_1, such that $W^u_g(p)$ has a transverse intersection with $W^s_g(q)$ in $f(\sigma)$.*

Proof. First, we orient the curve γ from p to q so that it follows the direction of positive iterates. Next, define the (oriented) arclength along γ starting from u_0 to be s, so that $s(u_0) = 0 < s(u_1) < s(u_2)$ owing to the definition of γ and the hypotheses. It follows from our assumptions that there exists a point $\tilde{u} \in \kappa$ with $0 < s(\tilde{u}) < s(u_1)$ such that the closed subarc χ of γ from u_0 to $\tilde{u}$ satisfies the following property:

(P1) $f^{-1}(\chi)$, χ, $f(\chi)$ and $f^2(\chi)$ are pairwise disjoint closed subarcs of κ.

At each point $u \in \gamma$ there is a unit normal vector that is unique if we specify an orientation, which we do by defining the positive direction to be consistent with the right hand rule and the positive direction along the curve. We denote this vector by $\boldsymbol{n}(u)$, which now allows the definition of a positive and negative distance from γ points x sufficiently close to γ, which we denote by $\nu(x)$. We then combine this with a coordinate $s(x)$ defined to be $s(\varphi(x))$, where $\varphi(x) := u$ is the unique (for points sufficiently near γ) point on the curve such that the distance $d(x, \gamma)$ from the point

x to γ is equal to $\|x-u\|$, where $\|\cdot\|$ is the Euclidean norm. Then basic results on normal bundles such as in [79] imply that there exists $\lambda_0 > 0$ such that for every $0 < \lambda \leq \lambda_0$,

$$N_\lambda := \{x \in S : s(u_{-1}) - \lambda/2 < s(x) < s(u_3) + \lambda/2; |\nu(x)| < \lambda\} \tag{5.12}$$

is an open set contained in U and is a neighborhood of the closed subarc κ, N_λ does not contain p or q, and it is well defined in the sense that every $x \in N_\lambda$ is uniquely determined by its coordinates $(s(x), \nu(x))$. We now have all the tools necessary to provide a simple description of small C^0 perturbations that possess the desired transverse intersections of unstable and stable manifolds. In virtue of the differentiability of the map and the homoclinic or heteroclinic curve and the definition of N_λ, there exists $0 < \lambda_1 < \lambda_0$ such that if $0 < \lambda \leq \lambda_1$ and we define $\bar{N}_\lambda(\chi) := \{x \in S : 0 \leq s(x) \leq s(\tilde{u}); |\nu(x)| \leq \lambda\}$, then the following obtains:

(P2) $f^{-1}\left(\bar{N}_\lambda(\chi)\right)$, $\bar{N}_\lambda(\chi)$, $f\left(\bar{N}_\lambda(\chi)\right)$ and $f^2\left(\bar{N}_\lambda(\chi)\right)$ are pairwise disjoint closed subsets of N_{λ_0}.

Now for any $0 < \varepsilon < \lambda_1$, we define the perturbation increment function $\Delta_\varepsilon : S \to S$ as

$$\Delta_\varepsilon(x) := \begin{cases} \varepsilon\left(1 - \lambda^{-1}|\nu(x)|\right) \sin\left(\frac{2\pi s(x)}{s(\tilde{u})}\right) \boldsymbol{n}(\varphi(x)), & x \in \bar{N}_\lambda(\chi) \\ 0, & x \notin \bar{N}_\lambda(\chi) \end{cases}, \tag{5.13}$$

which is tantamount to saying that the s-coordinate function of Δ_ε is zero and ν-coordinate function is zero except in $\bar{N}_\lambda(\sigma)$ where it is defined to be the coefficient of the unit normal vector in (5.13). Note that this function also vanishes when $s(x) = 0$, $(1/2)s(\tilde{u})$ or $s(\tilde{u})$; that is, all along the normals to the curve γ at u_0, $\tilde{u}$ and a point $w \in \gamma$ with $s(\tilde{u}) < s(w) = (1/2)s(\tilde{u}) < s(\tilde{u})$. Moreover, the graph of (5.13)

in the s, ν-plane has a transverse intersection with the s-axis at $s = (1/2)s(\tilde{u})$. The desired perturbation of f is

$$g_\varepsilon = f + \Delta_\varepsilon, \tag{5.14}$$

which is readily seen to have the desired properties. In particular, $\|g_\varepsilon(x) - f(x)\| \leq \varepsilon$ for all $x \in S$, $W^u_{g_\varepsilon}(p) = W^u_f(p)$ and $W^s_{g_\varepsilon}(q) = W^s_f(q)$ in a neighborhood of p and q, respectively, and the differentiability of both f and g_ε in a neighborhood of w together with (P1), (P2) and the transversality property of Δ_ε at w guarantee that there is a transverse intersection of $W^u_{g_\varepsilon}(p)$ and $W^s_{g_\varepsilon}(q)$ at $f(w)$. Thus, the proof is complete. □

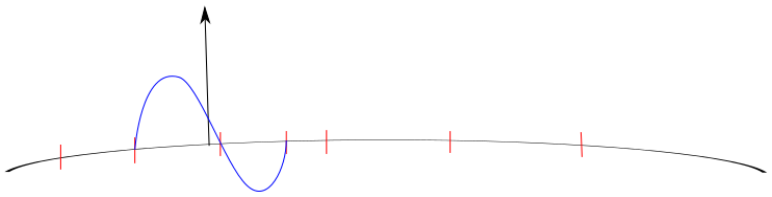

Figure 5.5 An example of a transverse intersection perturbation.

Source: A. Rahman and D. Blackmore. Threshold voltage dynamics of chaotic RS flip-flop circuits. arXiv:1507.03065, 2017.

As a final remark concerning the above lemma, it is rather easy to see how by smoothing corners and reducing the scale of the perturbation increment, if necessary, the perturbation of the function can be chosen to be C^1 small. Moreover, it is a simple matter to extend the result to general C^1 surfaces using standard techniques from differential geometry and topology (*cf.* [75, 79, 139, 122, 125, 164]).

Next we shall show how to embed C^0-small dynamics in a neighborhood of the fixed point p_* of the minimal model F that has a homoclinic orbit or a heteroclinic 2-cycle. Once done, we can apply Lemma 5.3.1 to create chaotic dynamics in arbitrarily

small C^0 perturbations of F. We shall use the time-one maps of the following Hamiltonian differential equations defined for $\delta > 0$ as

$$\begin{aligned} \dot{\xi} &= \eta \left(\delta^2 + \xi^2 + \eta^2\right), \\ \dot{\eta} &= \xi \left(\delta^2 - \xi^2 - \eta^2\right), \end{aligned} \tag{5.15}$$

which has the Hamiltonian function

$$H_\delta = (1/4)\left[\left(\xi^2 + \eta^2\right)^2 - 2\left(\xi^2 - \eta^2\right)\right]. \tag{5.16}$$

Here we have relabeled the s, t-coordinates used in subsections 5.1 and 5.2 as ξ, η-coordinates to avoid confusion with the time parameter t in (5.15). This equation yields a pair of homoclinic orbits corresponding to $H_\delta = 0$ that are depicted in Figure 5.6. For the heteroclinic 2-cycle, we choose the system

$$\begin{aligned} \dot{\xi} &= \eta, \\ \dot{\eta} &= -\xi + \left(\xi^3/\delta^2\right), \end{aligned} \tag{5.17}$$

with Hamiltonian function

$$K_\delta = (1/4)\left[2\left(\xi^2 + \eta^2\right) - \left(x^4/\delta^2\right)\right]. \tag{5.18}$$

This system has a heteroclinic 2-cycle contained in $K_\delta = \delta^2/4$, which is also shown in Figure 5.6. Now let the solution of (5.15) and (5.17) be denoted, respectively as

$$(\xi, \eta) = \varphi_\delta\left(t, (\xi_0, \eta_0)\right) \tag{5.19}$$

and

$$(\xi, \eta) = \psi_\delta\left(t, (\xi_0, \eta_0)\right). \tag{5.20}$$

The desired embeddings are obtained from the time-1 maps of the above; namely, we define

$$\Phi_\delta(\xi,\eta) := \varphi_\delta\left(1,(\xi,\eta)\right) \tag{5.21}$$

and

$$\Psi_\delta(\xi,\eta) := \psi_\delta\left(1,(\xi,\eta)\right). \tag{5.22}$$

Clearly, these maps have the desired homoclinic and heteroclinic orbits, respectively. Now, we select $\delta_0 > 0$ so small that $\bar{B}_{6\delta_0}(p_*)$ is contained in the interior of I^2 and then $0 < \delta = \delta(\varepsilon) \leq \delta_0$ for a given $\varepsilon > 0$ such that

$$\|F(z) - \Phi_\delta(z)\| < \varepsilon \tag{5.23}$$

and

$$\|F(z) - \Psi_\delta(z)\| < \varepsilon \tag{5.24}$$

for all $z \in \bar{B}_{6\delta_0}(p_*)$. Whence, we can define

$$\hat{F}_\delta(z) := (1 - \varkappa(r))\,\Phi_\delta(z) + \varkappa(r)F(z) \tag{5.25}$$

and

$$\tilde{F}_\delta(z) := (1 - \varkappa(r))\,\Psi_\delta(z) + \varkappa(r)F(z), \tag{5.26}$$

where $r := \|z - p_*\|$ and

$$\varkappa(r) := \begin{cases} 0, & 0 \leq r \leq 3\delta \\ (1/\delta)\,(r - 3\delta), & 3\delta \leq r \leq 4\delta \\ 1, & r \geq 4\delta \end{cases}. \tag{5.27}$$

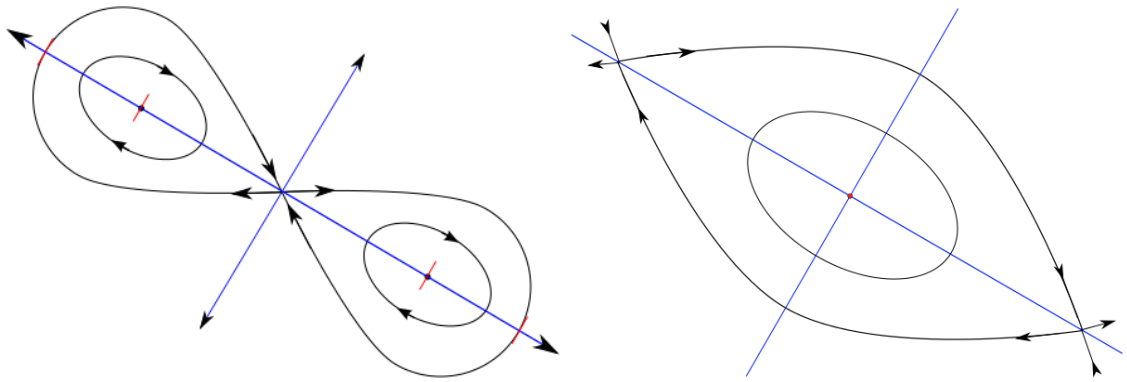

Figure 5.6 Sketches of homoclinic and heteroclinic orbits.

Source: A. Rahman and D. Blackmore. Threshold voltage dynamics of chaotic RS flip-flop circuits. arXiv:1507.03065, 2017.

It follows from (5.17)-(5.26) that $\left\|F(z) - \hat{F}_\delta(z)\right\| < \varepsilon$ and $\left\|F(z) - \tilde{F}_\delta(z)\right\| < \varepsilon$ for all $z \in I^2$ and that $\hat{F}_\delta$ has a homoclinic orbit comprised of the stable and unstable manifolds at p_* and $\tilde{F}_\delta$ has a heteroclinic 2-cycle centered at p_* as shown in Figure 5.6. Whence, we may, after choosing δ smaller if necessary, use Lemma 5.3.1 to further perturb $\hat{F}_\delta$ and $\tilde{F}_\delta$ to create a transverse intersection point in the homoclinic orbit and, respectively, to create a transverse intersection point in one or both components of the heteroclinic 2-cycle, while still remaining ε-close to the original maps in the C^0 metric. Then λ-Lemma based arguments of the type developed in such sources as [6, 37, 122, 164] and the smoothing discussed above lead directly to the following result.

Theorem 5.3.3. *For every $\varepsilon > 0$ there exist smooth C^0 ε-close perturbations of the minimal model map F exhibiting transverse homoclinic point or transverse heteroclinic 2-cycle induced chaos.*

5.3.4 Multihorseshoe Strange Attractor Perturbations

The next element of our description and analysis of more pervasive chaotic C^0 perturbations of the map F defined by (4.3)-(4.4) involves embedding a symmetric pair of attracting horseshoes along the lines introduced in [8]. In particular, we shall show how to C^0 perturb F to produce multihorseshoe (more precisely, double-horseshoe) chaos (*cf.* [8]), as shown in Figure 5.7.

To begin the construction of the embedding, we note first that the minimal map F is actually defined and smooth at all points in the x, y-plane above the curve defined by $x + y - xy = 0$. Next, for convenience, we denote the period-2 points $(1, 0)$ and $(0, 1)$ by p and q, respectively. Let $\varepsilon > 0$ be given. As both p and q are fixed points of F^2 and of G^2, where G is the reflection in the line $y = x$, we may choose $0 < \delta \leq 1/4$ such that

$$\|F(z) - G(z)\| < \varepsilon/2 \tag{5.28}$$

whenever $z \in \bar{B}_{10\sqrt{2}\delta}(p) \cup \bar{B}_{10\sqrt{2}\delta}(q)$. Define

$$\tilde{F}_\varepsilon(z) := \begin{cases} F(z), & z \notin \bar{B}_{10\sqrt{2}\delta}(p) \cup \bar{B}_{10\sqrt{2}\delta}(q) \\ (1 - \omega(r_p))\, G(z) + \omega(r_p) F(z), & z \in \bar{B}_{10\sqrt{2}\delta}(p) \\ (1 - \omega(r_q))\, G(z) + \omega(r_q) F(z), & z \in \bar{B}_{10\sqrt{2}\delta}(q) \end{cases}, \tag{5.29}$$

where $r_p := \|z - p\|$, $r_q := \|z - q\|$ and

$$\omega(r) := \begin{cases} 0, & 0 \leq r \leq 8\delta\sqrt{2} \\ \left(1/\delta\sqrt{2}\right)\left(r - 8\delta\sqrt{2}\right), & 8\delta\sqrt{2} \leq r \leq 9\delta\sqrt{2} \\ 1, & r \geq 9\delta\sqrt{2} \end{cases}. \tag{5.30}$$

It is clear from the definition and (5.28) that

$$\left\| F(z) - \tilde{F}_\varepsilon(z) \right\| < \varepsilon/2. \tag{5.31}$$

It now remains to make a final adjustment of the map $\tilde{F}_\varepsilon$ that has the attracting horseshoes. To this end, we define the following perturbation of the identity in $\bar{B}_{10\sqrt{2}\delta}(p) \cap I^2$ using the original x, y-coordinates

$$\Theta(x, y) = (\varphi(x), \psi(x, y)),$$

where

$$\varphi(x) := \begin{cases} 1, & x \leq 1 - 7\delta \text{ or } 1 - \delta \leq x \leq 1 \\ 2(x + \delta) - 1, & 1 - 4\delta \leq x \leq 1 - \delta \\ -2(x + 7\delta) + 3, & 1 - 7\delta \leq x \leq 1 - 4\delta \end{cases} \tag{5.32}$$

and

$$\psi(x, y) := \begin{cases} y/5, & x \leq 1 - 9\delta \text{ or } 1 - 5\delta \leq x \leq 1 \\ (y/5) + 6(1 - 5\delta - x), & 1 - 6\delta \leq x \leq 1 - 5\delta \\ (y/5) + 6\delta & 1 - 7\delta \leq x \leq 1 - 6\delta \\ (y/5) + 3(x + 9\delta - 1) & 1 - 9\delta \leq x \leq 1 - 7\delta \end{cases}. \tag{5.33}$$

Observe that Θ has a sink at p and a saddle point at $(1 - 2\delta, 0)$ with a horizontal unstable and vertical stable manifold. Moreover, Θ maps the rectangle $[1 - 4\delta, 1 - \delta] \times [-\delta, 9\delta]$ onto a piecewise smooth (and of course smoothable) attracting horseshoe as defined in [8]. This function can be reflected in the line $y = x$ to obtain the symmetric map $\hat{\Theta} := G \circ \Theta \circ G$ mapping the rectangle $[-\delta, 9\delta] \times [1 - 4\delta, 1 - \delta]$ onto the reflection of the horseshoe image of Θ in $y = x$.

Now it follows directly from the above definitions that, taking δ smaller if necessary, we can ensure that

$$\|G(z) - \Theta \circ G(z)\| < \varepsilon/2 \tag{5.34}$$

when $z \in \bar{B}_{10\sqrt{2}\delta}(q) \cap I^2$ and

$$\left\| G(z) - \hat{\Theta} \circ G(z) \right\| < \varepsilon/2 \tag{5.35}$$

for all $z \in \bar{B}_{10\sqrt{2}\delta}(p) \cap I^2$. Therefore, also taking into account (5.31), the modification F_ε of $\tilde{F}_\varepsilon$ defined as

$$F_\varepsilon(z) := \begin{cases} F(z), & z \notin \bar{B}_{10\sqrt{2}\delta}(p) \cup \bar{B}_{10\sqrt{2}\delta}(q) \\ (1-\omega(r_p))\,\hat{\Theta} \circ G(z) + \omega(r_p) F(z), & z \in \bar{B}_{10\sqrt{2}\delta}(p) \\ (1-\omega(r_q))\,\Theta \circ G(z) + \omega(r_q) F(z), & z \in \bar{B}_{10\sqrt{2}\delta}(q) \end{cases}$$

satisfies

$$\|F(z) - F_\varepsilon(z)\| < \varepsilon.$$

Moreover, we note that both p and q are attracting fixed points (sinks) of F_ε^2, just as they are of F^2, while $(1-2\delta, 0)$ and $(0, 1-2\delta)$ comprise a 2-cycle of F_ε (consisting of saddle points of F_ε^2) but not F. Finally, as constructed, each of the symmetric horseshoes shown in Figure 5.7 is an attracting horseshoe of F, so that it follows from the main multihorseshoe theorem in [8] that we have now proved the following result.

Theorem 5.3.4. *For every positive ε there is a smooth C^0 ε-close perturbation F_ε of the minimal map F having a strange chaotic double-horseshoe attractor with attracting horseshoes in neighborhoods of the points $(1,0)$ and $(0,1)$.*

It is interesting to note that the strange attractor for the small perturbation of F in Theorem 5.3.4 resembles a discrete analog of the "double scroll" attractor for Chua's circuit (*cf.* [23, 25]), also seen in the dynamics of RSFF realization simulations such as in [16] and could, with some minor modification, produce discrete analogs of the attractors found in or associated with various physical circuit models such as in [16, 74, 73, 84, 107, 111, 110, 118].

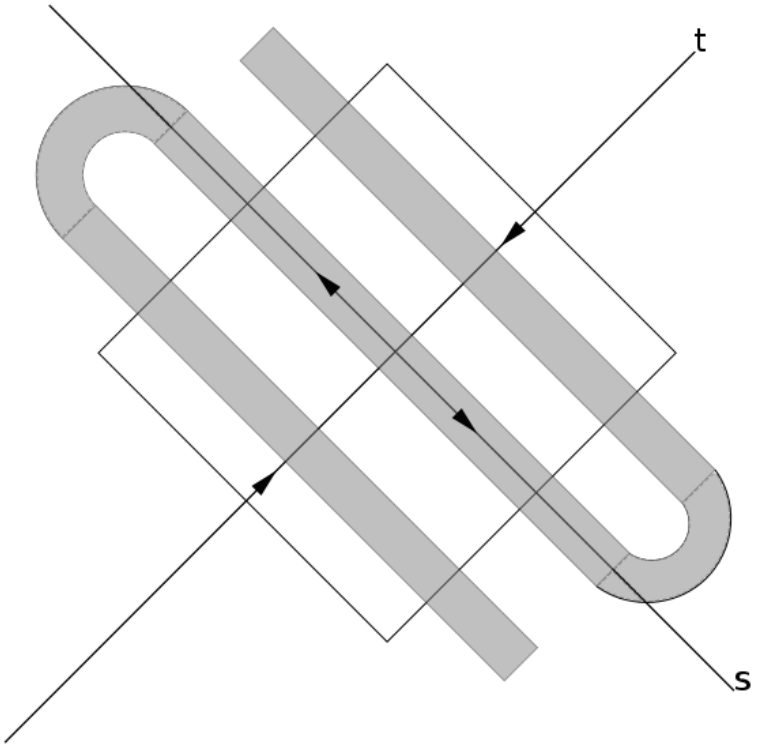

Figure 5.7 Embedded double-horseshoe chaotic strange attractor.

Source: A. Rahman and D. Blackmore. Threshold voltage dynamics of chaotic RS flip-flop circuits. arXiv:1507.03065, 2017.

5.3.5 Neimark–Sacker Bifurcation Perturbations

Our final result shall show that Neimark–Sacker bifurcations can occur in arbitrarily small C^0 perturbations of the minimal model map F. Once again, we use the ξ, η-coordinates employed in preceding subsections to define for $\delta > 0$ the following parameter-dependent map in polar coordinates in the ξ, η - plane with origin at p_*

$$N_\delta(\xi, \eta; \mu, \alpha) := -\delta \tanh(\mu r/\delta)\,(\cos(\theta + \alpha), \sin(\theta + \alpha)), \tag{5.36}$$

where $1/2 < \mu < 3/2$, α is nonnegative and $r := \|(\xi, \eta) - p_*\|$. It is easy to verify that the origin is a global attractor of (5.36) for $1/2 < \mu < 1$ and a local repeller for $1 < \mu < 3/2$, so $\mu = 1$ is a bifurcation value. Moreover, as μ increases across 1 with a corresponding transition of the origin from a sink to a source, a stable invariant circle of radius $r = r(\mu)$, where $r(\mu)$ is the unique positive solution of

$$\delta \tanh(\mu r/\delta) = r. \tag{5.37}$$

The parameter α just represents the rotation of the map (5.36), so what we have is a Neimark–Sacker bifurcation at $\mu = 1$.

Now just as in the preceding subsections, we can choose $\delta_0 > 0$ so small that $\bar{B}_{6\delta_0}(p_*)$ is contained in the interior of I^2 and then $0 < \delta = \delta(\varepsilon) \le \delta_0$ for a given $\varepsilon > 0$ such that

$$\|F(z) - N_\delta(z)\| < \varepsilon \tag{5.38}$$

for all $\mu \in (1/2, 3/2)$ and $\alpha \ge 0$ whenever $z \in \bar{B}_{6\delta_0}(p_*)$. Therefore, by defining

$$\check{F}_\delta(z) := (1 - \varkappa(r))\, N_\delta(z) + \varkappa(r) F(z),$$

where $\varkappa$ is defined just as in (5.27), we obtain a map that is ε-close to F in the C^0 norm and has the desired bifurcation properties. In short, we have now proved the following result.

Theorem 5.3.5. *For every positive ε there is a smooth C^0 ε-close perturbation $\check{F}$ of the minimal map F having a Niemark–Sacker bifurcation at p_*.*

A direct detailed construction was used for the proof of Theorem 5.3.5, but the same result can be proved, using the main theorem in [17], for any perturbation in which p_* changes from an attractor to a local repeller as a parameter is varied. It should also be noted that one can, by a straightforward modification of the above procedure, construct arbitrarily small C^0 perturbations of F exhibiting doubling Neimark–Sacker (Hopf) cascades like those in the ad hoc RSFF model analyzed in [9].

5.4 Simulations, Computations, and Comparisons

Our purpose in this section is to show with just a few examples that our discrete dynamical model – when properly perturbed – shares many properties with actual physical realizations (and their associated mathematical models) of the R-S flip-flop and related circuits such as in [34, 74, 73, 84, 107, 111, 110, 118, 142, 171]. For example, we have already demonstrated in Section 5.3 that our model can be perturbed so that it exhibits the chaos found by simulation in a one-dimensional map associated with the dynamics of the realization of the autonomous flip-flop circuit - which is not an R-S flip-flop circuit - investigated in [118], and it is this kind of chaos we consider in the next subsection.

5.4.1 Perturbed Minimal Model with One-dimensional Chaos

We derive the perturbed map by inserting (5.6) into (4.4) where $x \to \varphi_\sigma(x)$ and $y \to \varphi_\delta(y)$,

$$\begin{aligned} \xi(x,y) &:= \frac{\varphi_\delta(y)(1-\varphi_\sigma(x))}{1-(1-\varphi_\sigma(x))(1-\varphi_\delta(y))} \\ \eta(x,y) &:= \frac{\varphi_\sigma(x)(1-\varphi_\delta(y))}{1-(1-\varphi_\sigma(x))(1-\varphi_\delta(y))}. \end{aligned} \tag{5.39}$$

The iterates of the perturbed map are shown in Figure 5.8.

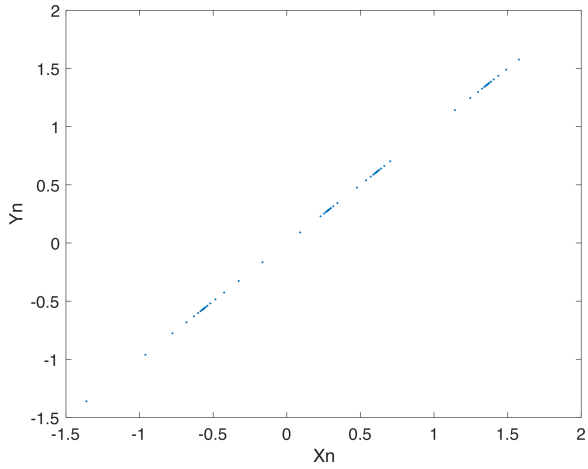

Figure 5.8 Example of perturbation inducing one-dimensional chaos on the line $y = x$.

Source: A. Rahman and D. Blackmore. Threshold voltage dynamics of chaotic RS flip-flop circuits. arXiv:1507.03065, 2017.

Corollary 5.4.1. *The perturbation in the preceding theorem can be chosen so that it is a C^∞ function having the same qualitative dynamics as the function constructed above.*

5.4.2 Evidence of Two-dimensional Chaos

As we have shown above, almost any type of chaotic dynamics - including double scroll chaos - can be obtained from the ideal map by inserting specific localized

perturbations. We shall now show that the introduction of a fairly general type of small C^0 perturbation is apt to produce chaotic dynamics. In order to produce two-dimensional chaos let us use the perturbation,

$$\begin{aligned}
\varphi_{k,\sigma}(x) &= 3.7\left[a_0 - .02 - \sum_{j=1}^{k} a_j \cos(j\pi x)\right] \\
a_{0,\sigma}(x) &= \frac{\mu_x + \lambda_x}{8} + \frac{\frac{1}{2}+\varepsilon}{4} \\
a_{j,\sigma}(x) &= \frac{1}{2j\pi}\left\{(1-\lambda_x)\sin\left[j\left(\frac{1}{2}-\varepsilon\right)\pi\right] + \frac{\mu_x+\lambda_x}{j\pi}[(-1)^j - 1]\right\}
\end{aligned}$$

to get the map,

$$\begin{aligned}
\xi &:= \frac{\varphi_{m,\delta}(y)(1-\varphi_{n,\varepsilon}(x))}{1-(1-\varphi_{m,\delta}(y))(1-\varphi_{n,\varepsilon}(x))} \\
\eta &:= \frac{\varphi_{n,\varepsilon}(x)(1-\varphi_{m,\delta}(y))}{1-(1-\varphi_{m,\delta}(y))(1-\varphi_{n,\varepsilon}(x))}
\end{aligned} \tag{5.40}$$

The iterates of this map, with their characteristic splattering indicative of chaos, are shown in Figure 5.9.

5.4.3 Ring Oscillator Example

Another interesting circuit, which we intend to analyze in detail in a forthcoming paper, is a modified ring oscillator. This ring oscillator comprises three NOR gates with feedbacks, in a very similar fashion to that of the RS flip-flop circuit. One may even choose to think of this as a three-dimensional RS flip-flop circuit.

We note that if the inputs are set to zero, the system is precisely a ring oscillator because the NOR gates now act as inverters. Applying our algorithm for finding a discrete dynamical system model for logical circuits yields the following "minimal"

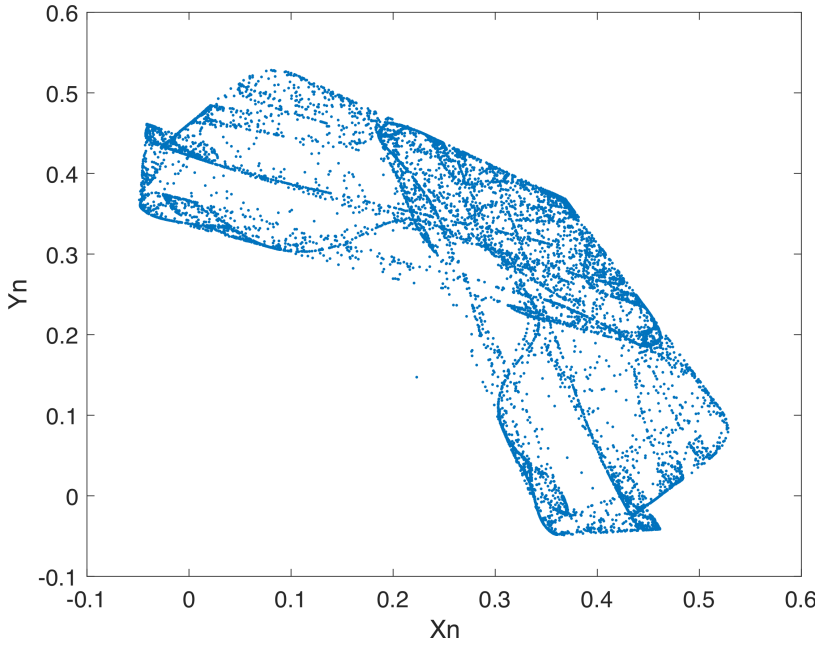

Figure 5.9 Iterates of a perturbed map seeming to exhibit two-dimensional chaos.

Source: A. Rahman and D. Blackmore. Threshold voltage dynamics of chaotic RS flip-flop circuits. arXiv:1507.03065, 2017.

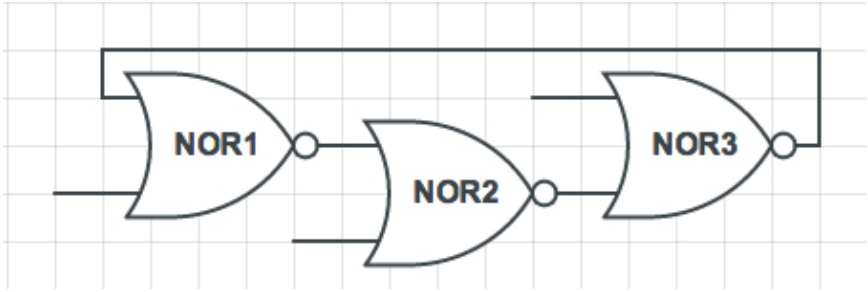

Figure 5.10 A "blox-box" schematic of a ring oscillator designed out of three NOR gates.

Source: A. Rahman and D. Blackmore. Threshold voltage dynamics of chaotic RS flip-flop circuits. arXiv:1507.03065, 2017.

(unperturbed) model,

$$\begin{aligned}\xi &= \frac{(x-1)(y(z-1)+1)}{(x-1(y-1)(z-1)-1)},\\ \eta &= \frac{(y-1)(z(x-1)+1)}{(x-1(y-1)(z-1)-1)},\\ \zeta &= \frac{(z-1)(x(y-1)+1)}{(x-1(y-1)(z-1)-1)};\end{aligned} \tag{5.41}$$

The only valid fixed point is $(x_*, y_*, z_*) = ((3-\sqrt{5})/2, (3-\sqrt{5})/2, (3-\sqrt{5})/2)$. Since the fixed points are roots of a quartic equation, one may wonder what happens to the other roots. We find that the other three roots are out of our domain, which means that they are of no practical consequence. For the ideal model, regardless of the initial conditions, the orbits decay to the fixed point in a spiral manner shown in Figure 5.11.

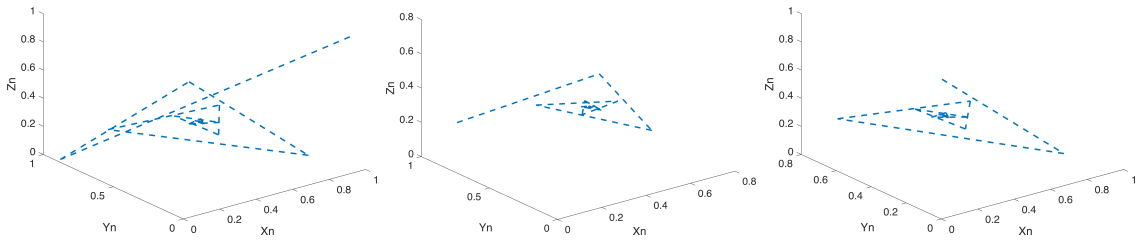

Figure 5.11 Plots of the orbits of (5.41) with initial conditions, $(.99, .1, .9)$, $(.1, .9, .2)$, and $(.1, .1, .9)$ respectively.

Source: A. Rahman and D. Blackmore. Threshold voltage dynamics of chaotic RS flip-flop circuits. arXiv:1507.03065, 2017.

In order to produce more interesting dynamics we perturb the ideal model slightly. Using a perturbation similar to (5.40), we produce the chaotic dynamics shown in Figure 5.12.

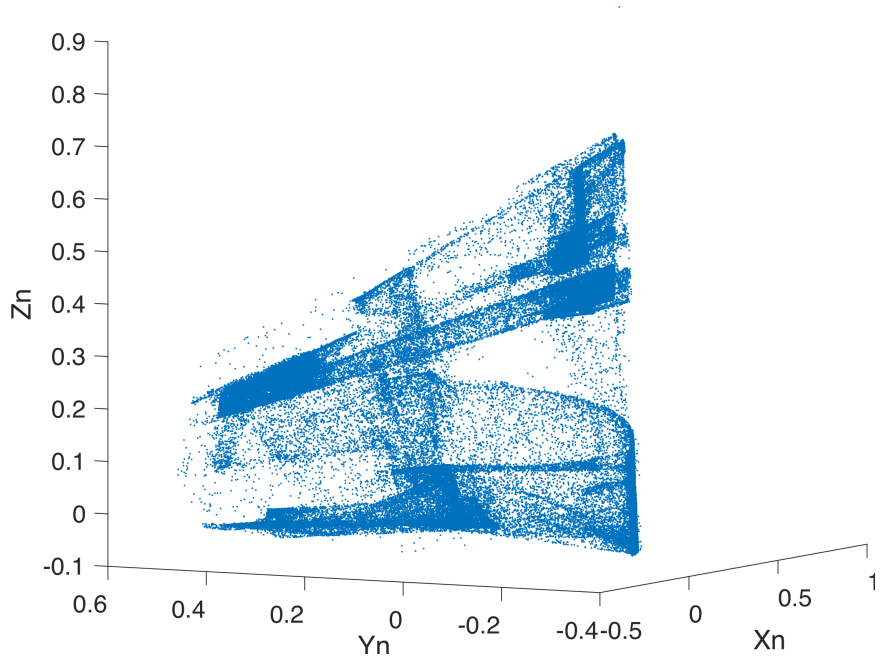

Figure 5.12 Plots of the orbits of the perturbed ring-oscillator model with initial conditions $(.99, .1, .9)$.

Source: A. Rahman and D. Blackmore. Threshold voltage dynamics of chaotic RS flip-flop circuits. arXiv:1507.03065, 2017.

5.5 Conclusions

We have introduced and analyzed a rather simple discrete (minimal) dynamical model for the RSFF circuit, which is based upon the iterates of a planar map. Moreover, we have proved that this model can be modified by arbitrarily small C^0 perturbations, motivated by the behavior of the electronic components used, to produce just about any dynamical property observed in physical realizations of RSFF and related flip-flop circuits. We have also shown that rather general small perturbations are apt to change the structurally stable minimal model to a two-dimensional discrete dynamical system with chaotic dynamics and related artifacts such as strange chaotic attractors.

Naturally, we are planning to extend this discrete dynamical systems approach to a much wider class of logical circuits and their perturbations, and verify the effectiveness of this approach by comparing our dynamic predictions with those of more standard ODE approaches as well as experimental data extracted from actual physical circuit measurements. We also plan to address a number of related questions such as showing that logical circuit realizations represent perturbations of our minimal models in some sense, and that the perturbations can actually be characterized and quantified. Such an investigation should provide insight into the relationship that we believe exists between our discrete dynamical systems approach and the underlying discrete dynamics of reconfigurable chaotic logic gates [38].

CHAPTER 6

ANALYSIS AND SIMULATIONS: QUALITATIVE MODELING OF NOR GATES AND RS FLIP-FLOP

In this chapter we analyze and simulate the mechanistic NOR gate and set/reset flip-flop models of Section 4.2. We first prove the existence of chaotic orbits in the models of the TCUs (Section 6.1). The first proof involves a simple translation and comparison with the tent map. The second proof, while more involved, utilizes the beautiful result of Li and Yorke [87]: "three cycle implies chaos". Then we compare the simulations of both our deterministic (Section 6.2) and stochastic (Section 6.3) models with experiments (Section 2.3.2) and *MultiSIM* simulations of the NOR gates, TCUs, and RSFF. Much of this work is presented in [137].

6.1 Chaos in Threshold Control Units

Here we shall prove the maps $g(1,1,x)$ and $f(1,1,x)$ become chaotic for certain parameters. First we prove this for $g(1,1,x)$, which employs a simple translation to the tent map.

Theorem 6.1.1. *The map $g(1,1,x)$ is chaotic for $\mu_g \geq 2$. In addition, it has a nonwandering set in the form of a translated Cantor set on $[1-\nu_g, \nu_g]$ for $\mu_g > 2$. Moreover, for $\mu = 3$, the nonwandering set is the middle-third Cantor set translated to the interval $[1-\nu_g, \nu_g]$.*

Proof. Consider the translation $(u,v) = H(x,y) : [1-\nu_g, \nu_g]^2 \to [0,1]^2$, defined as $(u,v) = (x+1-\nu_g, g(1,1,x)+1-\nu_g)$, applied to $g(1,1,x)$. This produces the map $v = T_{\mu_g(u)} : [0,1] \to [0,1]$, which is exactly the tent map. Since H is a conjugacy,

it suffices to analyze the tent map. It is well known that when $\mu \geq 2$, the tent map is chaotic. Furthermore, for $\mu > 2$, the nonwandering set is a Cantor set, and for $\mu = 3$, it is precisely the middle-third Cantor set. This shows the map $g(1, 1, x)$ is also chaotic for $\mu_g \geq 2$, and has a nonwandering set in the form of a translated Cantor set, thereby completing the proof. □

Now we prove $f(1, 1, x)$ is chaotic in the physical parameter regime outlined in Table 4.1. For the sake of brevity, we assume the parameters are in this regime for our next theorem. The main idea of the proof is to search for 3-cycles and use the main theorem by Li and Yorke [87]. Since the formula for f^3 becomes overly complex, we shall use properties of f^3 to show the existence of a 3-cycle rather than finding it explicitly, and we provide visual aids to illustrate the proof.

Theorem 6.1.2. *For every $n \in \mathbb{N}$ there exists a periodic point $p_n \in [-\mu_f\nu_f, \mu_f\nu_f]$ of the map $f(1, 1, x)$ having period n and $[-\mu_f\nu_f, \mu_f\nu_f]$ contains chaotic orbits of f. Furthermore, there exists an uncountable set $S \subset [-\mu_f\nu_f, \mu_f\nu_f]$ containing no periodic orbits.*

Proof. It is shown in [87] that a 3-cycle implies chaos. Now, we show there exists a 3-cycle for all parameter values in the physical regime. This is done by finding the roots of f^3 not including the fixed points, or rather showing they exist.

First, let P_n be the set of roots of f^n, then $P_3 \setminus P_1$ is the set of points having period 3. We observe f^3 (Figure 6.1) has 17 linear branches. Since these are linear, each branch may intersect the line $y = x$ at most once. The two outermost branches will never intersect the line $y = x$ for the parameter regime outlined in Table 4.1. Then $\max(\mathbf{card}(P_3)) = 15$ and $\mathbf{card}(P_1) = 3$ (i.e., f has three fixed points), hence $\max(\mathbf{card}(P_3 \setminus P_1)) = 12$. Notice, a 3-cycle exists only if $\mathbf{card}(P_3 \setminus P_1) \in \{6, 12\}$ due to the symmetry.

We observe (Figure 6.1a) $\mathbf{card}(P_3 \setminus P_1) = 12$ for the parameters near that used in simulations. If μ_f and ν_f are varied forward we maintain $\mathbf{card}(P_3 \setminus P_1) = 12$. If we vary them backward, the first instance $\mathbf{card}(P_3 \setminus P_1) \neq 12$ occurs when the cusps of the second and third branches from the left, and respectively from the right, lie on the line $f(1, 1, x) = x$. The cusps are located at

$$\hat{x} = \pm \left(\nu_f + \mu_f \nu_f \frac{\mu_f - 1}{\mu_f + 1} \; -\frac{\nu_f}{\mu_f} \frac{\mu_f - 1}{\mu_f + 1} \right), \qquad f(1, 1, \hat{x}) = \pm \mu_f \nu_f.$$

Then, solving $\hat{x} = f(1, 1, \hat{x})$ for μ_f, gives $\mu_f = 1$, which is unphysical. Since $\mathbf{card}(P_3 \setminus P_1) = 12$ in the parameter regime of Table 4.1, 3-cycles (in fact, four of them) exist. Therefore, the hypotheses of [87] is satisfied, thereby completing the proof. □

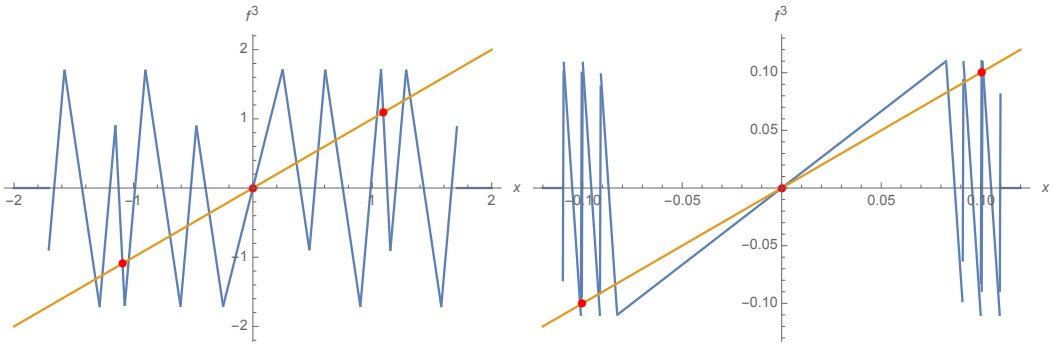

(a) $\mu_f = 1.9$, $\nu_f = 0.9$ (b) $\mu_f = 1.1$, $\nu_f = 0.1$

Figure 6.1 Plots of f^3 for parameters in the physical regime of Table 4.1 with parameters similar to that of the experiments and simulation and parameters just within the physical regime. It should be noted that the gaps between certain branches in Figure 6.1b are due to computational inaccuracy and in reality all branches connect.

Source: A. Rahman, I. Jordan, and D. Blackmore. Qualitative models and experimental investigation of chaotic NOR gates and set/reset flip-flops. arXiv:1702:04838, 2017.

6.2 Comparison of Deterministic Model with Experiments

From the models of the circuit we can simulate the NOR gate and RSFF operations. The codes for the simulations are quite simple with the majority of them dedicated to iterating (4.9) for both operations. For both the NOR gate and RSFF, we assume there is a "circuit frequency", which we define as the amount of time it takes a signal to traverse the entire circuit, and is on the order of 100 microseconds. We also set the following parameters: $\mu_f = 3.2$, $\nu_f = 0.5694$, $\mu_g = 2$, and $\nu_g = 1/3$.

Furthermore, for the NOR gate, while the model is not stochastic (no added noise), we do make small deterministic perturbations in the inputs to approximate the effects of noise and demonstrate sensitivity to initial conditions. For I_2 and I_4, from the 20 millisecond mark to the 40 millisecond mark we add 10^{-9}, and from the 60 millisecond mark to the 80 millisecond mark we subtract 10^{-9}. This equates to less than a nano-volt difference (recall the voltage used in the experiments is 1.84 volts). The simulations are shown in Figure 6.2.

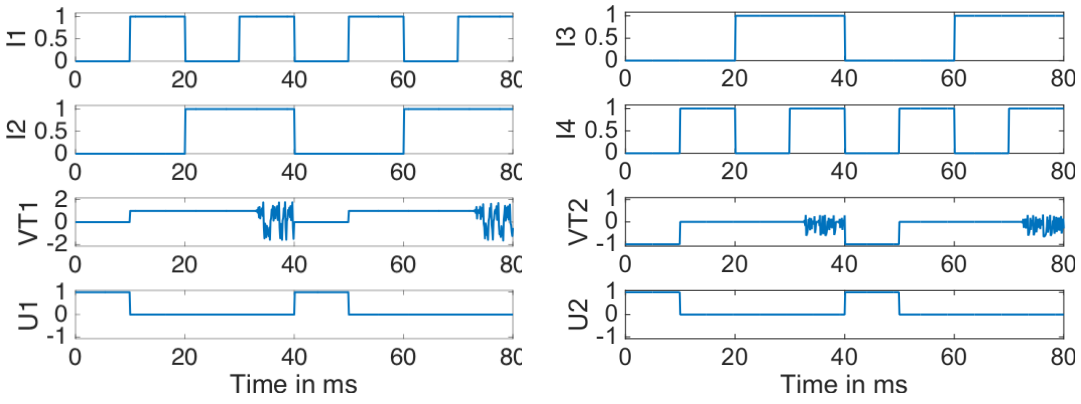

Figure 6.2 Simulations of the two input voltages, threshold voltage, and output voltages for the respective NOR gate operations.

Source: A. Rahman, I. Jordan, and D. Blackmore. Qualitative models and experimental investigation of chaotic NOR gates and set/reset flip-flops. arXiv:1702:04838, 2017.

Notice, we have surprisingly close agreement with Figure 2.8. The model even replicates the lag observed in the second threshold (in Figure 2.8 the second threshold voltage seems to remain close to zero for a few milliseconds). The only dynamics that were missed are the effects on the outputs at the clock edges. This shall be rectified in the sequel.

For the RSFF, we employ the same circuit frequency and perturbation on the initial conditions. This is plotted in Figure 6.3. Moreover, in the circuit design, the outputs are achieved by taking the difference between the voltage across the capacitors and their respective threshold voltages. However, we approach this from the other direction where we have a model for the outputs and threshold voltages and take the sum to predict the voltage across the capacitors. Since our system is discrete and the phase plane of Chua's circuit is continuous, we interpolate between the respective points. While this is not perfectly accurate, it illustrates a more complete picture of the dynamics than the purely discrete case. This is plotted in Figure 6.4.

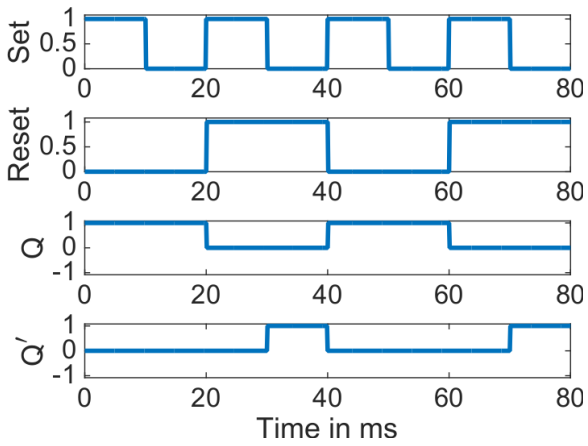

Figure 6.3 Plots of two input voltages and simulation of two output voltages for RSFF operations.

Source: A. Rahman, I. Jordan, and D. Blackmore. Qualitative models and experimental investigation of chaotic NOR gates and set/reset flip-flops. arXiv:1702:04838, 2017.

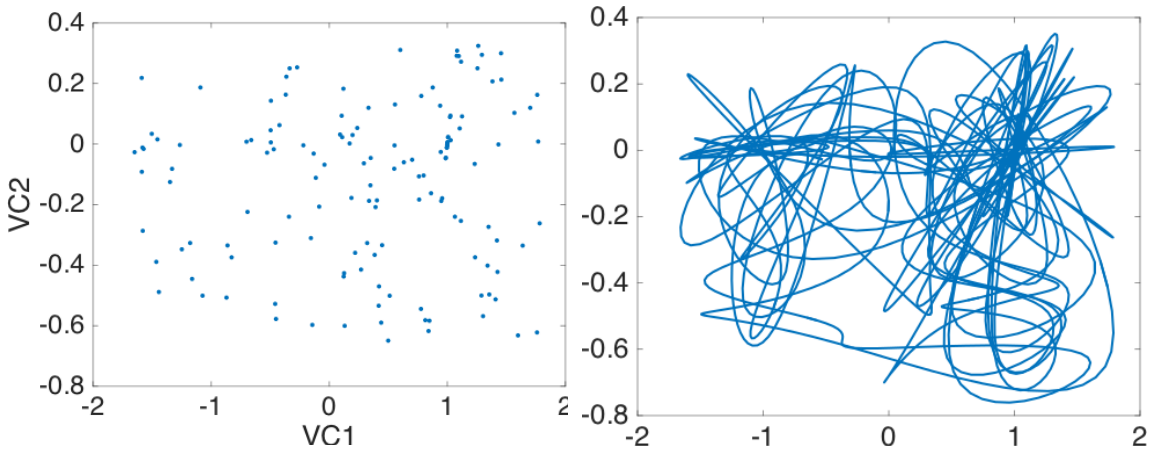

Figure 6.4 Simulation of the capacitor voltages. On the left we plot the individual points from the model. On the right we interpolate between these plots using 2000 points between each two iterates.

Source: A. Rahman, I. Jordan, and D. Blackmore. Qualitative models and experimental investigation of chaotic NOR gates and set/reset flip-flops. arXiv:1702:04838, 2017.

Again, as with the NOR gate, we are able to reproduce the behavior for the RSFF except for the clock edge effects. We also plot the iterate plane for the capacitor voltages. This can be thought of as iterates of a Poincaré map of the double scroll attractor. After interpolating between the iterates, we observe a double scroll like projection in the plane.

6.3 Comparison of Stochastic Model with Experiments

To simulate the models we use the same values for parameters in y_f and y_g, and for the circuit frequency, as Section 6.2. For the NOR gate and RSFF we set $M = N + 1 = T = 11$ (i.e., approximately 1 millisecond) and $\varepsilon = \pm O\left(10^{-8}\right)$. The choice of ε describes a physical signal which has less than 1 nano-volt of noise, on average. The simulations for the NOR gate are plotted in Figure 6.5. We observe that these are precisely the type of damped oscillations seen in Figure 2.8.

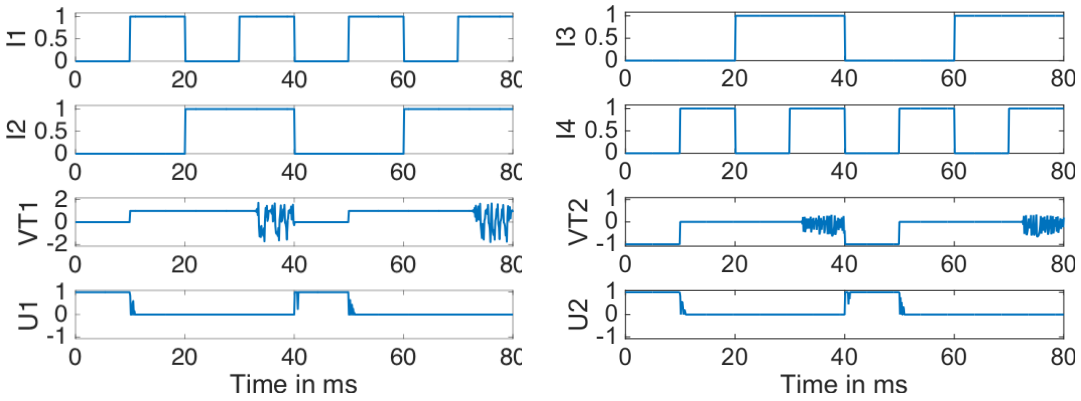

Figure 6.5 Stochastic simulations of the two input voltages, threshold voltage, and output voltages for the respective NOR gate operations.

Source: A. Rahman, I. Jordan, and D. Blackmore. Qualitative models and experimental investigation of chaotic NOR gates and set/reset flip-flops. arXiv:1702:04838, 2017.

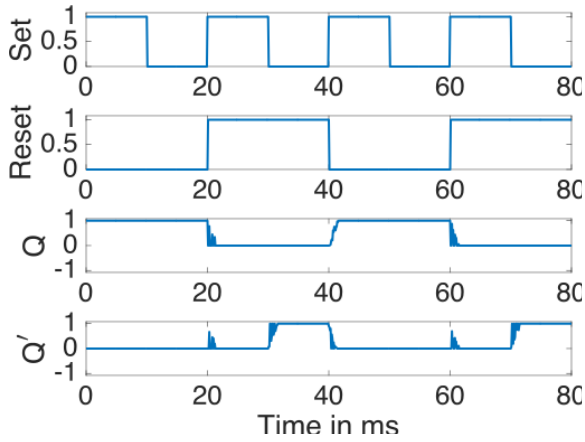

Figure 6.6 Plots of two input voltages and simulation of two output voltages for RSFF operations.

Source: A. Rahman, I. Jordan, and D. Blackmore. Qualitative models and experimental investigation of chaotic NOR gates and set/reset flip-flops. arXiv:1702:04838, 2017.

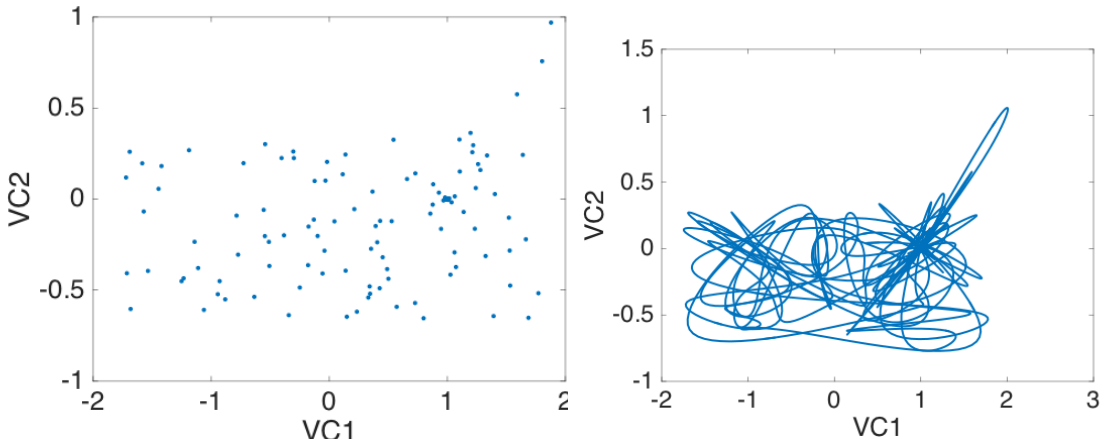

Figure 6.7 Stochastic simulation of the capacitor voltages. On the left we plot the individual points from the model. On the right we interpolate between these plots using 2000 points between each two iterates.

Source: A. Rahman, I. Jordan, and D. Blackmore. Qualitative models and experimental investigation of chaotic NOR gates and set/reset flip-flops. arXiv:1702:04838, 2017.

The RSFF and capacitor voltage simulations are plotted in Figure 6.6 and 6.7 respectively. Observe that the oscillations match the type in Figure 2.9b. Furthermore, Figure 6.7 is, now, qualitatively more similar to Figure 2.8b.

6.4 Conclusions

In the context of chaotic logical circuits there have been many *SPICE* simulations, some experiments, and only a few models. Simpler chaotic logical circuits are modeled as ordinary differential equations [118, 73]. More complex ones are generally studied using *SPICE* simulations [111, 110, 16] and physical realizations [111, 110]. We studied the RSFF/dual NOR gate through experiments, dynamical modeling, simulations, and analysis of the models.

By modifying the circuit in [16] we designed an RSFF/dual NOR gate using modern components. We then simulated the circuit using *MultiSIM* to confirm the new

design produces the proper outputs. Next we put together a physical realization of the circuit and conducted experiments to show agreement with *MultiSIM*. By observing the behavior of the circuit and using properties of TCUs as seen in [111, 110] we are able to model the dynamics of the circuit as difference equations. The chaotic behavior of the models is verified by standard dynamical systems analysis for one-dimensional maps. Finally, we simulate our models to show agreement with both experiments and *MultiSIM*. It was expected that the original deterministic models would not be sufficient to replicate the "race" behavior observed in the outputs. Therefore, we inserted probabilistic elements to show this edge-trigger phenomenon, thereby deriving a stochastic model.

While we are able to capture much of the behavior, there is a need for similarly simple models that replicate the more complex "race" behavior, which is not observed in any SPICE simulations. Furthermore, as this is a rich problem, and we have a physical realization, many new phenomena may arise. It shall be useful to study various physical bifurcations as we make changes in the circuit and make connections with topological bifurcations. We predict this will lead to local bifurcations such as transcritical, pitchfork, and Neimark–Sacker as observed in other models [9, 136], and novel global bifurcations previously unobserved in the literature. We shall also endeavor to build other more complex circuits to study analogs of other logic families and exploit the chaotic and logical properties for the purposes of encryption and secure communication.

CHAPTER 7

WALKING DROPLET EXPERIMENTS

In this Chapter we discuss the single particle diffraction experiment (Section 7.1), which initiated the study of hydrodynamic quantum analogs. Then we discuss walking in a circular corral and rotating frame (Section 7.2), and walking in an annular cavity (Section 7.3), which have strong connections to the discrete dynamical systems investigated in this thesis.

7.1 Single Particle Diffraction

In the seminal work of Couder and Fort [27] it is shown that walking droplets can reproduce quantum-like experiments. In their experiments, a bath of silicon oil is sinusoidally forced (Figure 7.1) with acceleration $\gamma = \gamma_m \cos(2\pi f_0 t)$ where γ_m is the forcing amplitude and f_0 is the frequency of the oscillatory force mechanism. Then a silicon oil droplet, which is much smaller than the domain of the bath, is dropped onto the bath. For the experiments the droplet is guided by an initial velocity towards either a single slit or double slit where the angle of incidence and angle of deflection are recorded and plotted as a histogram. The experimental setup is shown in Figure 7.2.

They observed surprising agreement between this experiment and single particle diffraction experiments in quantum mechanics. The histogram of the number of experiments that yielded the respective angle of deflection is shown in Figure 7.3.

The work of Couder *et al.* initiated other such quantum analog experiments.

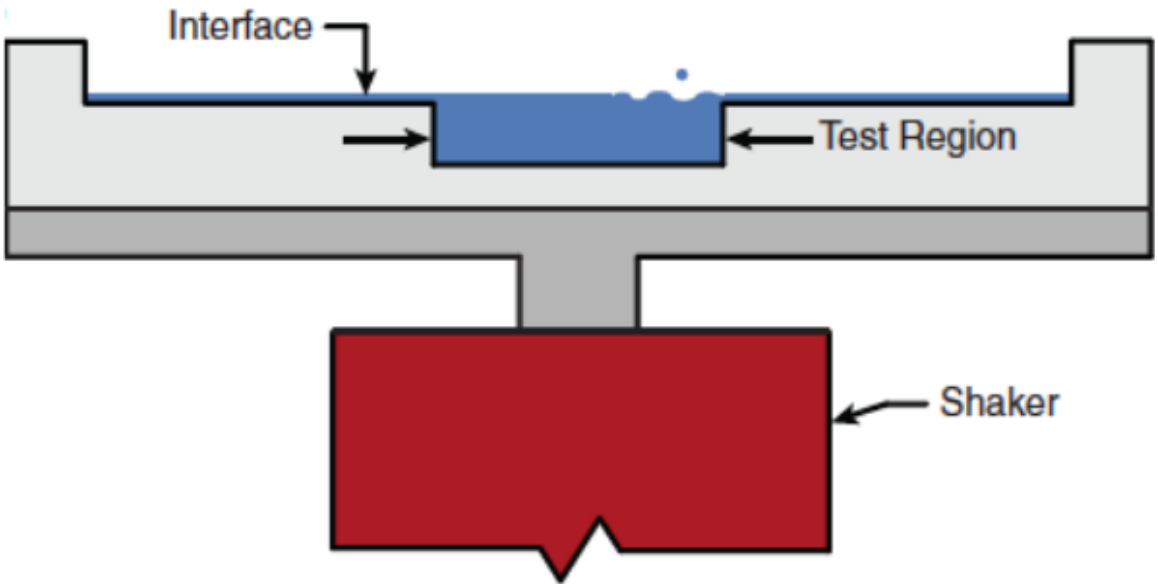

Figure 7.1 Schematic of sinusoidally forced table producing the vibrating bath. (Reproduced under *APS* thesis permissions).

Source: D. Harris, J. Moukhtar, E. Fort, Y. Couder, and J. Bush. Wavelike statistics from pilot-wave dynamics in a circular corral. *Phis. Rev. E*, 88:011001, 2013.

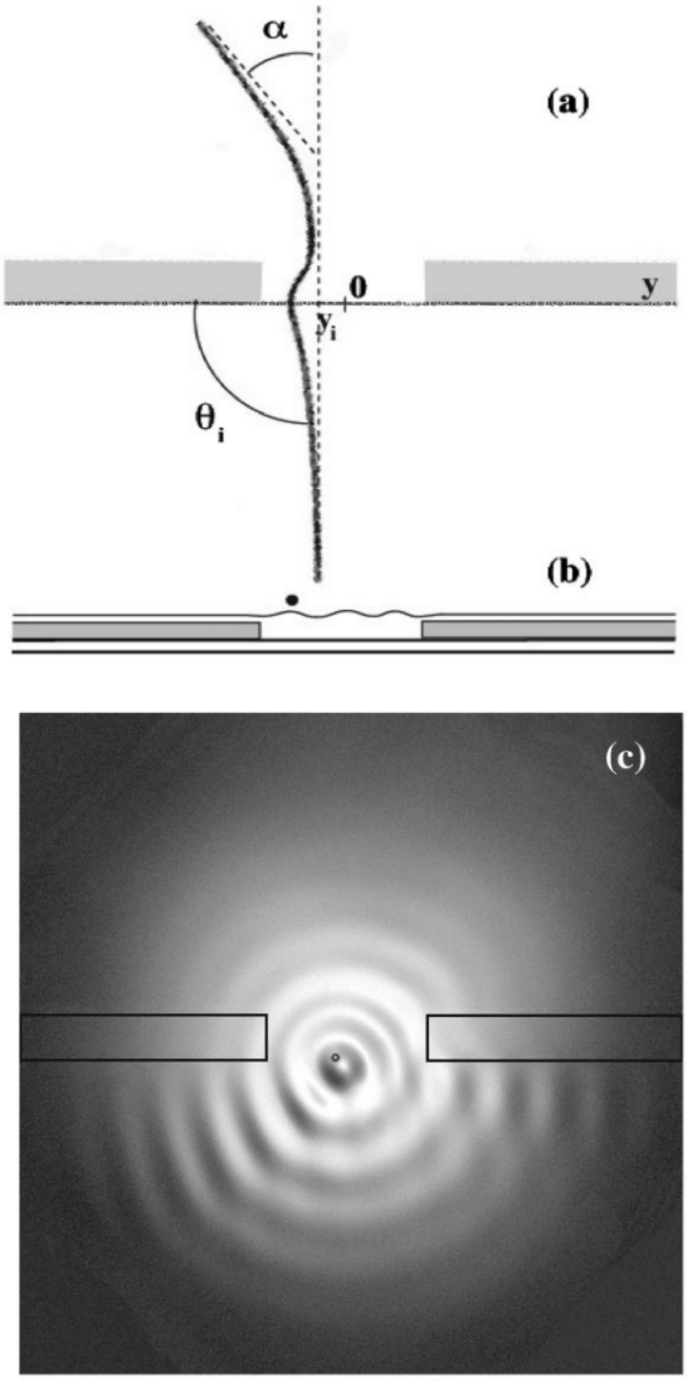

Figure 7.2 Experimental setup of single particle diffraction with walking droplets. (Reproduced with permission from *APS*).

Source: Y. Couder and E. Fort. Single-particle diffraction and interference at a macroscopic scale. *Phys. Rev. Lett.*, 97:154101, 2006.

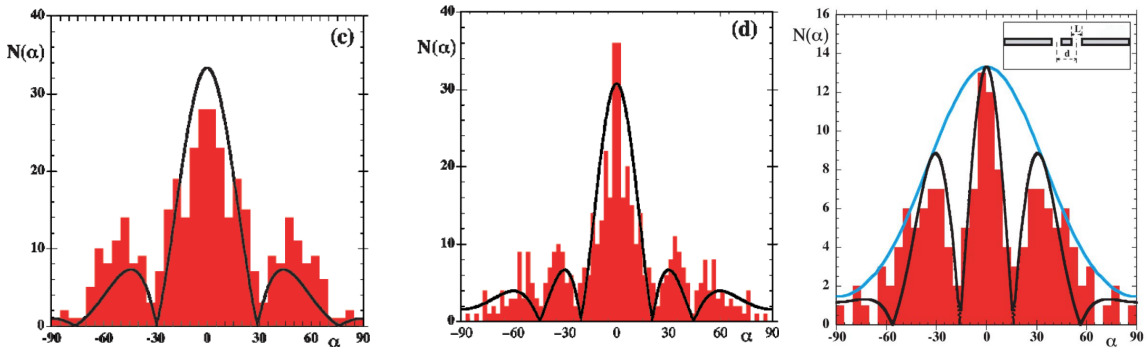

Figure 7.3 Histogram from single particle diffraction experiment, where the abscissa is the angle of deflection and the ordinate is the number of experiments with the respective angle of deflection. The solid lines represent an approximate fit of the histograms. Left: Single slit experiment where the width of the slit is approximately twice the Faraday wavelength. Center: Single slit experiment where the width of the slit is approximately three times the Faraday wavelength. Right: Double slit experiment where the width of the two slits are slightly larger than the Faraday wavelength and the distance between the two slits is approximately twice the width. (Reproduced and modified under *APS* thesis permissions).

Source: Y. Couder and E. Fort. Single-particle diffraction and interference at a macroscopic scale. *Phys. Rev. Lett.*, 97:154101, 2006.

7.2 Walker in a Circular Corral and Rotating Frame

More experiments reproducing quantum-like features were conducted, and two such experiment, by Fort *et al.* [48], Eddi *et al.* [41], and Harris *et al.* [59, 57, 58], were analogous to an electron trapped in a magnetic field [29] and the Zeeman effect (the splitting of spectral lines in the presence of a magnetic field) [170, 169]. The experimental setups are similar to [27]. For the circular corral, the walker is simply trapped in a small circle. For the rotating frame the walker is trapped in a larger circle, but the entire frame is now rotating as shown in Figure 7.4.

Since these walking droplets have already been shown to reproduce quantum-like features, it is reasonable to expect the circular corral to reproduce statistics similar to the *quantum corral* (electrons trapped in a bounded domain) in [29]. In the experiment, the droplet is tracked and a probability distribution of the droplet's position is recorded. In Figure 7.5 Harris *et al.* show statistics very similar to the quantum corral.

The addition of rotation introduces a Coriolis force, which an effect on the walker analogous to that of the force from a perpendicular magnetic field on an electron. In addition to analogs of the quantum corral, they also observe the quantization of orbital radii shown in Figure 7.6.

The experiments shown in this section may have connections with discrete dynamical models, but the connections would be tenuous. We would like to have the ability to refer to an experiment that can be directly modeled as a discrete dynamical system.

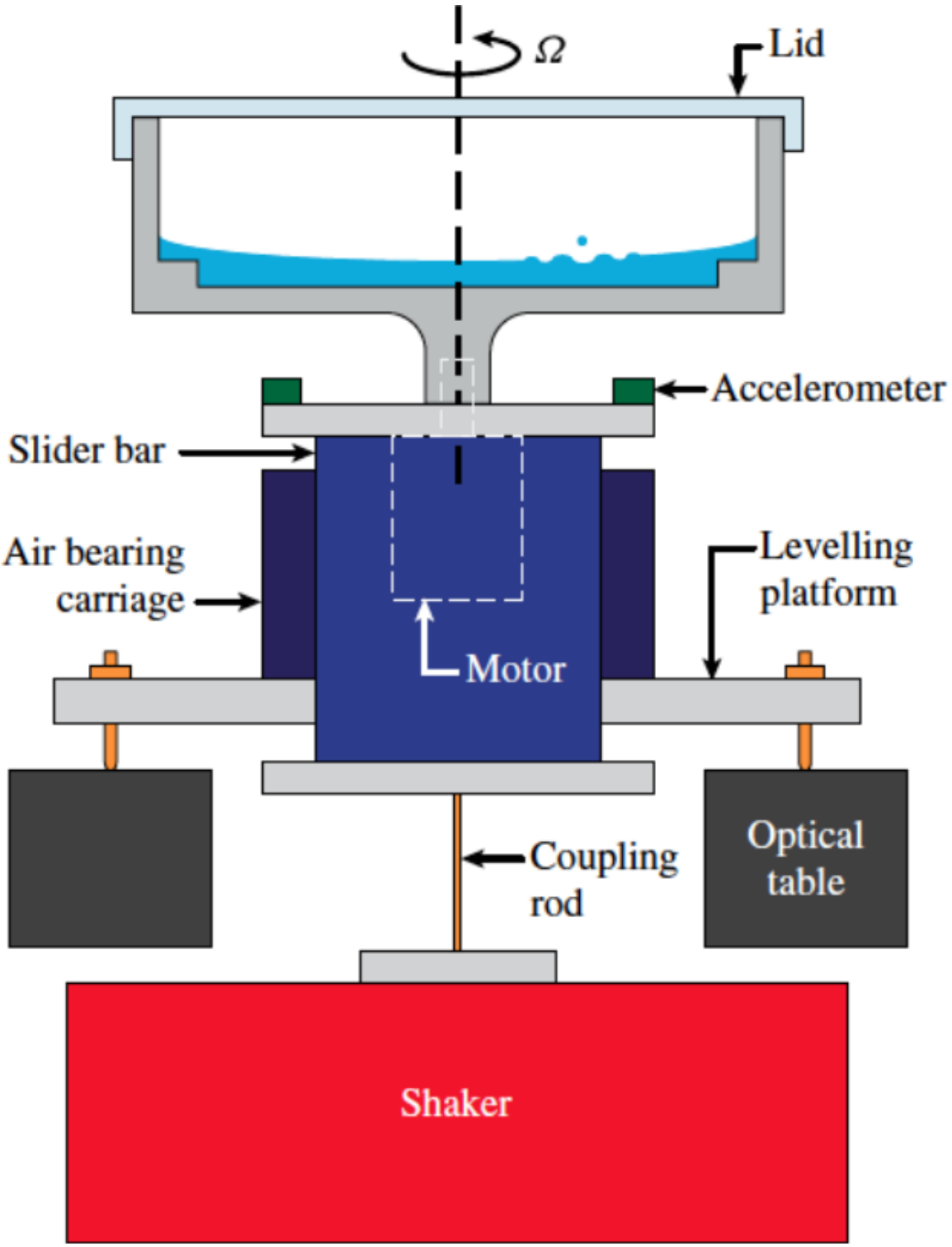

Figure 7.4 The experimental setup for a sinusoidally forced rotating frame. (Reproduced with permission from *Cambridge University Press*).

Source: D. Harris and J. Bush. Droplets walking in a rotating frame: from quantized orbits to multimodal statistics. *J. Fluid Mech.*, 739: 444-464, 2014.

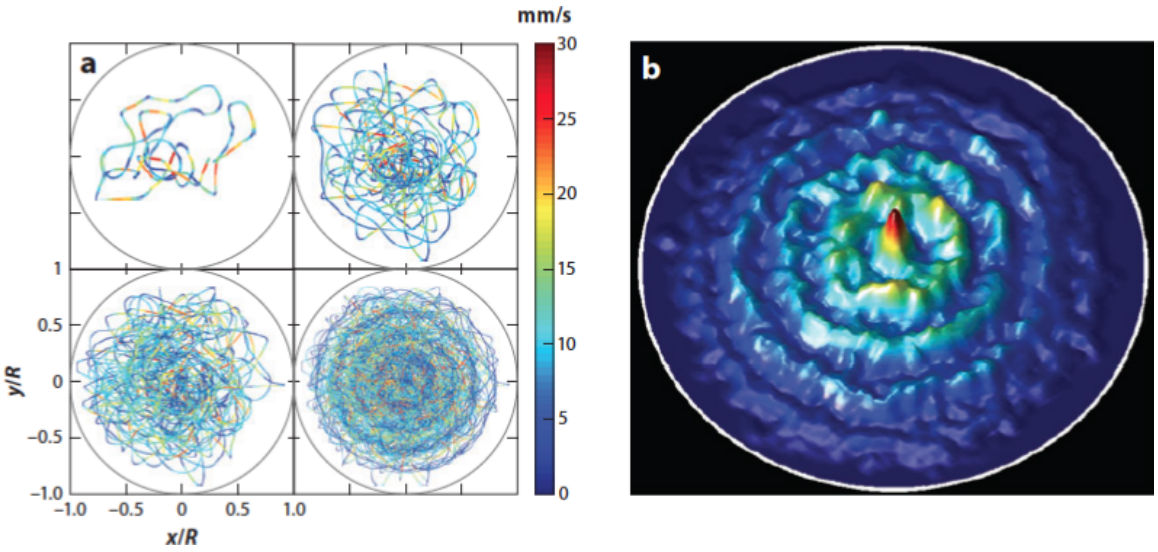

Figure 7.5 Statistics of the droplet trajectory in a circular corral. (a) Snapshots of the recorded path of the walker at increasing times: top left, top right, bottom left, bottom right. (b) Rendering of the final snapshot of the walker's path with height (and color) corresponding to the amount of total time the walker spent in that region. (Reproduced with permission from *Annual Reviews*).

Source: J. Bush. Pilot-wave hydrodynamics. *Ann. Rev. Fluid Mech.*, 49: 269-292, 2015.

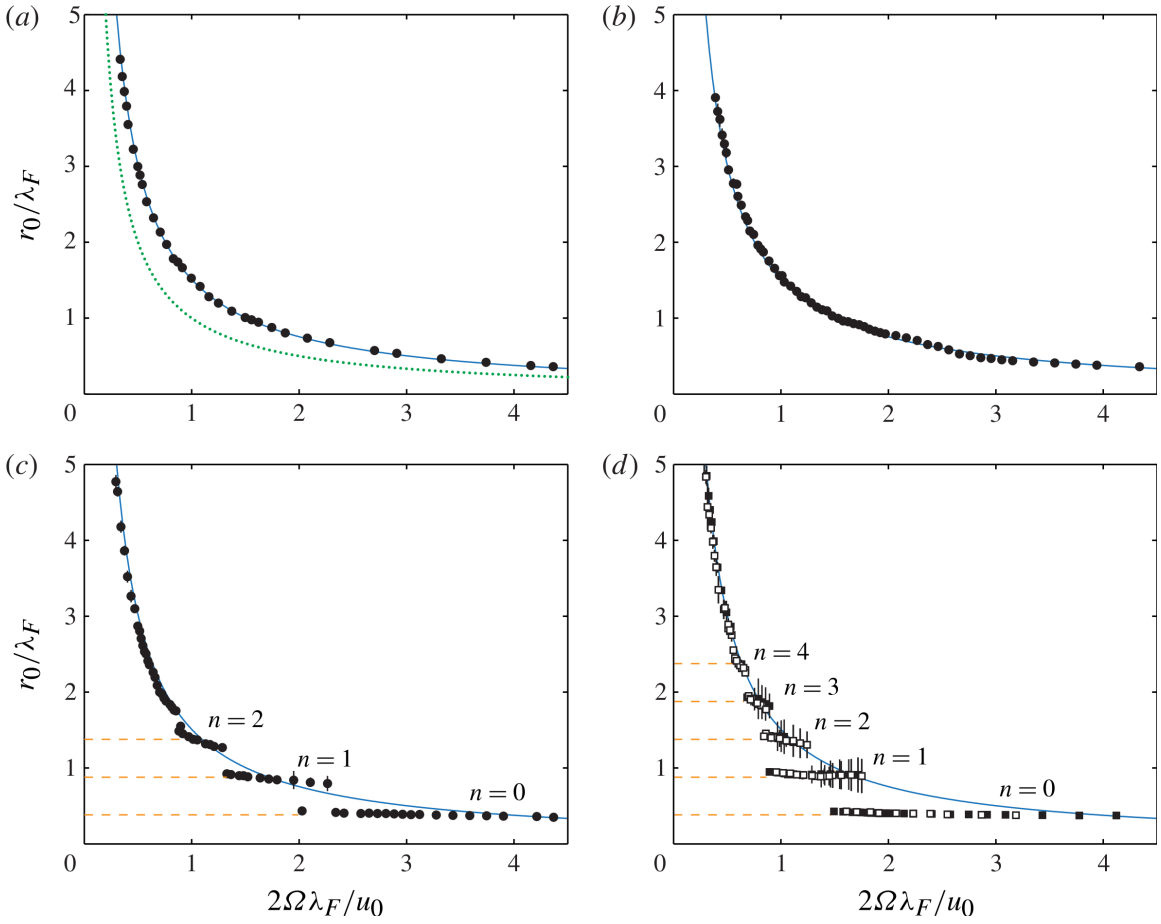

Figure 7.6 Observations of quantized orbital levels for the high memory regime in (c) and (d). In (a) and (b) no quantization is observed. (Reproduced with permission from *Cambridge University Press*).

Source: D. Harris and J. Bush. Droplets walking in a rotating frame: from quantized orbits to multimodal statistics. *J. Fluid Mech.*, 739: 444-464, 2014.

7.3 Walker Trapped in an Annulus

Recently, Filoux *et al.* developed an experiment for walkers in an annular cavity [44] and they modeled the dynamics in a similar manner to [42]. They too have an experimental setup similar to [27], with the major difference being the added boundaries. The experiment if first performed with only one droplet, which gives them a typical velocity. Then multiple droplets are added to the experiment. When two droplets added they bounce asynchronously; that is when one droplet impacts the bath the other is in the air and vice versa. When there are more than two, each sequential drop is asynchronous. Figure 7.7 shows an experiment with seven droplets. As we observe, there are four impacting the surface and three in the air.

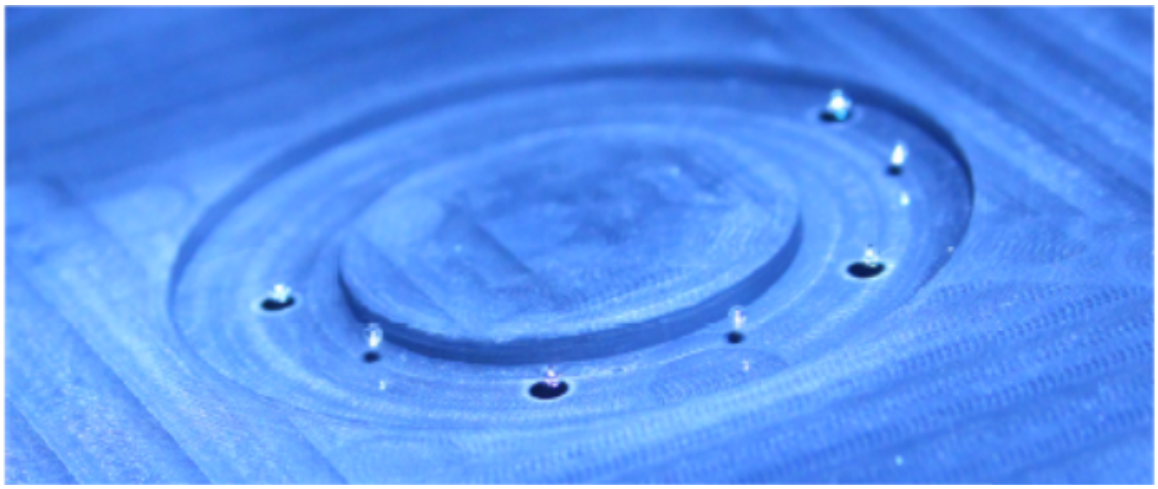

Figure 7.7 Multiple walkers traversing an annular cavity. (Reproduced under *APS* thesis permissions).

Source: B. Filoux, M. Hubert, and N. Vanderwalle. Strings of droplets propelled by coherent waves. *Phys. Rev. E*, 92:041004(R), 2015.

While the model of Filoux *et al.* [44] is not a discrete dynamical system, their experiment presents an opportunity to connect discrete dynamical models, such as in Section 9.2.3 and Chapter 10. This connection between theory and experiments would

allow us to understand these systems better and perhaps lead us to simplifications of more complex models.

CHAPTER 8

TRADITIONAL MODELING TECHNIQUES: WALKING DROPLETS

In Chapter 7 we discussed four experiments on walking droplets. In order to better understand these experiments and the phenomena themselves, it is necessary to derive hydrodynamic models rooted in first principles and simple enough for numerical solutions. In this Chapter we discuss the models developed by Oza *et al.* for walkers in free space and the rotating frame (Section 8), which were investigated mainly through simulations.

8.1 Description

Oza *et al.* developed and studied, via simulations, integro-differential models for walkers in free space [120] and in a rotating frame [119, 121]. In [120], Oza *et al.* developed an integro-differential model for walkers in free space. They assume, for a single bounce, the droplet is governed by the usual equation of motion including drag and with forcing proportional to the slope of the surface during contact. For example, if the surface is flat upon contact, the droplet will not move. On the other hand, if the surface is deformed, the droplet moves with a velocity of equal magnitude and and angle supplementary to the angle of incidence.

In experiments it is observed that waves are produced at each bounce when the fluid bath is sinusoidally forced. Each bounce excites an eigenmode, which decays with time and contributes to the total wave field in the bath. The wave field contains "cavities", the slopes of which cause the droplet to move. Oza *et al.* make the simplifying assumption that each eigenmode is a Bessel function centered at the

position of the bounce immediately after impact. They also approximate the sum of previous bounces as an integral from negative infinity to the current time, i.e., the droplet has been bouncing forever, which is a reasonable approximation after many impacts.

Taking these assumptions into consideration, the model they developed is

$$\kappa\ddot{x} + \dot{x} = \beta \int_{-\infty}^{t} \frac{J_1(|x(t) - x(s)|)}{|x(t) - x(s)|}(x(t) - x(s))e^{s-t}ds, \tag{8.1}$$

where x is the position of the droplet, $\kappa = m/(DT_F M_e)$ is the nondimensional mass, $\beta = (Fk_F T_F M_e^2)/D$ is the nondimensional memory force coefficient, m is the mass of the droplet, D is the drag coefficient, g is acceleration due to gravity, T_F is the Faraday period (the period of the surface waves), A is the amplitude of a single surface wave, k_F is the Faraday wavenumber, T_d is the decay time in the case of no forcing, γ is the acceleration of sinusoidal forcing, γ_F is the Faraday instability threshold (the acceleration required for the existence of Faraday waves), $F = mgAk_F$ is the memory force coefficient, and M_e is the memory (inversely proportional to the damping).

In [119] Oza *et al.* developed an integro-differential model for walkers in a rotating frame. The assumptions are the same as walking in free space, however there is an additional term due to the Coriolis effect: $-2m\Omega \times \dot{x}$. Here Ω is the angular frequency of the fluid bath, and this addition modifies the model to

$$\kappa\ddot{x} + \dot{x} = \beta \int_{-\infty}^{t} \frac{J_1(|x(t) - x(s)|)}{|x(t) - x(s)|}(x(t) - x(s))e^{s-t}ds - 2m\Omega \times \dot{x}. \tag{8.2}$$

8.2 Basic Properties

In [120] Oza *et al.* conducted a linear stability analysis on the position of the droplet in free space. Further, in [119] they analyze the stability of orbital solutions (i.e., paths of fixed radii) in the rotating frame. We shall briefly discuss their findings here.

Oza *et al.* first study the transition between bouncing and walking, which they observe occurs when $\gamma \geq \gamma_w$, where

$$\gamma_w := \gamma_F \left(1 - \sqrt{\frac{F k_F T_d^2}{2DT_F}}\right). \tag{8.3}$$

When the bouncing state destabilizes, the droplet transitions to straight-line walking with constant speed, and remains in this state for $\gamma_w < \gamma < \gamma_F$. The base walking speed used in [120] is

$$u = \frac{1}{k_F T_d}\left(1 - \frac{\gamma}{\gamma_F}\right)\sqrt{\frac{1}{4}\left[-1 + \sqrt{1 + 8\left(\frac{\gamma_F - \gamma_w}{\gamma_F - \gamma}\right)^2}\right]^2 - 1} \tag{8.4}$$

It is observed that perturbations in the direction of walking decay, and transverse perturbations neither decay nor grow.

For the rotating frame, Oza *et al.* first search for orbital solutions by writing (8.2) as

$$\begin{aligned} -\kappa r\omega^2 &= \beta \int_0^\infty J_1\left(2r \sin\frac{\omega z}{2}\right)\sin\frac{\omega z}{2} e^{-z} dz + \Omega r\omega \\ r\omega &= \beta \int_0^\infty J_1\left(2r \sin\frac{\omega z}{2}\right)\cos\frac{\omega z}{2} e^{-z} dz \end{aligned} \tag{8.5}$$

Then low memory, mid memory, and high memory approximations via asymptotic methods are studied. When the radii are either small ($r \ll 1$) or large ($r \gg \sqrt{\beta}$), the orbits are stable. However, between these limits the radii form sets of linearly stable (when $d\Omega/dr < 0$) and linearly unstable (when $d\Omega/dr > 0$) orbits.

After the linear stability analysis, they begin to focus on simulations and matching theoretical results with experimental results.

8.3 Simulations

Perhaps the most compelling results from [120, 119, 121] are the simulations. In [120], the simulations support the linear stability analysis of the motion of the droplet. Further, in [119, 121], Oza *et al.* show surprising agreement between the simulations and experiments. In one such simulation and experiment the frequency of the rotations of the fluid bath versus the orbital radius and frequency are plotted. It should be noted that the plots are scaled or inverted for the sake of clarity.

In Figure 8.1, the blue portions correspond to stable orbits, the green portions correspond to unstable orbits with $d\Omega/dr < 0$, and the red portions correspond to unstable orbits with $d\Omega/dr > 0$. Here, Oza *et al.* illustrate the dependence of orbital radius and frequency on the rotation frequency of the bath. The first thing we observe is the discrepancy between simulation and experiment for high orbital frequency. This may be due to the drag playing a larger part at larger velocities. Other than this, what is striking is the agreement for the orbital radius of all radii, or more precisely the radii scaled by the reciprocal of the Faraday wavelength. They strengthen their case by showing many more comparisons with experiments similar to this.

In [121], Oza *et al.* show numerical observations of exotic trajectories as illustrated in Figure 8.2. While many of these orbits have not been observed in experiments, the agreement that is observed for simpler orbits give us confidence that these orbits may exist. Furthermore, these trajectory types produce nontrivial topological structures, especially the quasiperiodic and chaotic trajectories. Discrete dynamical models similar to those studied in Chapters 9 and 10 may provide connections to these trajectories via Poincareé sections.

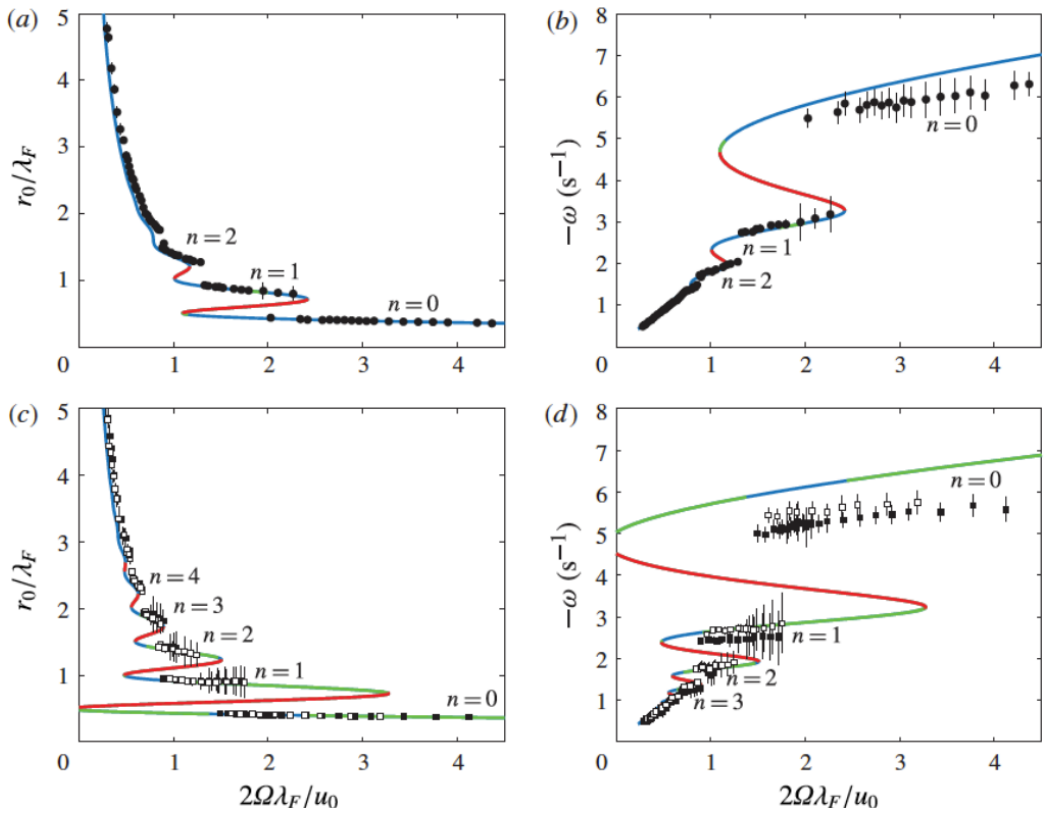

Figure 8.1 Panels (a) and (c) show the dependence of the orbital radius on bath rotation frequency, and panels (b) and (d) show the dependence of the orbital frequency on bath rotation frequency. The fluid bath in (c) and (d) is being forced harder than in (a) and (b). (Reproduced with permission from *Cambridge University Press*).

Source: A. Oza, D. Harris, R. Rosales, and J. Bush. Pilot-wave dynamics in a rotating frame: on the emergence of orbital quantization. *J. Fluid Mech.*, 744: 404-429, 2014.

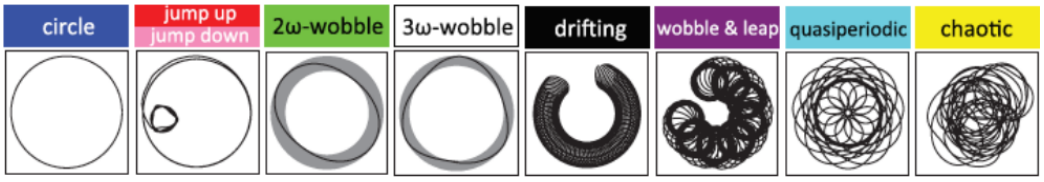

Figure 8.2 Various trajectory types observed in simulations of droplets walking in a rotating frame. (Reproduced with permission of *AIP Publishing*).

Source: A. Oza, O. Wind-Willassen, D. Harris, R. Rosales, and J. Bush. Pilot-wave dynamics in a rotating frame: Exotic orbits. *Phys. Fluids*, 26:082101, 2014.

CHAPTER 9

DISCRETE DYNAMICAL MODELS: WALKING DROPLETS

While the models in Chapter 8 agree very well with experiments, the equations are quite difficult to study analytically. The complexity of the equations naturally created interest in developing realistic simplified mathematical models exhibiting important dynamical features of the original ones, while being easier to analyze. The first models to exploit the discrete nature of the bouncing/walking were developed by Fort *et al.* [48] and later Eddi *et al.* [42]. Several other such reduced models were developed with two of them, devised by Shirokoff [146] and Gilet [49], showing considerable promise are planar discrete dynamical system models. Shirokoff [146] developed a model in which he derived a map for the motion of a particle in a square cavity. In this model, using numerics, he discovered cascading period doubling bifurcations (Theorem 1.1.2), which is indicative of chaos. Gilet [49] included the amplitude of subsequent modes in his model (9.7) for the straight line motion of a particle. He observed what appeared to be a Neimark–Sacker (N–S) bifurcation in numerous simulations, and so conjectured its existence and type.

In this chapter we describe the two discrete dynamical models. First we give a brief description of Shirokoff's model of walkers in a two-dimensional cavity (Section 9.1). Then, we give a more detailed description of Gilet's model (Section 9.2); first we discuss the simplifying assumptions and derivation of the model and then a detailed linear stability analysis follows [135].

9.1 Shirokoff Model

In [146], Shirokoff derived a discrete dynamical model and analyzed simulations of a walking droplet in a two-dimensional bounded domain. He made two general assumptions: the force on the particle is proportional to the slope of the wave field at the point of impact and the particle produces a crater displacing a volume of fluid only at the point of impact. Using these assumptions, he derived the map

$$\begin{aligned} y_{n+1} &= y_n + v_n, \\ v_{n+1} &= (1-\gamma)v_n - F\nabla h(y_{n+1}), \end{aligned} \tag{9.1}$$

where y is the position of the droplet, v is the velocity of the droplet, h is the wave field profile, n denotes the most recent impact, and γ is the dissipation factor.

Shirokoff then modeled the wave field by considering gravity-capillary waves. He first did so in free space, for which the velocity equation becomes

$$v_{n+1} = (1-\gamma)v_n - F\sum_{k=0}^{n-1} \nabla h(y_{n+1}, r_{n-k}), \tag{9.2}$$

where r is the radial distance from the impact position y. He then made the assumption that the most recent bounce contributes the most to the walkers position and velocity. This gives us a simpler velocity equation:

$$v_{n+1} = (1-\gamma)v_n - F\nabla h(y_{n+1}, r_n). \tag{9.3}$$

Using the bath forcing magnitude, with F as the bifurcation parameter, Shirokoff found evidence of period doubling bifurcations in the velocity through simulations as shown in Figure 9.1 He then studied bifurcations using the dissipation as a parameter. Finally, Shirokoff analyzed the requirements for walking in his model and the movement of the droplet in a square.

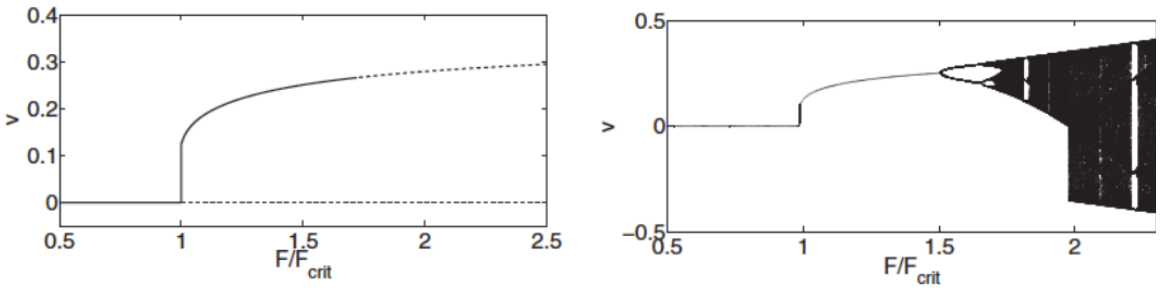

Figure 9.1 Example of period doubling in the Shirokoff model. (Reproduced with permission of *AIP Publishing*).

Source: D. Shirokoff, Bouncing droplets on a billiard table. *Chaos*, 23:013115, 2013.

While the model (9.1) is simpler than the integro-differential models from Chapter 8, it is still not amenable to dynamical systems analysis.

9.2 Gilet Model

In this section, we first summarize the simplifying assumptions and derivation of the model from [49]. Then, we revisit the basic properties, while approaching the linear stability analysis from a purely dynamical systems point of view. This in turn sets up the theoretical foundation for the bifurcation analysis in Chapter 10.

9.2.1 Derivation

In [49], Gilet began his description of the problem by considering impacts exciting complex orthonormal eigenmodes $\Psi_k(x)$, of the Faraday wave field $h_n(x)$, that are pinned at the boundary of domain Ω, with amplitude $W_{k,n}$, where n is the current impact and $k \leq n$ are past impacts. The wave field can be written as the decomposition

$$h_n(x) = \sum_{k=1}^{n} W_{k,n} \Psi_k(x). \tag{9.4}$$

At each impact, a radially symmetric crater, denoted as $f(r)$, is initially formed, where r is the distance from the center of the crater. Assuming the radius of the crater is small compared to the characteristic wavelength of the eigenmodes, the function can be approximated as $f(r) = A\delta(r)$. He then normalized $h_n(x)$ by A. It should be noted, that unlike [146], [49] assumes there are no traveling capillary waves.

After briefly describing the problem and simplifying assumptions, Gilet derived a discrete model for the amplitude of each mode and the position of the walker. He introduced a damping factor μ_k, associated with the memory parameter M_k of mode k with the equation $\mu_k^{M_k} = 1/e$. This is defined as the ratio of amplitudes of an eigenmode in the instance before an impact and that of the instance after the previous impact; that is

$$\mu_k = \frac{W_{k,n+1}}{\Psi_k^*(x_n) + W_{k,n}}, \tag{9.5}$$

where Ψ_k^* is the complex conjugate of Ψ_k. Furthermore, it is assumed the droplet velocity is proportional to the slope of the wave field at the position of impact; that is the distance between an impact and the next impact is proportional proportional to the slope of wave field $h_n(x)$ at the impact position x_n. We write this as

$$x_{n+1} - x_n = -C \sum_{k=1}^{n} W_{k,n} \nabla \Psi_k(x_n), \tag{9.6}$$

where C is associated with the size of the droplet, which determines the strength of wave-particle coupling.

Now, if we restrict the domain to one-dimensional free space, we have a single eigenmode $\Psi(x) \in \mathbb{R}$, and the associated amplitude w_n at an impact n. Then the

model becomes the discrete dynamical system (difference equation):

$$\begin{aligned} w_{n+1} &= \mu\left[w_n + \Psi(x_n)\right], \\ x_{n+1} &= x_n - C w_n \Psi'(x_n). \end{aligned} \tag{9.7}$$

We illustrate this system in Figure 9.2. It should be noted that by definition μ, $C \in [0,1]$ and x, w, $\Psi \in \mathbb{R}$. When $\mu = 0$, there is only bouncing and the model returns trivial results, and when $\mu = 1$, the forcing is so strong that Faraday waves exist; that is there are waves without a droplet being present. For $C = 0$, the droplet is nonexistent, and $C = 1$ represents a droplet so large that the difference in position is exactly the gradient of the wave field at the n^{th} impact.

The discrete dynamical system (9.7) is analyzed in more detail in below and in Chapter 10.

9.2.2 Basic Properties of the Map

In this section we find the fixed points as done in [49]. Then we analyze the stability of the fixed points for two cases: holding C constant and holding μ constant. It should be noted that a family of fixed points is defined as a set of multiple fixed points, and all calculations are done without loss of generality.

First, define $F : \mathbb{R}^2 \mapsto \mathbb{R}^2$ as,

$$\begin{bmatrix} w_{n+1} \\ x_{n+1} \end{bmatrix} = F(w_n, x_n) = \begin{bmatrix} \mu[w_n + \Psi(x_n)] \\ x_n - C w_n \Psi'(x_n) \end{bmatrix} \tag{9.8}$$

We find the fixed points of (9.7) by solving,

$$\begin{aligned} w_* &= \mu[w_* + \Psi(x_*)] \\ x_* &= x_* - C w_* \Psi'(x_*). \end{aligned}$$

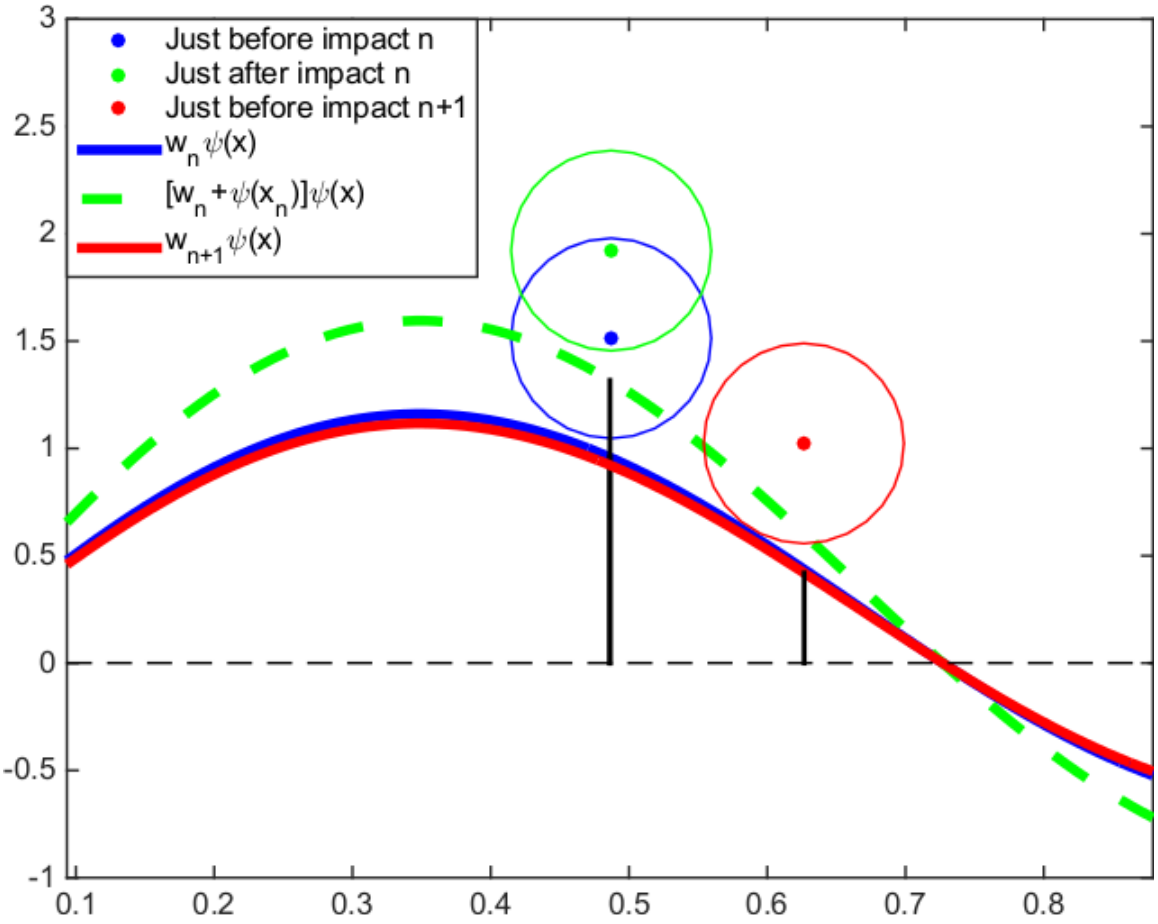

Figure 9.2 Diagram of the discrete dynamical system model (9.7) where the abscissa corresponds to the position x of the droplet and the ordinate corresponds to the wave amplitude w.

Source: A. Rahman and D. Blackmore. Neimark–Sacker bifurcations and evidence of chaos in a discrete dynamical model of walkers. *Chaos, Solitons & Fractals*, 91: 339-349, 2016.

Notice that this gives us two families of fixed points:

$$(0, x_*) \text{ such that } \Psi(x_*) = 0;\ \mu \neq 0 \text{ and} \tag{9.9}$$

$$(\hat{w}_*, \hat{x}_*) \text{ such that } \hat{w}_* = \frac{\mu}{1-\mu}\Psi(\hat{x}_*), \Psi'(\hat{x}_*) = 0;\ C \neq 0, \mu \neq 1. \tag{9.10}$$

The derivative matrix of F is,

$$DF(w, x) = \begin{pmatrix} \mu & \mu\Psi'(x) \\ -C\Psi'(x) & 1 - Cw\Psi''(x) \end{pmatrix}. \tag{9.11}$$

Properties of F in Neighborhoods of the Second Family. We first notice that for fixed points (9.10), $\mu \in [0, 1)$ and $C \in (0, 1]$ because if $\mu = 1$ or $C = 0$ this fixed point does not exist. Substituting the fixed points (9.10) into the derivative matrix (9.11), we obtain

$$DF(\hat{w}_*, \hat{x}_*) = \begin{pmatrix} \mu & 0 \\ 0 & 1 - \frac{\mu C}{1-\mu}\Psi(\hat{x}_*)\Psi''(\hat{x}_*) \end{pmatrix}.$$

Therefore, the eigenvalues are

$$\lambda_1 = \mu,\ \lambda_2 = 1 - \frac{\mu C}{1-\mu}\Psi(\hat{x}_*)\Psi''(\hat{x}_*)$$

Observe that since $\mu \in [0, 1)$, if $\Psi(\hat{x}_*)\Psi''(\hat{x}_*) < 0$ the fixed point is a saddle. However, if $\Psi(\hat{x}_*)\Psi''(\hat{x}_*) > 0$, we always have $\lambda_2 < 1$, so we must find a condition for which $\lambda_2 = -1$.

If we hold C constant we derive the condition:

$$\hat{\mu} = \frac{1}{1 + C\Psi(\hat{x}_*)\Psi''(\hat{x}_*)/2}.$$

Then, for $\mu < \hat{\mu}$ the fixed points (9.10) are sinks and for $\mu > \hat{\mu}$ they are saddles. If $\mu = \hat{\mu}$, the fixed point is not hyperbolic.

If we hold μ constant we derive the condition $\hat{C}$,

$$\hat{C} = \frac{2(1-\mu)}{\mu\Psi(\hat{x}_*)\Psi''(\hat{x}_*)}. \tag{9.12}$$

If $C < \hat{C}$ the fixed points (9.10) are stable, but if $C > \hat{C}$ the fixed points are saddles. When $C = \hat{C}$, $\lambda_2 = -1$, which indicates the possibility of a flip bifurcation.

When the fixed point is a saddle, it is easy to see that the linear stable and unstable manifolds are,

$$W^s_{\text{lin}} = \{(w, x) : x = \hat{x}_*\}, \tag{9.13}$$

$$W^u_{\text{lin}} = \left\{(w, x) : w = \hat{w}_* \frac{\mu}{1-\mu}\Psi(\hat{x}_*)\right\}. \tag{9.14}$$

Properties of F in Neighborhoods of the First Family. Since we can translate any fixed point (9.9) to the origin, without loss of generality, we assume the fixed point is $(w_*, x_*) = (0, 0)$ with the relevant conditions on Ψ'. Substituting the fixed point (9.9) into the derivative matrix (9.11), we obtain

$$DF(0,0) = \begin{pmatrix} \mu & \mu\Psi'(0) \\ -C\Psi'(0) & 1 \end{pmatrix}. \tag{9.15}$$

The characteristic polynomial is

$$(\mu - \lambda)(1 - \lambda) + C\mu\Psi'(0)^2 = 0 \Rightarrow \lambda^2 - (1+\mu)\lambda + \mu(1 + C\Psi'(0)^2) = 0,$$

and the eigenvalues are

$$\lambda = \frac{1}{2}(1+\mu) \pm \frac{i}{2}\sqrt{4\mu(1 + C\Psi'(0)^2) - (1+\mu)^2}. \tag{9.16}$$

Notice that $\lambda \in \mathbb{C} \setminus \mathbb{R}$ if $4\mu(1 + C\Psi'(0)^2) - (1+\mu)^2 > 0$.

Holding C constant gives us the condition,

$$2C\Psi'(0)^2 - 2\sqrt{C\Psi'(0)^2(C\Psi'(0)^2+1)} + 1 < \mu < 2C\Psi'(0)^2 + 2\sqrt{C\Psi'(0)^2(C\Psi'(0)^2+1)} + 1. \tag{9.17}$$

Now, if $|\lambda| < 1$, we get a stable focus, and when $|\lambda| > 1$ we get an unstable focus. This indicates that there may be a Neimark–Sacker bifurcation at the fixed point when $|\lambda|$ passes through unity, which occurs when μ goes from $\mu \leq \mu_* := 1/(1 + C\Psi'(0)^2)$ to $\mu > \mu_*$.

If we hold μ constant we have,

$$C > \frac{1}{\Psi'(0)^2}\left[\frac{(1+\mu)^2}{4\mu} - 1\right], \tag{9.18}$$

and substituting this inequality into the eigenvalue (9.16) shows that the fixed points are always stable when the eigenvalues are real. When the eigenvalues are purely complex conjugates, the fixed points undergo Neimark–Sacker bifurcations, similar to the constant C case. The eigenvalue passes through unity when $C_* = (1/\mu - 1)/\Psi'(0)^2$.

These properties will be used to prove the results in Chapter 10.

9.2.3 Modified Gilet Model in an Annulus

In this section we modify Gilet's model to replicate behavior in an annulus in order to compare with experiments in Section 7.3. As we shall see in Chapter 10, Gilet's model becomes does not stay bounded in the chaotic regime. We endeavor to rectify this here and in Section 10.4.1.

Gilet's model was developed for a confined geometry, however when the system becomes chaotic the droplet has enough energy to escape this confinement since the confinement used is not physical. One way to rectify this would be to use a physically relevant confinement. Another way, which gives us a comparison with the experiments

in Section 7.3, is to glue the boundaries together. We accomplish this by transforming the model to the domain $[0, 2\pi]$ and identifying $x = 0$ and $x = 2\pi$. We also modify the eignemodes to be identified at the end points, where the function and its derivatives are equivalent. This modified model is

$$\begin{aligned} w_{n+1} =& \mu[w_n + \Psi(x_n)], \qquad x_{n+1} = [x_n - C w_n \Psi'(x_n)] \mod 2\pi; \\ \Psi(x, \beta) =& \frac{\cos\beta}{\sqrt{\pi}} \sin 3(x - \pi/2) + \frac{\sin\beta}{\sqrt{\pi}} \sin 5(x - \pi/2), \end{aligned} \tag{9.19}$$

where β is the shape parameter of the eigenmode test function.

The basic properties of the Gilet model seems to indicate that it is amenable to dynamical systems analysis. Furthermore, not only is it simple, it can be modified to compare with physical experiments.

CHAPTER 10

ANALYSIS AND SIMULATIONS: DISCRETE WALKING DROPLET MODELS

In this chapter we analyze Gilet's walking droplet model map via dynamical systems and bifurcation theory and formulate the conditions for it to have Neimark–Sacker (N–S) bifurcations (Section 10.1). In our analysis, we first vary μ while treating C as a constant, then vice versa, and find the values of μ and C for which the eigenvalues (9.16) have a modulus of unity and become complex conjugates. Then, we apply the genericity conditions for a N–S bifurcation to determine conditions on Ψ that make the system a generic 2-D map. Next, we apply our theorems for the conditions on the single eigenmode Ψ to the test functions that Gilet proposed (Section 10.2). While we use the same form of test functions, we also study test function shapes different from those studied in [49]. We end by noting a new global bifurcation that appears in our simulations (Section 10.3). Much of this work is presented in [135].

10.1 Neimark–Sacker Bifurcations

We consider the genericity conditions outlined in [81]. That is, the map must be locally conjugate near the fixed point to a specific normal form, there are no strong resonances, and the first Lyapunov coefficient must be nonzero. The Lyapunov coefficient also determines if the bifurcation is supercritical (if negative) or subcritical (if positive). While the N–S bifurcation is a local phenomenon about a single fixed point, it should be noted that all calculations apply to any fixed points, some of which will yield N–S bifurcations.

10.1.1 Neimark–Sacker Bifurcations with Respect to the Parameter μ

In [49], Gilet conjectured that a supercritical N–S bifurcation occurs at the fixed points (9.9). He also observed evidence of this in the iterates of the map for the chosen test functions. Here we prove that the map (9.8) is generic and a N–S bifurcation occurs at the fixed point as the parameter μ is varied by verifying the conditions of 1.1.1 (c.f. [81, 114, 144]). We also show the map allows for both supercritical and subcritical N–S bifurcations.

Theorem 10.1.1. *The map (9.8) is generic about some fixed point (w_*, x_*) if the eigenmode satisfies the following property,*

$$\begin{aligned}\hat{d} =&\Psi'''(x_*)\Psi'(x_*)(1+C\Psi'(x_*)^2)(1+2C\Psi'(x_*)^2)(4+3C\Psi'(x_*)^2)\\ &+2\Psi''(x_*)^2\left\{5+C\Psi'(x_*)^2\left[1-C\Psi'(x_*)^2\left(31+21C\Psi'(x_*)^2\right)\right]\right\}\neq 0.\end{aligned} \tag{10.1}$$

and a Neimark–Sacker bifurcation occurs at the fixed points (9.9) when

$$\mu=\mu_*=\frac{1}{1+C\Psi'(x_*)^2}. \tag{10.2}$$

Furthermore, if $\hat{d}<0$, the map undergoes a supercritical Neimark–Sacker bifurcation, whereas if $\hat{d}>0$, the map undergoes a subcritical Neimark–Sacker bifurcation in a neighborhood of the fixed point.

Proof. As done in Section 9.2.2, without loss of generality we translate the fixed point to $(w_*, x_*) = (0, 0)$. We showed in Section 9.2.2 that the pair of eigenvalues λ are complex conjugates if

$$\begin{aligned}&2C\Psi'(0)^2-2\sqrt{C\Psi'(0)^2(C\Psi'(0)^2+1)}+1\\ &\quad<\mu<2C\Psi'(0)^2+2\sqrt{C\Psi'(0)^2(C\Psi'(0)^2+1)}+1\end{aligned} \tag{10.3}$$

and $|\lambda| = 1$ when

$$\mu = \mu_* = \frac{1}{1 + C\Psi'(0)^2}.$$

This shows that a Neimark–Sacker bifurcation occurs at the fixed point if the map is generic.

Next we show the map is generic (c.f. [81, 114, 144]) via three conditions from Theorem 1.1.1; (C.1), (C.2), and (C.3):

(C.1) We show that $r'(\mu_*) \neq 0$, where $r = |\lambda| = \sqrt{\mu\,(1 + C\Psi'(0)^2)}$.

Notice, since $r(\mu_*) = 1$,

$$\frac{d}{d\mu}\left(r(\mu)^2\right)\Big|_{\mu=\mu_*} = 2r(\mu_*)r'(\mu_*) = 2r'(\mu_*),$$

so if $\frac{d}{d\mu}\left(r(\mu)^2\right)\Big|_{\mu=\mu_*} \neq 0$, $r'(\mu_*) \neq 0$. Then, since $C > 0$ and $\Psi'(0) \in \mathbb{R}$,

$$\frac{d}{d\mu}\left(r(\mu)^2\right)\Big|_{\mu=\mu_*} = (1 + C\Psi'(0)^2) \neq 0. \tag{10.4}$$

This shows that the transversality condition is satisfied.

(C.2) We show the arguments of the eigenvalues satisfy the first set of nondegeneracy conditions for a Neimark–Sacker bifurcation.

Let $\theta_* = \tan^{-1} A$, where

$$A = \frac{\sqrt{4\mu_*(1 + C\Psi'(0)^2) - (1 + \mu_*)^2}}{1 + \mu_*} = \frac{\sqrt{4 - (1 + \mu_*)^2}}{1 + \mu_*} \tag{10.5}$$

Observe that $\theta_* = 0$ if $A = 0$, $\theta_* = \pm\pi$ if $A = 0$, $\theta_* = \pm 2\pi/3$ if $A = \pm\sqrt{3}$, and $\theta_* \to \pm\pi/2$ as $A \to \pm\infty$. Since A is clearly positive and bounded, this rules out each case except $A = \sqrt{3}$. In order to get $\sqrt{3}$ we need $1 + \mu = 1$; however, since μ is positive, as shown in Section 9.2.2, this is not possible.

Thus the first nondegeneracy condition is satisfied.

(C.3) We compute the normal form for the Neimark–Sacker bifurcation and derive the conditions for which the second nondegeneracy condition is satisfied.

First, we compute the eigenvectors: $(DF)q = \lambda q$ and $(DF)^T p = \bar{\lambda} p$,

$$q = \begin{pmatrix} \mu_* \Psi'(0) \\ \lambda - \mu_* \end{pmatrix} \text{ and } p = \begin{pmatrix} \bar{\lambda} - 1 \\ \mu_* \Psi'(0) \end{pmatrix} \tag{10.6}$$

For the normalization, we take

$$\langle p, q \rangle = \bar{p} \cdot q = i\mu_* \Psi'(0) \sqrt{4 - (1 + \mu_*)^2}. \tag{10.7}$$

Now we change the variables to

$$\begin{pmatrix} w \\ x \end{pmatrix} = zq + \bar{z}\bar{q} = \begin{bmatrix} (z + \bar{z})\mu_* \Psi'(0) \\ (\lambda - \mu_*)z + (\bar{\lambda} - \mu_*)\bar{z} \end{bmatrix} \tag{10.8}$$

Substituting this into F yields

$$F = \begin{bmatrix} F_1 \\ F_2 \end{bmatrix}; \text{ where} \tag{10.9}$$

$$\begin{aligned} F_1 =& (z + \bar{z})\mu_*^2 \Psi'(0) + \mu_* \Psi((\lambda - \mu_*)z + (\bar{\lambda} - \mu_*)\bar{z}), \\ F_2 =& (\lambda - \mu_*)z + (\bar{\lambda} - \mu_*)\bar{z} - C(z + \bar{z})\mu_* \Psi'(0)\Psi'((\lambda - \mu_*)z + (\bar{\lambda} - \mu_*)\bar{z}). \end{aligned}$$

Now we take the inner product

$$\begin{aligned} \langle p, F \rangle =& (z + \bar{z})\mu_*^2(\lambda - 1)\Psi'(0) + \mu_*(\lambda - 1)\Psi((\lambda - \mu_*)z + (\bar{\lambda} - \mu_*)\bar{z}) \\ &+ (\lambda - \mu_*)\mu_* \Psi'(0)z + (\bar{\lambda} - \mu_*)\mu_* \Psi'(0)\bar{z} \\ &- C\mu_*^2 \Psi'(0)^2 (z + \bar{z})\Psi'((\lambda - \mu_*)z + (\bar{\lambda} - \mu_*)\bar{z}). \end{aligned} \tag{10.10}$$

Finally, to get the normal form we divide this through by $\langle p, q\rangle$ and take the Taylor series in $(z, \bar{z})$,

$$\begin{aligned} H = \Bigg[& (z+\bar{z})\mu_*^2(\lambda-1)\Psi'(0) + \mu_*(\lambda-1)\sum_{j+k\geq 1}\frac{1}{j!k!}\partial_{z^j\bar{z}^k}\Psi(0)z^j\bar{z}^k \\ & + (\lambda-\mu_*)\mu_*\Psi'(0)z + (\bar{\lambda}-\mu_*)\mu_*\Psi'(0)\bar{z} \\ & -C\mu_*^2\Psi'(0)^2(z+\bar{z})\left(\Psi'(0) + \sum_{j+k\geq 1}\frac{1}{j!k!}\partial_{z^j\bar{z}^k}\Psi'(0)z^j\bar{z}^k\right)\Bigg] \\ & \Big/ \left(i\mu_*\Psi'(0)\sqrt{4-(1+\mu_*)^2}\right), \end{aligned} \tag{10.11}$$

where $\partial_{z^j\bar{z}^k}\Psi(0) := \partial_{z^j\bar{z}^k}\Psi((\lambda-\mu_*)z + (\bar{\lambda}-\mu_*)\bar{z})|_{(z,\bar{z})=(0,0)}$, and similarly for $\partial_{z^j\bar{z}^k}\Psi'(0)$.

By matching the linear terms in (10.11), it is easy to show the normal form can be written as,

$$\begin{aligned} H = \lambda z + \Bigg[& (\lambda-1)\sum_{j+k\geq 2}\frac{1}{j!k!}\partial_{z^j\bar{z}^k}\Psi(0)z^j\bar{z}^k \\ & -C\mu_*\Psi'(0)^2(z+\bar{z})\sum_{j+k\geq 1}\frac{1}{j!k!}\partial_{z^j\bar{z}^k}\Psi'(0)z^j\bar{z}^k\Bigg] \\ & \Big/ \left(i\Psi'(0)\sqrt{4-(1+\mu_*)^2}\right). \end{aligned} \tag{10.12}$$

We are ready now to compute the nondegeneracy condition required to satisfy the final genericity condition. From [81, 144], we have the formula,

$$d(0) = \mathrm{Re}\left(\frac{\bar{\lambda}g_{21}}{2}\right) + \mathrm{Re}\left(\frac{\bar{\lambda}(\bar{\lambda}-2)}{2(\lambda-1)}g_{20}g_{11}\right) - \frac{1}{2}|g_{11}|^2 - \frac{1}{4}|g_{02}|^2. \tag{10.13}$$

where $g_{jk}/(j!k!)$ is the coefficient of the $z^j\bar{z}^k$ term. We compute the relevant terms

$$\begin{aligned}
g_{20} =& \frac{(\lambda-1)(\lambda-\mu_*)^2\Psi''(0) - 2C\mu_*\Psi'(0)^2(\lambda-\mu_*)\Psi'(0)}{i\sqrt{4-(1+\mu_*)^2}\Psi'(0)} \\
g_{02} =& \frac{(\lambda-1)(\bar{\lambda}-\mu_*)^2\Psi''(0) - 2C\mu_*\Psi'(0)^2(\bar{\lambda}-\mu_*)\Psi'(0)}{i\sqrt{4-(1+\mu_*)^2}\Psi'(0)} \\
g_{11} =& \frac{(\lambda-1)(\lambda-\mu_*)(\bar{\lambda}-\mu_*)\Psi''(0)}{i\sqrt{4-(1+\mu_*)^2}\Psi'(0)} - \frac{C\mu_*\Psi'(0)^2(\lambda-\mu_*+\bar{\lambda}-\mu_*)\Psi'(0)}{i\sqrt{4-(1+\mu_*)^2}\Psi'(0)} \\
g_{21} =& \frac{(\lambda-1)(\lambda-\mu_*)^2(\bar{\lambda}-\mu_*)\Psi'''(0)}{i\sqrt{4-(1+\mu_*)^2}\Psi'(0)} \\
& - \frac{C\mu_*\Psi'(0)^2((\lambda-\mu_*)^2+2(\lambda-\mu_*)(\bar{\lambda}-\mu_*))\Psi'''(0)}{i\sqrt{4-(1+\mu_*)^2}\Psi'(0)}
\end{aligned}$$

If we factor out certain terms this formula greatly simplifies to

$$\begin{aligned}
d(0) =& \frac{\Psi'''(0)}{2\Psi'(0)}\frac{\mathrm{Re}(-i\bar{\lambda}\hat{g}_{21})}{\sqrt{4-(1+\mu_*)^2}} - \frac{\Psi''(0)^2}{\Psi'(0)^2}\frac{\mathrm{Re}\left(\frac{\bar{\lambda}(\bar{\lambda}-2)}{2(\lambda-1)}\hat{g}_{20}\hat{g}_{11}\right)}{(4-(1+\mu_*)^2)} \\
& - \frac{\Psi''(0)^2}{\Psi'(0)^2}\frac{\frac{1}{2}|\hat{g}_{11}|^2+\frac{1}{4}|\hat{g}_{02}|^2}{(4-(1+\mu_*)^2)},
\end{aligned} \tag{10.14}$$

where

$$\hat{g}_{20} = (\lambda-\mu_*)\left[\lambda^2+\mu_*-2C\Psi'(0)^2\mu_*-\lambda(1+\mu_*)\right] \tag{10.15}$$

$$\hat{g}_{02} = (\bar{\lambda}-\mu_*)\left[1+\mu_*-2C\Psi'(0)^2\mu_*-\lambda\mu_*-\bar{\lambda}\right] \tag{10.16}$$

$$\begin{aligned}
\hat{g}_{11} = -1+\lambda+&\lambda\mu_* - C\Psi'(0)^2\lambda\mu_* - \lambda^2\mu_* + \lambda\mu_* - C\Psi'(0)^2\bar{\lambda}\mu_* \\
& - \mu_* - \mu_*^2 + 2C\Psi'(0)^2\mu_*^2 + \lambda\mu_*^2
\end{aligned} \tag{10.17}$$

$$\begin{aligned}
\hat{g}_{21} = (\mu_*-\lambda)\big[&1-\lambda-\lambda\mu_*+C\Psi'(0)^2\lambda\mu_*+\lambda^2\mu_*-\bar{\lambda}\mu_* \\
&+2C\Psi'(0)^2\bar{\lambda}\mu_*+\mu_*+\mu_*^2-3C\Psi'(0)^2\mu_*^2-\lambda\mu_*^2\big].
\end{aligned} \tag{10.18}$$

Then, substituting in for λ and μ_* gives

$$d(0) = C^2\Psi'(0)^2\Big[\Psi'''(0)\Psi'(0)(1+C\Psi'(0)^2)(1+2C\Psi'(0)^2)(4+3C\Psi'(0)^2) + 2\Psi''(0)^2\left\{5+C\Psi'(0)^2\left[1C\Psi'(0)^2\left(31+21C\Psi'(0)^2\right)\right]\right\}\Big] \Big/ \left[4(1+C\Psi'(0)^2)^4(4+3C\Psi'(0)^2)\right]. \tag{10.19}$$

Since

$$\frac{C^2\Psi'(0)^2}{4(1+C\Psi'(0)^2)^4(4+3C\Psi'(0)^2)} > 0,$$

we need only be concerned with

$$\hat{d} := \Psi'''(x_*)\Psi'(x_*)(1+C\Psi'(x_*)^2)(1+2C\Psi'(x_*)^2)(4+3C\Psi'(x_*)^2) + 2\Psi''(x_*)^2\left\{5+C\Psi'(x_*)^2\left[1-C\Psi'(x_*)^2\left(31+21C\Psi'(x_*)^2\right)\right]\right\} \tag{10.20}$$

Consequently, the Neimark–Sacker criteria imply that the bifurcation occurs if $\hat{d} \neq 0$, and it is supercritical for $\hat{d} < 0$ and subcritical for $\hat{d} > 0$.

This shows that if Ψ has certain properties then the second nondegeneracy condition is satisfied, thereby completing the proof.

□

10.1.2 Neimark–Sacker Bifurcations with Respect to the Parameter C

In this section we prove the map (9.8) is generic and a Neimark–Sacker bifurcation occurs as we vary the parameter C at the fixed point.

Corollary 10.1.1. *The map (9.8) is generic about some fixed point (w_*, x_*) if the eigenmode satisfies the following property,*

$$\hat{d} = \Psi'(x_*)\Psi'''(x_*)\left(6 - \mu - \mu^2\right) + 2\Psi''(x_*)^2\left(32\mu - 6\mu^3 - 21\right) \neq 0. \tag{10.21}$$

and a Neimark–Sacker bifurcation occurs at the fixed points (9.9) when

$$C = C_* = \frac{1}{\Psi'(x_*)^2}\left(\frac{1}{\mu} - 1\right). \tag{10.22}$$

Furthermore, if $\hat{d} < 0$, the map undergoes a supercritical Neimark–Sacker bifurcation, and if $\hat{d} > 0$, the map undergoes a subcritical Neimark–Sacker bifurcation in a neighborhood of the fixed point.

Proof. As done in Section 9.2.2, without loss of generality we translate the fixed point to $(w_*, x_*) = (0, 0)$. We showed in Section 9.2.2 that the pair of eigenvalues λ are complex conjugates if

$$C > \frac{1}{\Psi'(0)^2}\left[\frac{(1+\mu)^2}{4\mu} - 1\right], \tag{10.23}$$

and $|\lambda| = 1$ when

$$C = C_* = \frac{1}{\Psi'(0)^2}\left(\frac{1}{\mu} - 1\right).$$

This shows that a Neimark–Sacker bifurcation occurs at the fixed point if the map is generic.

Most of the arguments for genericity follow directly from the proof of Theorem 10.1.1. For the first condition we use the same r and study $r(C)$. Just as with $r(\mu)$, it suffices to study $r(C)^2$. Then,

$$\frac{d}{dC}\left(r(C)^2\right)\Big|_{C=C_*} = \mu\Psi'(0)^2 \neq 0 \text{ if } \Psi'(0) \neq 0. \tag{10.24}$$

Hence, if $\Psi'(0) \neq 0$, the map satisfies the transversality condition.

The argument to show no strong resonances is the same as that of Theorem 10.1.1.

For the first Lyapunov coefficient, the calculations are the same up to (10.18), by replacing C with C_* and μ_* with μ. Then, substituting in for λ and C_* gives

$$d(0) = \frac{(\mu-1)^2}{4\Psi'(0)^2(3+\mu)}\big[\Psi'(x_*)\Psi'''(x_*)\left(6-\mu-\mu^2\right) + 2\Psi''(x_*)^2\left(32\mu-6\mu^3-21\right)\big]. \tag{10.25}$$

Since

$$\frac{(\mu-1)^2}{4\Psi'(0)^2(3+\mu)} > 0$$

we need only be concerned with

$$\hat{d} := \Psi'(x_*)\Psi'''(x_*)\left(6-\mu-\mu^2\right) + 2\Psi''(x_*)^2\left(32\mu-6\mu^3-21\right) \tag{10.26}$$

Consequently, the Neimark–Sacker criteria imply that the bifurcation occurs if $\hat{d} \neq 0$, and it is supercritical for $\hat{d} < 0$ and subcritical for $\hat{d} > 0$.

This shows that for certain properties of Ψ the genericity conditions are satisfied, thereby completing the proof.

□

10.2 Application of the Mathematical Results to Sample Test Functions

In [49], Gilet uses the test functions,

$$\Psi(x,\beta) = \frac{1}{\sqrt{\pi}}\cos\beta\sin 3x + \frac{1}{\sqrt{\pi}}\sin\beta\sin 5x \tag{10.27}$$

where $\beta \in [0,\pi]$ is a fixed parameter that can be changed in order to tweak the shape of the eigenmode. He shows numerical constructions of the iterate-space for $\beta = \pi/3$

and $\beta = \pi/6$, and studies the statistics of the iterates for other values of β, all the while holding $C = 0.05$. We first follow in a similar manner and hold $C = 0.05$ and vary μ, then we hold $\mu = 0.5$ and vary C.

To illustrate how small the parameter regime for a subcritical Neimark–Sacker bifurcation is, let us consider $\hat{d}$ for the origin, since it is always a fixed point. We plot over $\beta \in [0, \pi]$, first for μ_* (i.e., holding $C = 0.05$), then for C_* (i.e., holding $\mu = 0.5$). This is shown in Figure 10.1.

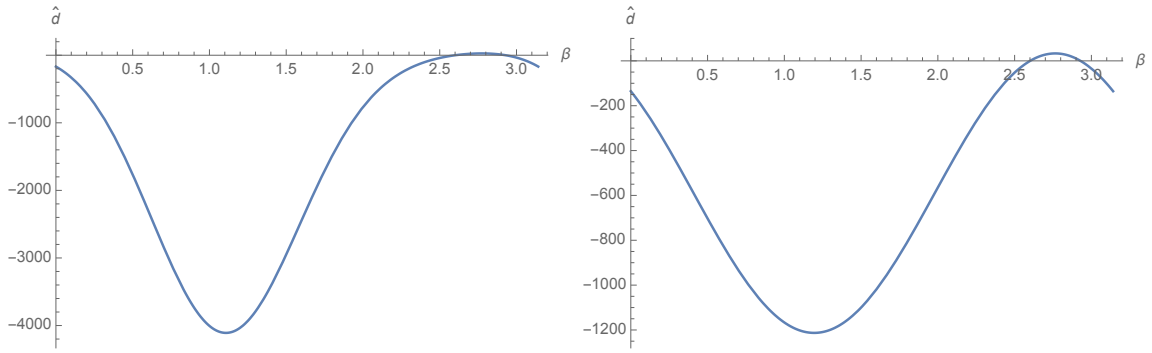

(a) $\mu = \mu_*$, $C = 0.05$, $(x_*, w_*) = (0, 0)$ (b) $\mu = 0.5$, $C = C_*$, $(x_*, w_*) = (0, 0)$

Figure 10.1 Plots of first Lyapunov exponent for Neimark–Sacker bifurcations in μ and C.

Source: A. Rahman and D. Blackmore. Neimark–Sacker bifurcations and evidence of chaos in a discrete dynamical model of walkers. *Chaos, Solitons & Fractals*, 91: 339-349, 2016.

10.2.1 Simulations of Neimark–Sacker Bifurcations in μ

As in [49], we first study the eigenmode for $\beta = \pi/3$, for which the map exhibits supercritical Neimark–Sacker bifurcations at various fixed points, but we also study $\beta = 5\pi/6$, for which the map exhibits a subcritical Neimark–Sacker bifurcation at the origin. We hold $C = 0.05$, which corresponds to a droplet much smaller than the

cavity being created by an impact, and we vary μ, which corresponds to the system approaching high memory.

It should be noted that for the sake of plotting, we consider the map (9.8) to be written as

$$\begin{bmatrix} x_{n+1} \\ w_{n+1} \end{bmatrix} = F(x_n, w_n) = \begin{bmatrix} x_n - Cw_n\Psi'(x_n) \\ \mu[w_n + \Psi(x_n)] \end{bmatrix} \tag{10.28}$$

Supercritical Neimark–Sacker Bifurcations for $\beta = \pi/3$. For $\beta = \pi/3$, we now consider the map (10.28) on the domain $x \in [0, \pi/2]$. On this domain the map has three fixed points $(x_*, 0)$, which occur at roots of Ψ, that undergo Neimark–Sacker bifurcations; one is at the origin. The other two are:

$$x_* = \tan^{-1}\left(\sqrt{\frac{15 + \sqrt{3} - \sqrt{6(8-\sqrt{3})}}{9 - \sqrt{3} + \sqrt{6(8-\sqrt{3})}}}\right) \approx 0.7269$$

$$x_* = \tan^{-1}\left(\sqrt{\frac{15 + \sqrt{3} + \sqrt{6(8-\sqrt{3})}}{9 - \sqrt{3} - \sqrt{6(8-\sqrt{3})}}}\right) \approx 1.3515$$

At the fixed points a supercritical Neimark–Sacker bifurcation occurs for $\mu_* = 0.64894,\ 0.742027,\ 0.879451$, respectively, for which $\hat{d} = -4076.61,\ -1747.52,\ -410.779$. The map (10.28) has three other fixed points: $(\approx 0.3490, \approx \frac{\mu}{1-\mu}\Psi(0.3490))$, $(\approx 1.0128, \approx \frac{\mu}{1-\mu}\Psi(1.0128))$, $(\pi/2, \frac{\mu}{1-\mu}\Psi(\pi/2))$, which are saddles (the w position varying with μ) and therefore not subject to Neimark–Sacker bifurcations. Let us vary the parameter μ from $\mu = 0.5$ to $\mu = 0.89$. We illustrate the progression of the bifurcations in Figure 10.2. In Figure 10.2a, the relevant fixed points are all stable foci. Next, in Figure 10.2b, we have passed the critical value for the origin and a stable invariant circle is now visible. Finally, in Figure 10.2c and 10.2d, the critical values for the next two fixed points, respectively, are passed. We notice in Figure 10.2c

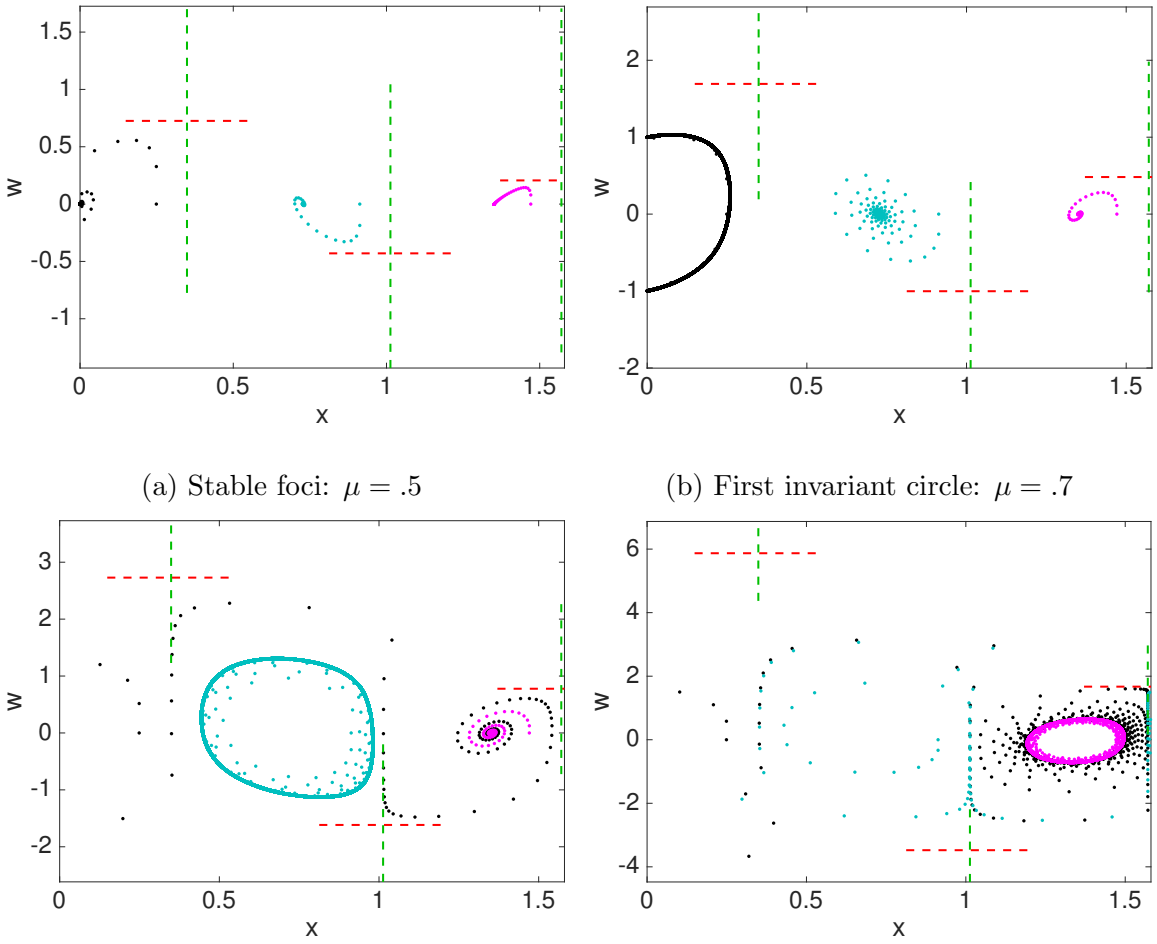

(a) Stable foci: $\mu = .5$

(b) First invariant circle: $\mu = .7$

(c) Second invariant circle: $\mu = .79$

(d) Third invariant circle: $\mu = .89$

Figure 10.2 For each plot the green lines represent the linear stable manifold and the red lines represent the linear unstable manifold at the respective saddle fixed points. The **black** markers represent iterates originating from a neighborhood of the **origin**, the cyan markers represent iterates originating from a neighborhood of $(\approx .7269, 0)$, and the magenta markers represent the iterates originating from a neighborhood of $(\approx 1.3515, 0)$.

Source: A. Rahman and D. Blackmore. Neimark–Sacker bifurcations and evidence of chaos in a discrete dynamical model of walkers. *Chaos, Solitons & Fractals*, 91: 339-349, 2016.

and 10.2d that the preceding fixed point(s), respectively, are now unstable focus(foci). This shows that each fixed point undergoes a supercritical Neimark–Sacker bifurcation in accordance with Theorem 10.1.1. It should be noted that since the test functions are periodic, on the entire domain of $x \in \mathbb{R}$, Neimark–Sacker bifurcations occur at (countably) infinitely many fixed points with the final bifurcation occurring for fixed points corresponding to $x_* \approx 1.3515$.

Physically, the droplet about any fixed point is initially (Figure 10.2a) oscillating with decaying radius. Then, due to the nature of the single eigenmode used by Gilet, the droplet corresponding to a position near the origin will undergo a N–S bifurcation (Figure 10.2b). This corresponds to the droplet oscillating about the origin with a fixed radius. Then as μ is varied further, the invariant circle about the origin disintegrates and it becomes unstable, which corresponds to the orbit of the droplet increasing radially until it reaches the neighborhood of one of the neighboring fixed points. Now, since a N–S bifurcation has already occurred at the next fixed point (Figure 10.2c), the iterates will bypass this region and converge to the following fixed point, which corresponds to the droplet jumping to an orbit around a different center. Similar behavior occurs at every other N–S fixed point.

In addition to Neimark–Sacker bifurcations, we notice a curious phenomenon. As the saddle fixed points move away from the Neimark–Sacker fixed points the trajectories from the neighborhood of one Neimark–Sacker fixed point crosses into that of another. Furthermore, as the invariant circle increases in radius it seems to collide (more precisely, gets arbitrarily close) with a stable manifold of one of its neighboring saddles just before the onset of chaos. We shall analyze this further in Section 10.3.

Subrcritical Neimark–Sacker Bifurcations for $\beta = 5\pi/6$. For $\beta = 5\pi/6$ let us once again consider the map (10.28), however let us simplify matters and restrict our domain to a neighborhood of the origin. Here lies a subcritical Neimark-Sacker bifurcation at $\mu_* = 0.999847$ where $\hat{d} = 4.88756$. Since this is subcritical, let us vary our parameter μ backwards from $\mu = 0.9999$ to $\mu = .999$. This is illustrated in Figure 10.3. First the origin is an unstable focus, then as μ passes μ_* backwards the origin becomes a stable focus, however if an initial point is taken further out the iterates diverge, which indicates an unstable invariant circle. In Figure 10.3b, we represent this unstable invariant circle by the black dashed curve.

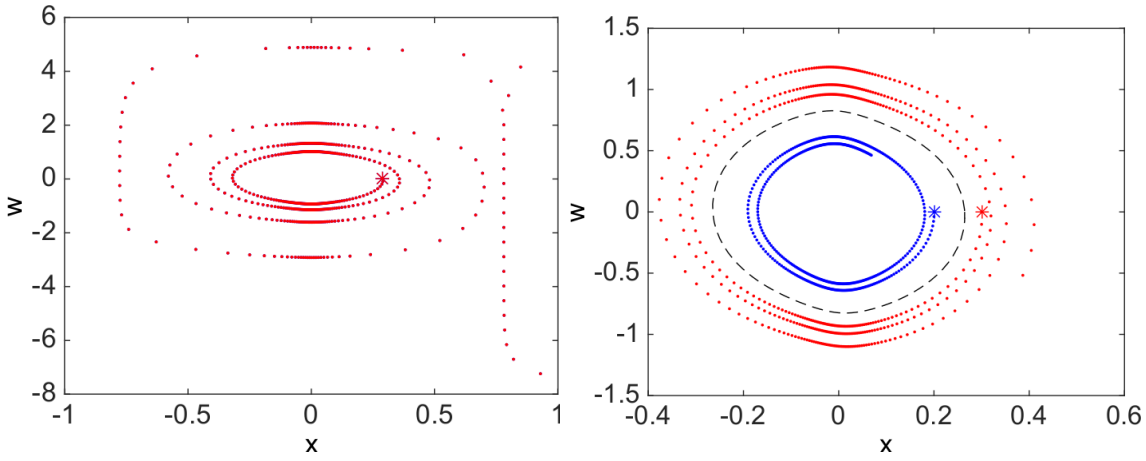

(a) Unstable focus: $\mu = 0.9999$ (b) Unstable invariant circle: $\mu = 0.999$

Figure 10.3 A star denotes the initial point. In the second plot the blue iterates have an initial point inside the invariant circle, and the red iterates have an initial point outside the invariant circle. Finally, the black dashed curve represents the unstable invariant circle.

Source: A. Rahman and D. Blackmore. Neimark–Sacker bifurcations and evidence of chaos in a discrete dynamical model of walkers. *Chaos, Solitons & Fractals*, 91: 339-349, 2016.

While from a dynamical systems perspective, we vary the parameter backward for a subcritical bifurcation, this would be cumbersome in a physical experiment.

Rather let us begin at Figure 10.3b, where a droplet close enough to the origin would oscillate with a decaying radius, however if the droplet were exactly on the unstable invariant circle it would remain at that constant radius, and if the droplet were slightly further out it would oscillate with a growing radius and escape the neighborhood of the origin. Now as we increase the memory the invariant circle shrinks until the critical parameter value $\mu_* = 0.999847$, when it ceases to exist and the origin becomes unstable, which corresponds to the droplet anywhere near the origin oscillating with increasing radius. It should be noted that the growth of the radius is not indefinite, and at some point it may be drawn to another fixed point or invariant circle, which is usually the case.

10.2.2 Simulations of Neimark–Sacker Bifurcations in C

Varying C produces exotic trajectories, of which we present one such example in this section, holding $\mu = 0.5$ and $\beta = \pi/3$. Consider two fixed points, $(x_*, 0)$ such that

$$x_* = -\tan^{-1}\left(\sqrt{\frac{15+\sqrt{3}+\sqrt{6(8-\sqrt{3})}}{9-\sqrt{3}-\sqrt{6(8-\sqrt{3})}}}\right) \approx -1.3515,$$

$$x_* = -\pi + \tan^{-1}\left(\sqrt{\frac{15+\sqrt{3}-\sqrt{6(8-\sqrt{3})}}{9-\sqrt{3}+\sqrt{6(8-\sqrt{3})}}}\right) \approx -1.7901.$$

At these fixed points a supercritical Neimark–Sacker bifurcations occurs simultaneously due to the symmetry for $C_* = 0.36477$, where $\hat{d} = -578.487$. The other fixed point is $(-\pi/2, \Psi(-\pi/2))$, which is a saddle.

For this case, increasing C corresponds to the drop size increasing, which leads to greater inertia. With increased inertia, the distance the droplet travels due to an impact is greater, and hence sensitive dependence may come into play. First, the N–S bifurcation is illustrated in Figure 10.4. Here the physical interpretation of the

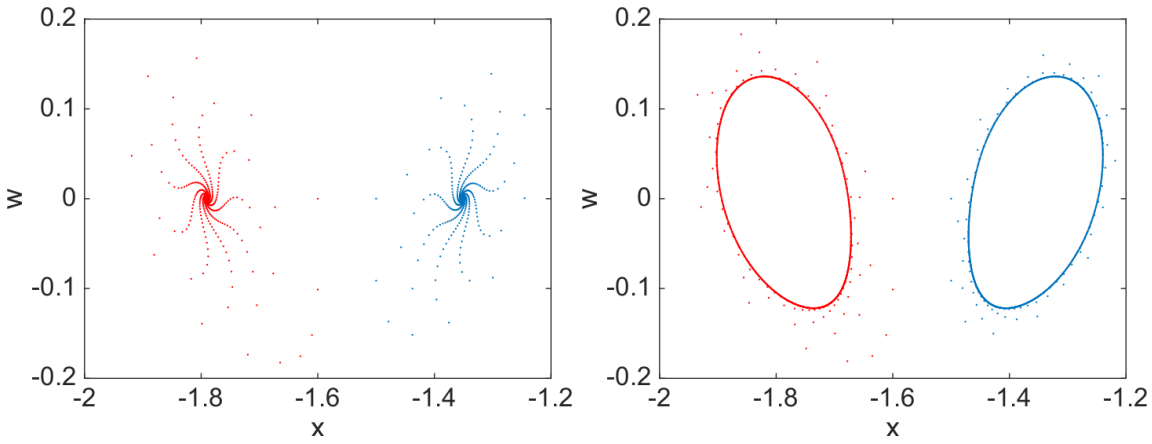

(a) Stable foci: $C = 0.35$ (b) Stable invariant circle: $C = 0.4$

Figure 10.4 The red trajectories start on the left of the saddle blue trajectories start on the right of the saddle (not shown).

Source: A. Rahman and D. Blackmore. Neimark–Sacker bifurcations and evidence of chaos in a discrete dynamical model of walkers. *Chaos, Solitons & Fractals*, 91: 339-349, 2016.

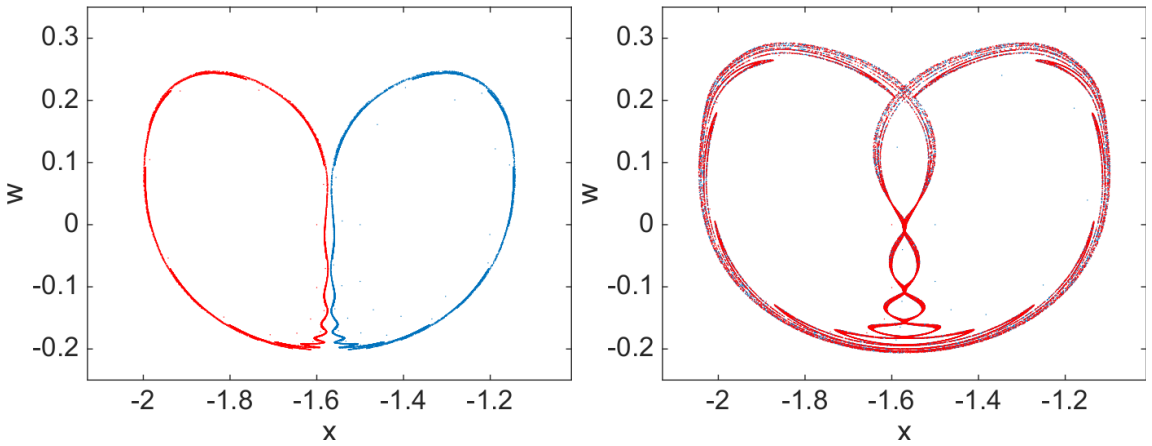

(a) Deformed invariant circles: $C = 0.5$ (b) Evidence of global bifurcation: $C = 0.6$

Figure 10.5 The red trajectories start on the left of the saddle blue trajectories start on the right of the saddle (not shown).

Source: A. Rahman and D. Blackmore. Neimark–Sacker bifurcations and evidence of chaos in a discrete dynamical model of walkers. *Chaos, Solitons & Fractals*, 91: 339-349, 2016.

bifurcation is the same as in Section 10.2.1, the only difference being the change in the size of the droplet as opposed to changes in memory.

Now, as we increase C, we obtain the exotic trajectories as illustrated in Figure 10.5. We observe the characteristic stretching and folding of chaotic dynamics, which may lead to fractal structures. The way in which the invariant circles approach the stable manifold that separates them shows evidence of what appears to be an unusual and possibly new type of global bifurcation, which is briefly discussed in the next section.

10.3 Global Bifurcations Leading to Chaos

In Figure 10.2d we observe evidence of nontrivial topological structures. If we continue to vary μ, we find more complex, chaotic-like, dynamics. We illustrate this in Figure 10.6, where we see a scatter of iterates in a manner indicative of chaos. Moreover, we observe that μ is varied, the iterates remain within a compact set. Here the iterates seem to satisfy the transitivity and sensitivity conditions for chaos. So far, all we have are simulations and informed intuition: further investigation is clearly required in order to obtain a more precise characterization these dynamical properties.

Now let us vary μ near the onset of chaos to study the bifurcation. This is illustrated in Figure 10.7. First (Figure 10.7a) we observe the invariant circles for $\mu = 0.913$ as before, then at $\mu = 0.914$ the invariant circles start to disintegrate (Figure 10.7b). Finally, in Figure 10.7c, for $\mu = 0.915$ we see the iterates bouncing between the neighborhoods of their respective Neimark–Sacker fixed point and perhaps nested invariant circles (both stable and unstable). This provides evidence of a new bifurcation as the invariant circle approaches the stable manifold of the saddle and perhaps even a cascading Neimark–Sacker doubling bifurcations, which is an infinite

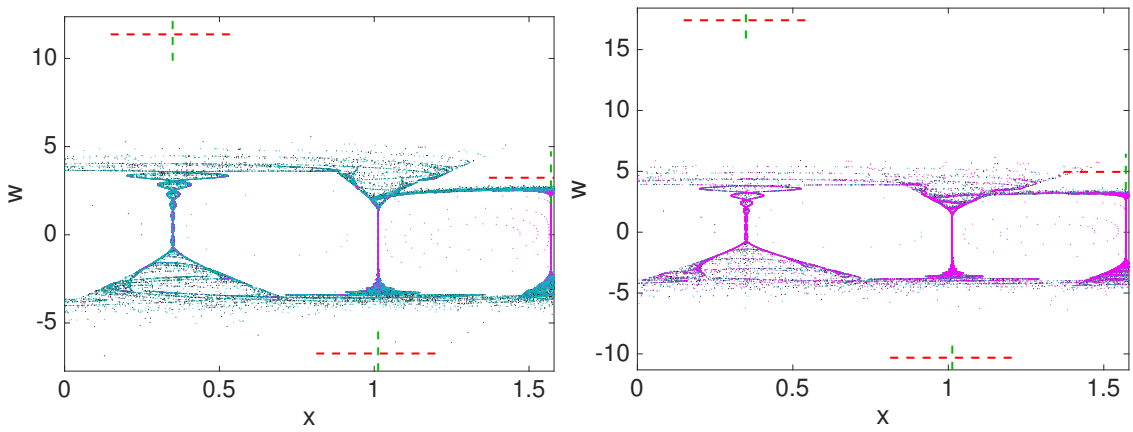

(a) Evidence of chaos: $\mu = 0.94$

(b) Evidence of chaos: $\mu = 0.96$

Figure 10.6 Seemingly chaotic trajectories. For each plot the green lines represent the linear stable manifold and the red lines represent the linear unstable manifold at the respective saddle fixed points. The **black** markers represent iterates originating from a neighborhood of the **origin**, the cyan markers represent iterates originating from a neighborhood of $(\approx .7269, 0)$, and the magenta markers represent the iterates originating from a neighborhood of $(\approx 1.3515, 0)$.

Source: A. Rahman and D. Blackmore. Neimark–Sacker bifurcations and evidence of chaos in a discrete dynamical model of walkers. *Chaos, Solitons & Fractals*, 91: 339-349, 2016.

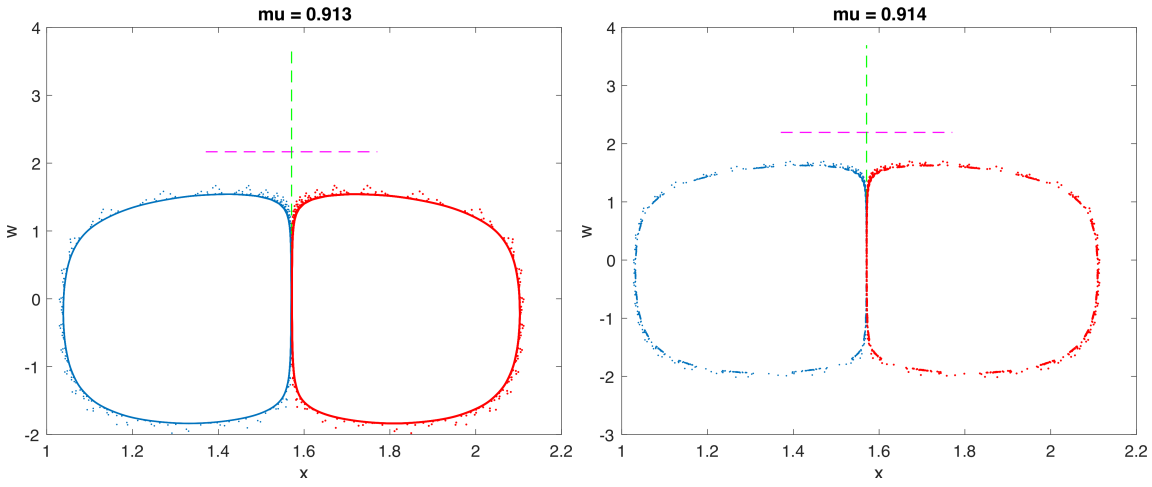

(a) Invariant circle: $\mu = 0.913$ (b) Invariant circle disintegrating: $\mu = 0.914$

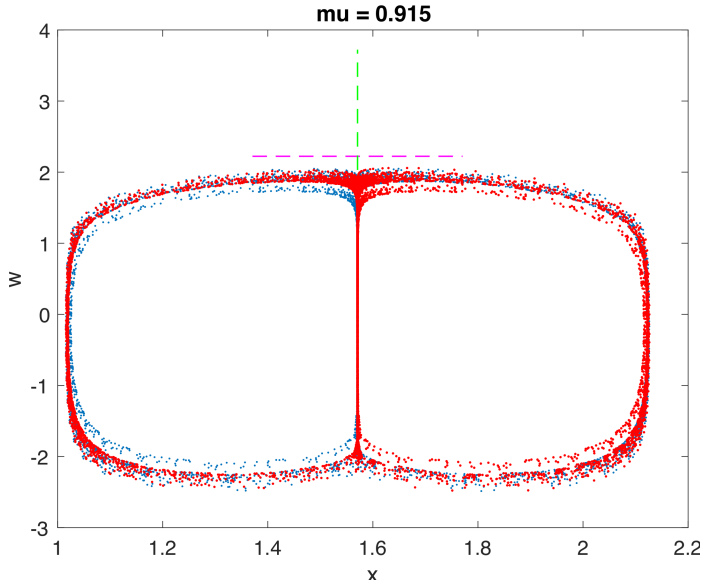

(c) Iterates after collision: $\mu = 0.915$

Figure 10.7 The green lines represent the linear stable manifold and the magenta lines represent the linear unstable manifold at the respective saddle fixed points. The blue markers represent iterates originating from the left of the saddle and the red markers represent iterates originating from the right of the saddle.

Source: A. Rahman and D. Blackmore. Neimark–Sacker bifurcations and evidence of chaos in a discrete dynamical model of walkers. *Chaos, Solitons & Fractals*, 91: 339-349, 2016.

succession of stability changes of invariant circles that create new pairs of invariant circles (see, e.g., [9], where they are called cascading Hopf doubling bifurcations).

Furthermore, we notice in our figures that iterates tend to intersect the linear stable manifolds. If we do not restrict the region of the plot, we observe that the iterates seem to prefer certain positions as shown in Figure 10.8. In [49], Gilet gives a detailed study of the statistics associated with the positions of the iterates and in the simulations he observes a probability density function inversely proportional to $|\Psi'(x)|$. While we do not study the statistics, we observe that the linear stable manifolds pass through the roots of $\Psi'(x)$, which hints at connections between the dynamical systems aspects and statistical analysis of this model.

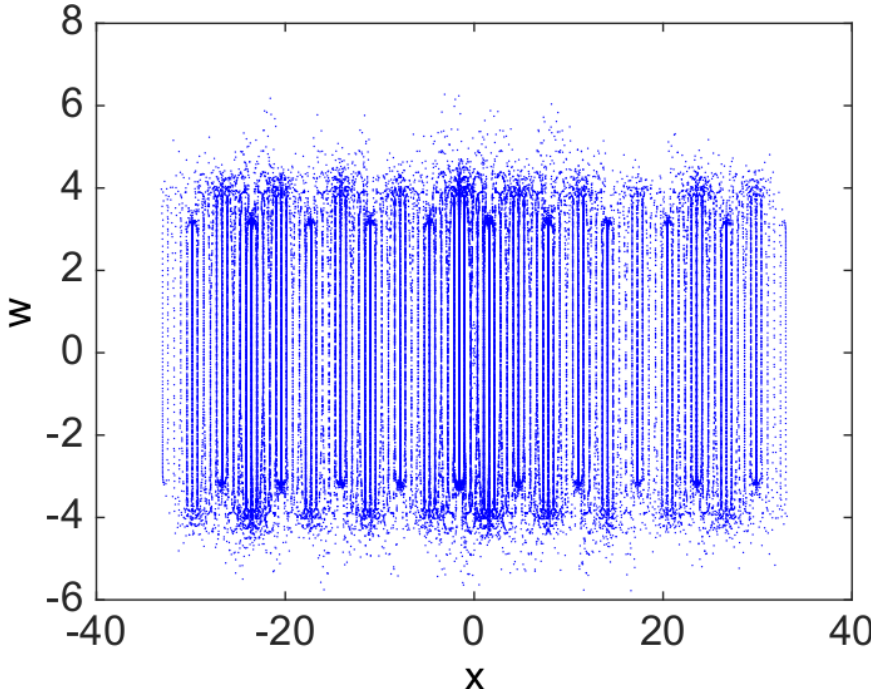

Figure 10.8 Iterates of the map (10.28) generated from four initial points chosen near the origin.

Source: A. Rahman and D. Blackmore. Neimark–Sacker bifurcations and evidence of chaos in a discrete dynamical model of walkers. *Chaos, Solitons & Fractals*, 91: 339-349, 2016.

10.4 Other Interesting Results

In this section we briefly discuss dynamics that have not yet been studied rigorously, but may reveal insight about the behavior of walkers and drawbacks of current discrete dynamical models.

10.4.1 Dynamics in an Annulus

In Section 9.2.3 we derived a model, based on Gilet's model, of a walker in an annulus. This leads to more physically relevant statistics than the walker in free space. While the statistics are different, the analysis in the previous sections are robust enough to be applied to this model as well, which shall be useful for future investigations. The iterate space and histogram are shown in Figure 10.9.

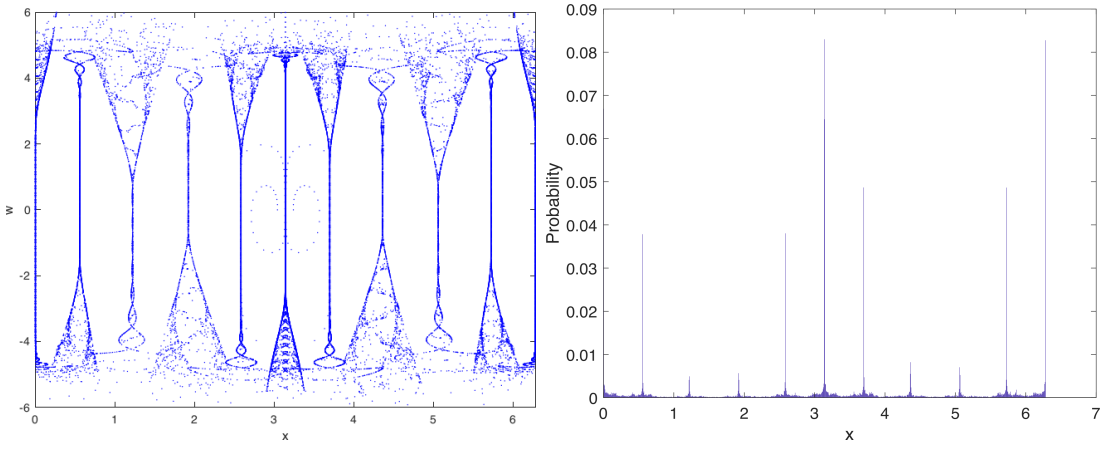

(a) Iterates of (9.19). (b) Histogram of (9.19).

Figure 10.9 Plot of the iterates and statistics of a walker in an annular geometry.

10.4.2 Crisis Bifurcations after Chaos

Crisis bifurcations, also called *crises*, occur when a chaotic strange attractor experiences a sudden topological change as a parameter is varied [50]. While this is difficult to characterize in most systems, we can visualize these topological changes

through numerical studies. We return to Gilet's original model and discover these bifurcations well after the onset of chaos, but below the Faraday threshold. In Figure 10.10 we show such an evolution of the chaotic attractor.

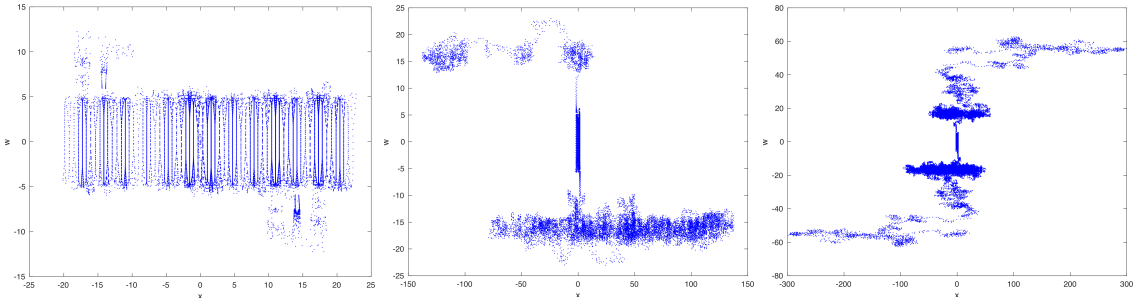

(a) $\mu = 0.99$. (b) $\mu = 0.999$. (c) $\mu = 0.9999$.

Figure 10.10 Evolution of a chaotic attractor undergoing a series of crisis bifurcations.

10.5 Conclusions

Previous investigations of the walking phenomena have shown evidence of exotic dynamics, such as Hopf bifurcations and chaos, mainly through experiments and numerical simulations. However, the equations have generally been too complex to prove the existence of certain bifurcations, chaos, and other topological properties. In recent years, discrete models have been studied by Fort *et al.* [48], Eddi *et al.* [42], Shirokoff [146], and Gilet [49]. The models of Shirokoff [146] and Gilet [49] are discrete dynamical systems, which are often more accessible to rigorous analysis. In this thesis we proved some of the properties observed and conjectured for Gilet's model; namely, the existence of N–S bifurcations. Similar dynamical systems analysis is likely in future to prove additional results concerning bifurcations, chaos, structural stability, and other properties. Proving these properties is not only important mathematically,

but may also provide insight into the phenomena observed for walkers and for their continuous models.

We proved Gilet's conjecture [49] about the existence of supercritical N–S bifurcations when varying the parameter μ. In doing so, we are also able to prove the existence of subcritical N–S bifurcations in the parameter μ, which had been missed by the original simulations. We then varied the parameter C, which had not been studied before, and proved the existence of N–S bifurcations there as well.

In order to verify the validity of our theory, the model was simulated using test functions for Ψ. For the sake of consistency the test functions used were of the same form as [49], but the shapes were changed by varying β. By doing so we were able to analyze the transition between supercritical and subcritical N–S bifurcations (Figure 10.1) for both μ and C. We reproduced one of the simulations from [49] in order to show consistency between the two studies. Then we ran additional simulations of the various cases in our theorems, all of which demonstrate complete agreement between our mathematical results and the numerics.

Finally, we observed evidence of more exotic dynamics, which seem to lead to chaos. One such curious phenomenon is a new global bifurcation when the invariant circles get ever closer to the stable manifold of a neighboring saddle fixed point. We originally believed the path to chaos was through cascading N–S bifurcations wherein the invariant circles change stability and give birth to twin stable invariant circles. However, it now seems as though the actual route is far more complex.

CHAPTER 11

CONCLUDING DISCUSSIONS

In this chapter we summarize the discussions in the previous chapters. We first encapsulate the contents for chaotic logical circuits and walking droplets. Finally we outline future work and the current direction of the fields.

11.1 Chaotic Logical Circuits

The main mathematical motivation for this work was to study the dynamics of logical circuits implemented using nonlinear elements. These nonlinear elements can either serve as analogs of nonlinearities in natural logical systems or can be exploited for the purposes of communication. As the circuits get more complicated the number of experiments and mathematical models drops precipitously. This work endeavored to create a modeling framework for nonlinear gates and flip-flops. First we presented previous work on simple gates and flip-flops creating an intuition about the common dynamics of such circuits. Then this thesis outlined our experimental investigations on a dual NOR gate/RSFF circuit. This system was chosen due to the dual gate–flip-flop functionality, which can then be used to construct an entire logic family. Finally we arrived at the main results of this work: modeling and analyzing the circuits.

With respect to modeling, we first presented a naïve approach that does not incorporate the physics of the circuits, but rather relies on previous investigations of similar circuits and reproduces behavior observed in Poincaré maps of continuous models from these investigations. This was done by noticing that both threshold control units have precisely the same edge-trigger mechanism of the final output; in-fact for one threshold this is a negation and for the other it is a flip of the sign in

the voltage. However, this does not explain the occurrence of chaos. We employed C^0 perturbations that mimic the type of perturbations observed in physical realizations, which then produced behavior qualitatively similar to that of approximate Poincaré maps of similar circuits. Doing so creates interesting mathematical results, but the physical connections were unsatisfactory, which necessitated mechanistic models.

Next we presented a mechanistic modeling framework capable of modeling any system using similar thresholding mechanisms. We modeled the circuits with the intention of matching our experiments quantitatively for non-chaotic regimes and qualitatively for chaotic regimes. This was accomplished by making continuous extensions of the binary behavior and inserting chaotic drivers represented as tent-like maps. Tent-like maps were used since the threshold control units replicate tent-like behavior for non-chaotic inputs. This model was shown to be chaotic through modern dynamical systems techniques. Finally, we compared the theoretical results to our experimental investigation. In addition, we developed stochastic models to rectify small discrepancies during the edge trigger, which qualitatively matches the behavior observed in physical realizations.

11.2 Walking Droplets

As in the previous section, the main mathematical motivation was to study the dynamical behavior of walking droplets near the onset of chaos. From a physical point of view, chaos is important because it leads to seemingly random behavior, which can then be used to show analogies between the fluidic system and traditional wave-particle systems. This work endeavored to illustrate the paths to chaos and the connections between the dynamics and the statistical behavior observed in experiments. First, the seminal experiments on walking droplets were presented to develop an intuition for the

physical problem. Then we discussed traditional hydrodynamic modeling techniques leading to integro-differential models. While these models match the experiments extremely well, they can be quite difficult to analyze. In order to facilitate dynamical systems analysis simpler models were necessary. These came in the form of discrete dynamical systems.

This work analyzed one discrete dynamical model in depth. The model is derived for a walker in a straight line for which the droplet moves a distance proportional to the gradient of the wave-field. Furthermore, since the droplet is moving in a straight line, it is assumed that only one eigenmode is excited at each bounce. For this model we proved the existence of Neimark–Sacker bifurcations when varying the damping factor and wave-particle coupling strength. In addition, we introduced a new global bifurcation that leads to the chaotic behavior of the system. Although the model is slightly removed from the physics of hydrodynamic quantum analogs, understanding the dynamics of this simple model may help us discover statistical properties, such as invariant measures, to guide experiments and numerics for the more complex models.

11.3 Future Work

In this section we propose future investigations and comment on the direction of current research in chaotic logical circuits and walking droplets.

11.3.1 Chaotic Logical Circuits

After a decade – long drought, in recent years there has been a resurgence in the studies of chaotic logical circuits. These circuits are mainly studied as analogs of logical systems appearing in nature and for the purposes of communication. The other logical systems of interest are mainly biological and often times neuronal. Since

neurons are traditionally modeled as electrical circuits [64, 45, 46, 47] and physical electrical circuit realizations have been developed to replicate the behavior in neuron models [113], it is natural to ask whether chaotic logical circuits can be used to replicate the behavior observed in more complex models of neuronal networks. Recent work by Leiser and Rotstein [86] has inspired us to develop such analogs. In addition, there are several groups from both a biological background and a physical one working on understanding the connections between these electrical systems and those found in nature.

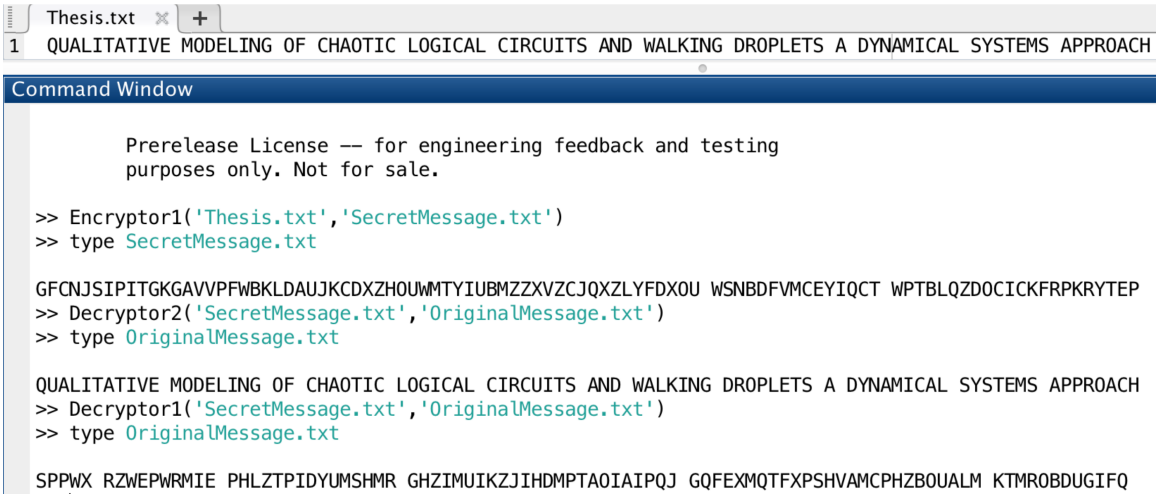

Figure 11.1 Example of chaotic encryption implemented on MATLAB.

There has also been renewed interest in chaotic communication [138]. The communications aspect is what initially attracted us to the topic, which has led us to develop a MATLAB code (See Appendix A) using our modeling framework from Section 4.2 to replicate chaotic encryption. An example of the encryption is shown in Figure 11.1. Here *Encryptor 1* and *Decryptor 1* uses the first threshold, and is employed by "Person 1". Similarly, *Encryptor 2* and *Decryptor 2* uses the second threshold, and is employed by "Person 2". At each chaotic cycle of the thresholds the Encryptor/Decryptor pairs integrates over their respective voltages, which provides

the new encryption code. Since users only have access to one threshold they will not be able to decrypt their own message as shown in the last line of Figure 11.1. The next goal would be to use our circuits and develop this encryption system, and our simple code serves as a proof of concept example that this may work.

11.3.2 Walking Droplets

Due to the nascency of the field and complexity of the phenomena of interest, there is an abundance of novel problems to pursue. By using dynamical systems theory this phenomena can be attacked on two fronts: developing new dynamical models amenable to analysis while also having strong connections with experiments and pushing the boundary of the theory for existing models. From the analysis perspective the most important problem currently is the derivation invariant measures for the dynamical models, which would create a direct link between the theory and experiments. If invariant measures can be found, even through numerical approximations, we may be able to identify physical properties that would lead to desired statistics. Due to the difficulty of the problem, this would be a more long term endeavor. The more immediately accessible problem would be the detailed characterization of the new bifurcation observed in Section 10.3 and *crises* bifurcations, is currently underway.

From the modeling side there are two polar categories: "accurate but mathematically complex" and "mathematically tractable but lacking in physical connection", which represents a rather wide gap. We are currently developing discrete dynamical and hybrid models to bridge this gap. The goal is to develop models that take advantage of the simplicity in [49] and incorporate more detailed physics from [119, 120, 121]. Furthermore, there are many aspects of the system that have not been explored in detail, such as boundary effects. Recently there has been some experimental work [134] on these effects and some models have incorporated simple

assumptions to treat boundaries, however new mechanistic models are necessary to achieve better agreement with experiments.

Finally, we can use chaotic circuits to study walking droplets and use walking droplets to develop a logic family. Recently a logic family using droplets (but no bouncing) was developed [76] and this shows promise that the same can be accomplished for walking droplets. Furthermore, our circuits can be used to chaotically vary the amplitude of the fluid bath potentially revealing new phenomena.

APPENDIX A

MATLAB CODES FOR TOY CHAOTIC ENCRYPTION DEMONSTRATION

Code used by "Person 1" to encrypt message.

```
function Encryptor1(file,CryptFile)

%Input:  file name
%Output:  Encrypted file

%%% Read file %%%
fileID = fopen(file, 'r');
M = textscan(fileID, '%c','whitespace',''); % M - message
M = cell2mat(M);
fclose(fileID);
%%%

%%% For now this only encrypts/decrypts capital letters
%%% and no punctuation...cus we gangsta like that.
Alphabet = 'ABCDEFGHIJKLMNOPQRSTUVWXYZ '; %initialize alphabet with space

%%% Convert message M into numerical values %%%
NumM = zeros(1,length(M));
for n = 1:length(M)
for i = 1:length(Alphabet)
    if M(n) == Alphabet(i)
    NumM(n) = i;
    end
end
end
%%%

%%%%%%%%%%%%%%%%%%%%%%%%%%%%%% Encryption 1 %%%%%%%%%%%%%%%%%%%%%%%%%%%%%%
%%%External Parameters%%%
T1 = 20;  %period of I1 and I4
T2 = 40;  %period of I2 and I3
Total = T2*length(M);  %Total time of clock
freq = 1/9;  %internal frequency
%%%%%%%%%%%%%%%%%%%%%%%%%%
N = Total/freq;

%%%Internal Parameters%%%
mu = 3.2;
nu = 2*mu/(1+mu^2);
%%%%%%%%%%%%%%%%%%%%%%%%%%

%%%Initialization%%%
f = zeros(1,N+1);  %VT1
%%%%%%%%%%%%%%%%%%%%

%%%Inputs%%%
I1 = f;
I2 = f;
for n = 1:2*length(M)
     I1((2*n-1)*T1/(2*freq)+1:n*T1/freq+1) = 1;
end
for n = 1:length(M)
    I2((2*n-1)*T2/(2*freq)+2:n*T2/freq+1) = 1 - n*1e-9;
end
%%%%%%%%%%%%

for n = 1:N

    %%%VT1 calculations%%%

    if  f(n) >= -nu*mu && f(n) < -nu

        yf = (1+mu)*f(n)/(1-mu) + nu*(1+mu)/(1-mu) - mu*nu;

```

```
        else if f(n) >= -nu && f(n) <= nu

            yf = mu*f(n);

            else

            yf = (1+mu)*f(n)/(1-mu) - nu*(1+mu)/(1-mu) + mu*nu;

        end

    end

    f(n+1) = abs(I1(n+1) - I2(n+1)) + I1(n+1)*I2(n+1)*yf;
    %%%%

    %%% Integrating the chaotic timeseries %%%
    if mod((n+1)*freq,T2) == 0
        SumF = sum(f((((n+1)*freq - 10)/freq):(n+1)));
        SumF = round(SumF);
        NumM((n+1)*freq/T2) = NumM((n+1)*freq/T2) + SumF;
        NumM((n+1)*freq/T2) = mod(NumM((n+1)*freq/T2),27);
        if NumM((n+1)*freq/T2) == 0
            NumM((n+1)*freq/T2) = 27;
        end
        M((n+1)*freq/T2) = Alphabet(NumM((n+1)*freq/T2));
    end
    %%%%

end
%%%%%%%%%%%%%%%%%%%%%%%%%%%%%%%%%%

%%% Writes encrypted file
fileID = fopen(CryptFile,'w');
fprintf(fileID,'%c',M);
fclose(fileID);
```

Code used by "Person 2" to decrypt message from "Person 1"

```
function Decryptor2(CryptFile,file)

%Input:  Encrypted file name
%Output:  Decrypted file

%%% Read file %%%
fileID = fopen(CryptFile, 'r');
M = textscan(fileID, '%c','whitespace','');  % M - message
M = cell2mat(M);
fclose(fileID);
%%%

%%% For now this only encrypts/decrypts capital letters
%%% and no punctuation...cus we gangsta like that.
Alphabet = 'ABCDEFGHIJKLMNOPQRSTUVWXYZ ';  %initialize alphabet with space

%%% Convert message M into numerical values %%%
NumM = zeros(1,length(M));
for n = 1:length(M)
for i = 1:length(Alphabet)
    if M(n) == Alphabet(i)
    NumM(n) = i;
    end
end
end
%%%

%%%%%%%%%%%%%%%%%%%%%%%%%%%%%%%%%% Decryption 2 %%%%%%%%%%%%%%%%%%%%%%%%%%%%%%%%%%
%%%External Parameters%%%
T1 = 20;  %period of I1 and I4
T2 = 40;  %period of I2 and I3
Total = T2*length(M);  %Total time of clock
freq = 1/9;  %internal frequency
%%%%%%%%%%%%%%%%%%%%%%%%%%%%%
N = Total/freq;

%%%Internal Parameters%%%
mu = 3.2;
nu = 2*mu/(1+mu^2);
%%%%%%%%%%%%%%%%%%%%%%%%%%%%

```

```
%%%Initialization%%%
f = zeros(1,N+1);  %VT1
%%%%%%%%%%%%%%%%%%%%%

%%%Inputs%%%
I1 = f;
I2 = f;
for n = 1:2*length(M)
     I1((2*n-1)*T1/(2*freq)+1:n*T1/freq+1) = 1;
end
for n = 1:length(M)
    I2((2*n-1)*T2/(2*freq)+2:n*T2/freq+1) = 1 - n*1e-9;
end
%%%%%%%%%%%%

for n = 1:N

    %%%VT1 calculations%%%

    if  f(n) >= -nu*mu && f(n) < -nu

        yf = (1+mu)*f(n)/(1-mu) + nu*(1+mu)/(1-mu) - mu*nu;

        else if f(n) >= -nu && f(n) <= nu

            yf = mu*f(n);

            else

            yf = (1+mu)*f(n)/(1-mu) - nu*(1+mu)/(1-mu) + mu*nu;

        end

    end

    f(n+1) = abs(I1(n+1) - I2(n+1)) + I1(n+1)*I2(n+1)*yf;
    %%%%

    %%% Integrating the chaotic timeseries %%%
    if mod((n+1)*freq,T2) == 0
        SumF = sum(f((((n+1)*freq - 10)/freq):(n+1)));
        SumF = round(SumF);
        NumM((n+1)*freq/T2) = NumM((n+1)*freq/T2) - SumF;
        NumM((n+1)*freq/T2) = mod(NumM((n+1)*freq/T2),27);
         if NumM((n+1)*freq/T2) == 0
            NumM((n+1)*freq/T2) = 27;
         end
        M((n+1)*freq/T2) = Alphabet(NumM((n+1)*freq/T2));
    end
    %%%%

end
%%%%%%%%%%%%%%%%%%%%%%%%%%%%%%%%%%%%%%%%

%%% Writes decrypted file
fileID = fopen(file,'w');
fprintf(fileID,'%c',M);
fclose(fileID);
```

Code used by “Person 2” to encrypt message.

```
function Encryptor2(file,CryptFile)

%Input:  file name
%Output:  Encrypted file

%%% Read file %%%
fileID = fopen(file, 'r');
M = textscan(fileID, '%c','whitespace','');% M - message
M = cell2mat(M);
fclose(fileID);
%%%

%%% For now this only encrypts/decrypts capital letters
%%% and no punctuation...cus we gangsta like that.
Alphabet = 'ABCDEFGHIJKLMNOPQRSTUVWXYZ '; %initialize alphabet with space

%%% Convert message M into numerical values %%%
NumM = zeros(1,length(M));
```

```
for n = 1:length(M)
for i = 1:length(Alphabet)
    if M(n) == Alphabet(i)
    NumM(n) = i;
    end
end
end
%%%

%%%%%%%%%%%%%%%%%%%%%%%%%%%%%% Encryption 2 %%%%%%%%%%%%%%%%%%%%%%%%%%%%%%
%%%External Parameters%%%
T1 = 20;  %period of I1 and I4
T2 = 40;  %period of I2 and I3
Total = T2*length(M);  %Total time of clock
freq = 1/9;  %internal frequency
%%%%%%%%%%%%%%%%%%%%%%%%%%%%
N = Total/freq;

%%%Initialization%%%
g = zeros(1,N+1);  %VT2
%%%%%%%%%%%%%%%%%%%%

%%%Inputs%%%
I1 = g;
I2 = g;
for n = 1:2*length(M)
     I1((2*n-1)*T1/(2*freq)+1:n*T1/freq+1) = 1;
end
for n = 1:length(M)
    I2((2*n-1)*T2/(2*freq)+2:n*T2/freq+1) = 1 - n*1e-9;
end
g(1) = -1;
%%%%%%%%%%%%

for n = 1:N

    %%%VT2 calculations%%%

    if abs(g(n)-1/3) <= 1/2

        yg = 1/3 + 2*abs(g(n)-1/3);

    else

        yg = 1/3 + 2*(1-abs(g(n)-1/3));

    end

    g(n+1) = abs(I2(n+1) - I1(n+1)) - 1 + I2(n+1)*I1(n+1)*yg;
    %%%%

    %%% Integrating the chaotic timeseries %%%
    if mod((n+1)*freq,T2) == 0
        SumG = sum(g((((n+1)*freq - 10)/freq):(n+1)));
        SumG = round(SumG);
        NumM((n+1)*freq/T2) = NumM((n+1)*freq/T2) + SumG;
        NumM((n+1)*freq/T2) = mod(NumM((n+1)*freq/T2),27);
         if NumM((n+1)*freq/T2) == 0
            NumM((n+1)*freq/T2) = 27;
         end
        M((n+1)*freq/T2) = Alphabet(NumM((n+1)*freq/T2));
    end
    %%%%

end
%%%%%%%%%%%%%%%%%%%%%%%%%%%%%%%%%%%%%%%%%%%%

%%% Writes encrypted file
fileID = fopen(CryptFile,'w');
fprintf(fileID,'%c',M);
fclose(fileID);
```

Code used by “Person 1” to decrypt message from “Person 2”

```
function Decryptor1(CryptFile,file)

%Input:  file name
%Output:  Encrypted file

```

```
%%% Read file %%%
fileID = fopen(CryptFile, 'r');
M = textscan(fileID, '%c','whitespace',''); % M - message
M = cell2mat(M);
fclose(fileID);
%%%

%%% For now this only encrypts/decrypts capital letters
%%% and no punctuation...cus we gangsta like that.
Alphabet = 'ABCDEFGHIJKLMNOPQRSTUVWXYZ '; %initialize alphabet with space

%%% Convert message M into numerical values %%%
NumM = zeros(1,length(M));
for n = 1:length(M)
for i = 1:length(Alphabet)
    if M(n) == Alphabet(i)
    NumM(n) = i;
    end
end
end
%%%

%%%%%%%%%%%%%%%%%%%%%%%%%%%%%% Decryption 1 %%%%%%%%%%%%%%%%%%%%%%%%%%%%%%
%%%External Parameters%%%
T1 = 20;  %period of I1 and I4
T2 = 40;  %period of I2 and I3
Total = T2*length(M);  %Total time of clock
freq = 1/9;  %internal frequency
%%%%%%%%%%%%%%%%%%%%%%%%%%%
N = Total/freq;

%%%Initialization%%%
g = zeros(1,N+1);  %VT2
%%%%%%%%%%%%%%%%%%%%%%%
%%%Inputs%%%
I1 = g;
I2 = g;
for n = 1:2*length(M)
     I1((2*n-1)*T1/(2*freq)+1:n*T1/freq+1) = 1;
end
for n = 1:length(M)
    I2((2*n-1)*T2/(2*freq)+2:n*T2/freq+1) = 1 - n*1e-9;
end
g(1) = -1;
%%%%%%%%%%%%

for n = 1:N

    %%%VT2 calculations%%%

    if abs(g(n)-1/3) <= 1/2

        yg = 1/3 + 2*abs(g(n)-1/3);

    else

        yg = 1/3 + 2*(1-abs(g(n)-1/3));

    end

    g(n+1) = abs(I2(n+1) - I1(n+1)) - 1 + I2(n+1)*I1(n+1)*yg;
    %%%%

    %%% Integrating the chaotic timeseries %%%
    if mod((n+1)*freq,T2) == 0
        SumG = sum(g((((n+1)*freq - 10)/freq):(n+1)));
        SumG = round(SumG);
        NumM((n+1)*freq/T2) = NumM((n+1)*freq/T2) - SumG;
        NumM((n+1)*freq/T2) = mod(NumM((n+1)*freq/T2),27);
         if NumM((n+1)*freq/T2) == 0
            NumM((n+1)*freq/T2) = 27;
         end
        M((n+1)*freq/T2) = Alphabet(NumM((n+1)*freq/T2));
    end
    %%%%

end
%%%%%%%%%%%%%%%%%%%%%%%%%%%%%%%%%%%%%%%%%%%%%%

%%% Writes decrypted file
fileID = fopen(file,'w');
fprintf(fileID,'%c',M);
fclose(fileID);
```

REFERENCES

[1] A. Andronov and L. Pontryagin. Systèmes grossiers. *Dokl. Akad. Nauk. SSSR*, 14:247–251, 1937.

[2] V. I. Arnold. Small denominators, I: mappings of the circumference into itself. *AMS Transl. Ser.*, 46(2):213–284, 1965.

[3] D. Arrowsmith and C. Place. *An Introduction to Dynamical Systems*. Cambridge University Press, Cambridge, United Kingdom, 1990.

[4] J. S. Bell. *Speakable and Unspeakable in Quantum Mechanics*. Cambridge University Press, Cambridge, United Kingdom, 1987.

[5] J. Bernoulli. Explicationes, annotationes et additiones ad ea, quae in actis sup. de curva elastica, iisochrona paracentrica, et velaria, hinc inde memorata, et paratim controversa legundur; ubi de linea mediarum directionum, alliisque novis. *Acta Eruditorum*, 1695.

[6] A. Bertozzi. Heteroclinic orbits and chaotic dynamics in planar fluid flows. *SIAM J. Appl. Math*, 19(6):1271–1294, 1988.

[7] D. Blackmore. New models for chaotic dynamics. *Regular & Chaotic Dynamics*, 10:307–321, 2005.

[8] D. Blackmore and Y. Joshi. Strange attractors for asymptotically zero maps. *Chaos, Solitons and Fractals*, 68:123–138, 2014.

[9] D. Blackmore, A. Rahman, and J. Shah. Discrete dynamical modeling and analysis of the r-s flip-flop circuit. *Chaos, Solitons & Fractals*, 42:951–963, 2009.

[10] D. Bohm and J. Vigier. Model of the causal interpretation of quantum theory in terms of a fluid with irregular fluctuations. *Phys. Rev.*, 96:208, 1954.

[11] P. Brun, D. Harris, V. Prost, J. Quintela, and J. Bush. Shedding light on pilot-wave phenomena. *Phys. Rev. Fluids*, 1:050510, 2016.

[12] J. Bush. Quantum mechanics writ large. *Proc. Nat. Acad. Sci.*, pages 1–2, 2010.

[13] J. Bush. The new wave of pilot-wave theory. *Physics Today*, 68(8):47–53, 2015.

[14] J. Bush. Pilot-wave hydrodynamics. *Ann. Rev. Fluid Mech.*, 49:269–292, 2015.

[15] J. Bush, A. Oza, and J. Molacek. The wave-induced added mass of walking droplets. *J. Fluid Mech.*, 755:R7, 2014.

[16] D. Cafagna and G. Grassi. Chaos-based SR flip-flop via Chua's circuit. *Int J Bifurcat Chaos*, 16(5):1521–1526, 2006.

[17] J. Champanerkar and D. Blackmore. Pitchfork bifurcation of invariant manifolds. *Topology and Its Applications*, 154:1650–1663, 2007.

[18] T. Chaney. A note on synchronizer and interlock maloperation. *IEEE Trans. Computers*, C-28:802–804, 1979.

[19] Chetvorno. https://en.wikipedia.org/wiki/File:Chua27s_circuit_with_Chua_diode.svg. April 13, 2017, February 2014.

[20] L. O. Chua. *Introduction to Nonlinear Network Theory*. McGraw-Hill, New York, NY, 1969.

[21] L. O. Chua. The genesis of Chua's circuit. *Archiv für Elektronik und Ubertragung-stechnik*, 46:250–257, 1992.

[22] L. O. Chua. Global unfolding of Chua's circuit. *IEICE Transactions on Fundamentals of Electronics, Communications, Computer Science*, E76-A:704–734, 1993.

[23] L. O. Chua. Chua's circuit: Ten years later. *IEICE Trans. Fundamentals*, E77-A:1811–1821, 1994.

[24] L. O. Chua, M. Komuro, and T. Matsumoto. The double scroll family. *IEEE Transactions on Circuits and Systems*, 33:1072–1118, 1986.

[25] L. O. Chua, C. Wu, A. Huang, and G. Zhong. A universal circuit for studying and generating chaos - part II: Strange attractors. *IEEE Trans. on Circuits and Systems*, 40:745–761, 1993.

[26] E. Coddington and N. Levinson. *Theory of Ordinary Differential Equations*. McGraw-Hill, New York, 1955.

[27] Y. Couder and E. Fort. Single-particle diffraction and interference at a macroscopic scale. *Phys. Rev. Lett.*, 97:154101, 2006.

[28] Y. Couder, S. Protiere, E. Fort, and A. Boudaoud. Dynamical phenomena: Walking and orbiting droplets. *Nature*, 437:208, 2005.

[29] M. Crommie, C. Lutz, and D. Eigler. Confinement of electrons to quantum corrals on a metal surface. *Science*, 262:218–220, 1993.

[30] J. M. Cruz and L. O. Chua. An ic chip of Chua's circuit. *IEEE Transactions on Circuits and Systems-II*, 10:596–613, 1993.

[31] K. Cuomo and A. Oppenheim. Circuit implementation of synchronized chaos with applications to communications. *Phys. Rev. Lett.*, 71(1):65–68, 1993.

[32] A. P. Damiano, P. Brun, D. Harris, C. Galeano-Rios, and J. Bush. Surface topography measurements of the bouncing droplet experiment. *Experiments in Fluids*, 57:163, 2016.

[33] M. D'Amico, J. Moiola, and E. Paolini. Hopf bifurcation in discrete-time systems via a frequency domain approach. In *Proc. IEEE COC Conf.*, pages 290–293, St. Petersburg, Russia, 2000.

[34] M. Danca. Numerical approximation of a class of switch dynamical systems. *Chaos, Solitons and Fractals*, 38:184–191, 2008.

[35] L. de Broglie. *Ondes et mouvements*. Gauthier-Villars, Paris, France, 1st edition, 1926.

[36] W. de Melo. Structural stability of diffeomorphisms on two-manifolds. *Invent. Math.*, 21(3):233–246, 1973.

[37] B. Deng. The Shilnikov problem, exponential expansion, strong λ-lemma, c^1-linearization and homoclinic bifurcations. *J. Diff. Eqs.*, 79(2):189–231, 1989.

[38] W. Ditto, K. Miliotis, K. Murali, S. Sinha, and M. Spano. Chaogates: Morphing logic gates that exploit dynamical patterns. *Chaos*, 20(037107), 2010.

[39] G. Duffing. *Erzwungene Schwingungen bei Veränderlicher Eigenfrequenz*. F. Vieweg u. Sohn, Braunschweig, Germany, 1918.

[40] A. Eddi, E. Fort, F. Moisy, and Y. Couder. Unpredictable tunneling of a classical wave-particle association. *Phys. Rev. Lett.*, 102:240401, 2009.

[41] A. Eddi, J. Moukhtar, S. Perrard, E. Fort, and Y. Couder. Level splitting at macroscopic scale. *Phys. Rev. Lett.*, 108:264503, 2012.

[42] A. Eddi, E. Sultan, J. Moukhtar, E. Fort, M. Rossi, and Y. Couder. Information stored in Faraday waves: the origin of path memory. *J. Fluid Mech.*, 674:433–463, 2011.

[43] B. Filoux, M. Hubert, P. Schlagheck, and N. Vandewalle. Waveguides for walking droplets. Arxiv: 1507.08228v1, July 2015.

[44] B. Filoux, M. Hubert, and N. Vandewalle. Strings of droplets propelled by coherent waves. *Phys. Rev. E*, 92:041004(R), 2015.

[45] R. FitzHugh. Mathematical models of threshold phenomena in the nerve membrane. *Bull. Math. Biophysics*, 17:257—278, 1955.

[46] R. FitzHugh. Impulses and physiological states in theoretical models of nerve membrane. *Biophysical J.*, 1:445–466, 1961.

[47] R. FitzHugh. *Mathematical models of excitation and propagation in nerve.* McGraw–Hill Book Co., 1969.

[48] E. Fort, A. Eddi, A. Boudaoud, J. Moukhtar, and Y. Couder. Path-memory induced quantization of classical orbits. *Proc. Nat. Acad. Sci.*, 107:17515, 2010.

[49] T. Gilet. Dynamics and statistics of wave-particle interaction in a confined geometry. *Phys. Rev. E*, 90:052917, 2014.

[50] C. Grebogi, E. Ott, and J. Yorke. Crises: sudden changes in chaotic attractors and chaotic transients. *Physica D*, 7:181, 1983.

[51] D. Grobman. Homeomorphisms of systems of differential equations. *Dokl. Akad. Nauk SSSR*, 128:880–881, 1959.

[52] J. Guckenheimer and P. Holmes. *Nonlinear Oscillations, Dynamical Systems, and Bifurcation of Vector Fields.* Springer-Verlag, New York, NY, 1983.

[53] V. Guillemin and A. Pollack. *Differential Topology.* Prentice-Hall, 1974.

[54] J. S. Hadamard. Les surfaces à courbures opposées et leurs lignes géodesiques. *Journal de Mathématiques Pures et Appliquées*, 4:27–73, 1898.

[55] D. Hamil. Learning about chaotic circuits with SPICE. *IEEE Trans. Education*, 36:28–35, 1993.

[56] D. Hamil, J. Deane, and D. Jeffries. Modeling of chaotic DC/DC converters by iterated nonlinear maps. *IEEE Trans Power electronics*, 7:25–36, 1992.

[57] D. Harris and J. Bush. The pilot-wave dyanmics of walking droplets. *Phys. Fluids*, 25:091112, 2013.

[58] D. Harris and J. Bush. Droplets walking in a rotating frame: from quantized orbits to multimodal statistics. *J. Fluid Mech.*, 739:444–464, 2014.

[59] D. Harris, J. Moukhtar, E. Fort, Y. Couder, and J. Bush. Wavelike statistics from pilot-wave dyanmics in a circular corral. *Phys. Rev. E*, 88:011001, 2013.

[60] D. Harris, J. Quintela, V. Prost, P. Brun, and J. Bush. Visualization of hydrodynamic pilot-wave phenomena. *J. Vis.*, 2016.

[61] P. Hartman. On the local linearization of differential equations. *Proc. Amer. Math. Soc.*, 14:568–573, 1963.

[62] P. Hartman. *Ordinary Differential Equations.* Birkhäuser, New York, 2 edition, 1982.

[63] M. Hénon. A two-dimensional mapping with a strange attractor. *Commun. Math. Phys.*, 50(1):69–77, 1976.

[64] A. Hodgkin and A. Huxley. A quantitative description of membrane current and its application to conduction and excitation in nerve. *The Journal of Physiology*, 117(4):500–544, 1952.

[65] P. Holmes. The dynamics of repeated impacts with a sinusoidally vibrating table. *J. Sound and Vibration*, 84(2):173–189, 1982.

[66] P. Holmes and D. Rand. Bifurcations of the forced van der Pol oscillator. *Quart. Appl. Math.*, 35:495–509, 1978.

[67] P. Holmes and D. Whitley. Bifurcations of one and two-dimensional maps. *Phil. Trans. R. Soc. A*, 311:43–102, 1984.

[68] E. Hopf. Abzweigung einer periodischen lösung von einer stationaren lösung eines differentialsystems. *Ber. Math.-Phys. Kl. Sachs, Acad. Wiss. Leipzig*, 94:1–22, 1942.

[69] C. Horsman, S. Stepney, R. Wagner, and V. Kendon. When does a physical system compute? *Proc. Roy. Soc. A*, 470:2169, 2014.

[70] A. Hurwitz. Ueber die bedingungen, unter welchen eine gleichung nur wurzeln mit negativen reellen theilen besitzt. *Math. Ann.*, 46(2):273–284, 1895.

[71] G. Ioos and D. Joseph. *Elementary Stability and Bifurcation Theory*. Springer-Verlag, New York, NY, 1981.

[72] Y. Joshi, D. Blackmore, and A. Rahman. Generalized attracting horseshoe and chaotic strange attractors. (under review), 2017.

[73] T. Kacprzak. Analysis of oscillatory metastable operation of RS flip-flop. *IEEE J. Solid-State Circuits*, 23:260–266, 1988.

[74] T. Kacprzak and A. Albicki. Analysis of metastable operation in RS CMOS flip-flop. *IEEE J. Solid-State Circuits*, SC-22:57–64, 1987.

[75] A. Katok and B. Hasselblatt. *Introduction to the Modern Theory of Dynamical Systems*. Cambridge University Press, Cambridge, United Kingdom, 1995.

[76] G. Katsikis, J. Cybulski, and M. Prakash. Sychronous universal droplet logic and control. *Nat. Phys.*, 11:588–596, 2015.

[77] M. Kennedy. Robust OP AMP realization of Chua's circuit. *Frequenz*, 46:66–80, 1992.

[78] G. Korir and M. Prakash. Punch card programmable microfluidics. *PLoS ONE*, 10(3):e0115993, 2015.

[79] A. Kosinski. *Differential Manifolds*. Dover, Mineola, NY, 2007.

[80] Kraaiennest. https://en.wikipedia.org/wiki/File:Van_der_pol_triode.svg. April 13, 2017, June 2009.

[81] Y. A. Kuznetsov. *Elements of Applied Bifurcation Theory*, volume 112. Springer-Verlag, New York, NY, 3 edition, 1995.

[82] M. Labousse, A. Oza, S. Perrard, and J. Bush. Pilot-wave dynamics in a harmonic potential: Quantization and stability of circular orbits. *Phys. Rev. E*, 93:033122, 2016.

[83] M. Labousse and S. Perrard. Non hamiltonian features of a classical pilot-wave dynamics. *Phys. Rev. E*, 2014.

[84] G. Lacroix, P. Marchegay, and N. Al Hossri. Prediction of flip-flop behavior in metastable state. *Electron. Lett.*, 16:725–726, 1980.

[85] G. W. v. Leibniz. Nova methodus pro maximis et minimis, itemque tangentibus, quae nec fractas nec irrationales quantitates moratur, et singulare pro illis calculi genus. *Acta eruditorum*, 1684.

[86] R. Leiser and H. Rotstein. Localized and mixed-mode oscillatory patterns in networks of relaxation oscillators with heterogeneous global coupling and diffusion. biorxiv, 2017.

[87] T. Li and J. Yorke. Period three implies chaos. *The American Mathematical Monthly*, 82(10):985–992, 1975.

[88] C. C. Lin and L. A. Segel. *Mathematics Applied to Deterministic Problems in the Natural Sciences*. SIAM, 1988.

[89] E. N. Lorenz. Deterministic nonperiodic flow. *J. Atoms. Sci.*, 20:130–141, 1963.

[90] E. N. Lorenz. Atmospheric predictability as revealed by naturally occuring analogues. *J. Atoms. Sci.*, 26(4):636–646, 1969.

[91] E. N. Lorenz. Three approaches to atmospheric predictability. *B. Am. Meteorol. Soc.*, 50:345–349, 1969.

[92] E. N. Lorenz. Irregularity: A fundamental property of the atmosphere. *Tellus A*, 36:98–110, 1984.

[93] A. Lyapunov. *General Problem of the Stability Of Motion*, volume 1. CRC Press, 1892.

[94] Maksim. https://en.wikipedia.org/wiki/File:Logistic_map_scatterplots_large.png. April 13, 2017, March 2006.

[95] A. Marcovitz. *Introduction to Logic Design*. McGraw-Hill, New York, 2 edition, 2005.

[96] F. Marotto. Snap-back repellers imply chaos. *J. Math. Anal. Appl.*, 63(1):199–223, 1978.

[97] F. Marotto. On redefining a snap-back repeller. *Chaos, Solitons and Fractals*, 25(1):25–28, 2005.

[98] J. Marsden and M. McCracken. *The Hopf Bifurcation and Its Applications*. Springer-Verlag, New York, NY, 1976.

[99] T. Matsumoto. A chaotic attractor from Chua's circuit. *IEEE Transactions on Circuits and Systems*, CAS-31(12):1055–1058, December 1984.

[100] R. M. May. Simple mathematical models with very complicated dynamics. *Nature*, 261(5560):459–467, 1976.

[101] R. McLachlan. A gallery of constant-negative-curvature surfaces. *Mathematical Intelligencer*, 16(4), 1994.

[102] J. Meiss. *Differential Dynamical Systems*. SIAM, Philadelphia, PA, 2007.

[103] P. Milewski, C. Galeano-Rios, A. Nachbin, and J. Bush. Faraday pilot-wave dynamics: modeling and computation. *J. Fluid Mech.*, 778:361–388, 2015.

[104] J. Milnor. *Topology from the Differentiable Viewpoint*. Princeton University Press, Princeton, NJ, 1997.

[105] J. Molacek and J. Bush. Droplets bouncing on a vibrating bath. *J. Fluid Mech.*, 727:582–611, 2013.

[106] J. Molacek and J. Bush. Droplets walking on a vibrating bath: towards a hydrodynamic pilot-wave theory. *J. Fluid Mech.*, 727:612–647, 2013.

[107] J. Moser. Bistable systems of differential equations with applications to tunnel diode circuits. *IBM J. Res. Dev.*, 5:226–240, 1961.

[108] J. Moser. *Stable and Random Motion in Dynamical Systems*. Princeton University Press, Princeton, NJ, 1973.

[109] K. Murali and S. Sinha. Experimental realization of chaos control by thresholding. *Phys. Rev. E*, 68, 2003.

[110] K. Murali, S. Sinha, and W. Ditto. Implementation of a nor gate by a chaotic Chua circuit. *Int J Bifurcat Chaos*, 13:2669–2672, 2003.

[111] K. Murali, S. Sinha, and W. Ditto. Realization of the fundamental nor gate using a chaotic circuit. *Phys. Rev. E*, 68:016205, 2003.

[112] A. Nachbin, P. Milewski, and J. Bush. Tunneling with a hydrodynamic pilot-wave model. *Phys. Rev. F*, 2:034801, 2017.

[113] J. Nagumo, S. Arimoto, and Y. S. An active pulse transmission line simulating nerve axon. *Proc. IRE*, 50:2061–2070, 1962.

[114] J. Neimark. On some cases of periodic motions depending on parameters. *Dokl. Akad. Nauk SSSR*, 129:736–739, 1959.

[115] I. Newton. *Philosophiæ Naturalis Principia Mathematica*. The Royal Society, 1687.

[116] I. Newton. Methodus fluxionum et serierum infinitarum cum eisudem applicatione ad curvarum geometriam. *Opuscola mathematica philosophica et philologica*, 1744.

[117] G. ocioso. https://en.wikipedia.org/wiki/File:Poincare_map.svg. April 25, 2017, February 2008.

[118] H. Okazaki, H. Nakano, and T. Kawase. Chaotic and bifurcation behavior in an autonomous flip-flop circuit using piecewise linear tunnel diodes. *Circ Syst*, 3:291–297, 1998.

[119] A. Oza, D. Harris, R. Rosales, and J. Bush. Pilot-wave dynamics in a rotating frame: on the emergence of orbital quantization. *J. Fluid Mech.*, 744:404–429, 2014.

[120] A. Oza, R. Rosales, and J. Bush. A trajectory equation for walking droplets: hydrodynamic pilot-wave theory. *J. Fluid Mech.*, 737:552–570, 2013.

[121] A. Oza, O. Wind-Willassen, D. Harris, R. Rosales, and J. Bush. Pilot-wave dynamics in a rotating frame: Exotic orbits. *Phys. Fluids*, 26:082101, 2014.

[122] J. Palis and W. de Melo. *Geometric Theory of Dynamical Systems*. Springer-Verlag, Berlin, 1982.

[123] L. Pecora and T. Carrol. Synchronization in chaotic systems. *Phys. Rev. Lett.*, 64(8):821–824, 1990.

[124] M. M. Peixoto. Structural stability on two-dimensional manifolds. *Topology*, 1:101–120, 1962.

[125] P. Percell. Structural stability on manifolds with boundaries. *Topology*, 12(2):123–144, 1973.

[126] L. Perko. *Differential Equations and Dynamical Systems*. Springer-Verlag, New York, NY, 3 edition, 2001.

[127] S. Perrard, M. Labousse, E. Fort, and Y. Couder. Chaos driven by interfering memory. *Phys. Rev. Lett.*, 113:104101, 2014.

[128] S. Perrard, M. Labousse, M. Miskin, E. Fort, and Y. Couder. Self-organization into quantized eigenstates of a classical wave-driven particle. *Nature Comm.*, 5:3219, 2014.

[129] J. H. Poincaré. Sur le problème des trois corps et les équations de la dynamique. divergence des séries de m. lindstedt. *Acta Mathematica*, 13:1–270, 1890.

[130] J. H. Poincaré. *Les méthodes nouvelles de la mécanique céleste*, volume 1. Gauthier-Villars, Paris, France, 1892-1899.

[131] J. H. Poincaré. *Leçons de Mécanique Céleste*, volume 1. Gauthier-Villars, 1905-1910.

[132] M. Prakash and N. Gershenfeld. Microfludic bubble logic. *Science*, 315:832–835, 2007.

[133] S. Protiere, A. Boudaoud, and Y. Couder. Particle-wave association on a fluid interface. *J. Fluid Mech.*, 554:85–108, 2006.

[134] G. Pucci, P. Saenz, L. Faria, and J. Bush. Non-specular reflection of walking droplets. *J. Fluid Mech.*, 804(R3):1–12, 2016.

[135] A. Rahman and D. Blackmore. Neimark–Sacker bifurcation and evidence of chaos in a discrete dynamical model of walkers. *Chaos, Solitons & Fractals*, 91:339–349, 2016.

[136] A. Rahman and D. Blackmore. Threshold voltage dynamics of chaotic RS flip-flop circuits. arXiv:1507.03065, 2017.

[137] A. Rahman, I. Jordan, and D. Blackmore. Qualitative models and experimental investigation of chaotic nor gates and set/reset flip-flops. arXiv:1702.04838, 2017.

[138] H.-P. Ren, C. Bai, J. Liu, M. Baptista, and C. Grebogi. Experimental validation of wireless communication with chaos. *Chaos*, 26:083117, 2016.

[139] C. Robinson. Structural stability of C^1 diffeomorphisms. *J. Diff. Eqs.*, 22:28–73, 1976.

[140] C. Robinson. *Dynamical Systems: Stability, Symbolic Dynamics, and Chaos*. Taylor & Francis Group: CRC Press, Boca Raton, FL, 1 edition, 1999.

[141] E. J. Routh. *A Treatise on the Stability of a Given State of Motion: Particularly Steady Motion.* Macmillan, 1877.

[142] M. Ruzbehani, L. Zhou, and M. Wang. Bifurcation features in a DC/DC converter under current-mode control. *Chaos, Solitons and Fractals*, 28:205–212, 2006.

[143] H. S. Cavalcante, G. D.J., J. Socolar, and R. Zhang. On the origin of chaos in autonomous boolean networks. *Phil. Trans. R. Soc. A*, 368:495–513, 2010.

[144] R. Sacker. On invariant surfaces and bifurcation of periodic solutions of ordinary differential equations. *Report IMM-NYU*, 333:1–62, 1964.

[145] A. Seed and R. Byrne. Animal tool-use. *Curr. Biol.*, 20:R1032–R1039, 2010.

[146] D. Shirokoff. Bouncing droplets on a billiard table. *Chaos*, 23:013115, 2013.

[147] S. Smale. On gradient dynamical systems. *Ann. of Math*, 74:199–206, 1961.

[148] S. Smale. Diffeomorphisms with many periodic points. In S. Carins, editor, *Differential and Combinatorial Topology*, pages 63–80, Princeton, NJ, 1963. Princeton University Press.

[149] S. Smale. Structurally stable systems are not dense. *Amer. J. Math.*, 88:491–496, 1966.

[150] S. Smale. Differentiable dynamical systems. *Bull. Amer. Math. Soc.*, 73:747–817, 1967.

[151] S. Smale. *The Mathematics of Time*. Springer-Verlag, New York, NY, 1980.

[152] S. Smale. Finding a horseshoe on the beaches of Rio. *Mathematical Intelligencer*, 20:39–44, 1998.

[153] S. Strogatz. *Nonlinear Dynamics and Chaos*. Westview Press, Cambridge, MA, 1994.

[154] SyntaxError55. https://en.wikipedia.org/wiki/File:Smale_Horseshoe_Map.svg. April 13, 2017, December 2007.

[155] L. Tambasco, D. Harris, A. Oza, R. Rosales, and J. Bush. The onset of chaos in orbital pilot-wave dynamics. *Chaos*, 26:103107, 2016.

[156] A. H. Taylor, G. R. Hunt, J. C. Holzhaider, and R. D. Gray. Spontaneous metatool use by New Caledonian crows. *Curr. Biol.*, 17(17):1504–1507, 2007.

[157] D. Vallado. *Fundamentals of astrodynamics and applications*. Springer-Verlag, New York, NY, 2007.

[158] B. Van der Pol. On "relaxation-oscillations". *Lond. Edinb. Dubl. Phil. Mag.*, 7(2):978–992, 1926.

[159] B. Van der Pol. Forced oscillations in a circuit with non-linear resistance (reception with reactive triode). *Lond. Edinb. Dubl. Phil. Mag.*, 7(3):65–80, 1927.

[160] G. Wan, D. Xu, and X. Han. On creation of Hopf bifurcations in discrete-time nonlinear systems. *CHAOS*, 12:350–355, 2002.

[161] Y. Wan. Computations of the stability condition for the Hopf bifurcation of diffeomorphisms on R^2. *SIAM J. Appl. Math*, 34:167–175, 1978.

[162] Widdma. https://en.wikipedia.org/wiki/File:VanderPol-lc.svg. April 13, 2017, September 2009.

[163] S. Wiggins. *Global Bifurcations and Chaos*. Springer-Verlag, New York, 1988.

[164] S. Wiggins. *Introduction to Applied Nonlinear Dynamical Systems and Chaos*. Springer-Verlag, New York, NY, 2 edition, 2003.

[165] E. Wigner. The unreasonable effectiveness of mathematics in the natural sciences. *Communications in Pure and Applied Mathematics*, 13, 1960.

[166] Wikimol. https://en.wikipedia.org/wiki/File:Lorenz_system_r28_s10_b2-6666.png. April 13, 2017, May 2005.

[167] O. Wind-Willassen, J. Molacek, D. Harris, and J. Bush. Exotic states of bouncing and walking droplets. *Phys. Fluids*, 25(082002):1–11, 2013.

[168] XaosBits. https://nl.wikipedia.org/wiki/File:HenonMapImage.png. April 13, 2017, February 2005.

[169] P. Zeeman. Doubles and triplets in the spectrum produced by external magnetic forces. *Phil. Mag.*, 44(266):55, 1897.

[170] P. Zeeman. On the influence of magnetism on the nature of the light emitted by a substance. *Phil. Mag.*, 43(226):332, 1897.

[171] A. Zorin, E. Tolkacheva, M. Khabipov, F. Buchholz, and J. Niemeyer. Dynamics of Josephson junctions and single-flux-quantum networks with superconductor-normal-metal junction shuntsjosephson junctions and single-flux-quantum networks with superconductor-normal-metal junction shunts. *Phys. Rev. B*, 74(014508), 2006.